



Final Report

Power Generation From Low Temperature Sources Utilizing A Stirling Engine

Date: 1st March 2018

Name: David S. Nobes, Alexander J. Hunt
Title: Professor
Company: University of Alberta
Department: Mechanical Engineering
Address: 10-281 Donadeo Innovation Centre for Engineering
9211-116 Street NW,
University of Alberta
Phone: 780 492 7031 **Fax:** 780 492 2200
Email: david.nobes@ualberta.ca

with financial support from

Alberta Innovates and Terrapin Geothermics Inc.

Disclaimer

Alberta Innovates (“AI”) and her Majesty the queen in right of Alberta make no warranty, express or implied, nor assume any legal liability or responsibility for the accuracy, completeness, or usefulness of any information contained in this publication, nor that use thereof infringe on privately owned rights. The views and opinions of the author expressed herein do not necessarily reflect those of AI or her majesty the Queen in right of Alberta. The directors, officers, employees, agents and consultants of AI and the Government of Alberta are exempted, excluded and absolved from all liability for damage or injury, howsoever caused, to any person in connection with or arising out of the use by that person for any purpose of this publication or its contents.

The University of Alberta makes no warranty, express or implied, nor assumes any legal liability or responsibility for the accuracy, completeness, or usefulness of any information contained in this publication, nor that use thereof infringes on privately owned rights. The views and opinions of the author expressed herein do not necessarily reflect those of the University of Alberta. The directors, officers, employees, agents, students and consultants of the University of Alberta are exempted, excluded and absolved from all liability for damage or injury, howsoever caused, to any person in connection with or arising out of the use by that person for any purpose of this publication or its contents.

Executive Summary (Non-Confidential)

A collaboration between the Dynamic Thermal Energy Conversion Laboratory (DTECL) in the Department of Mechanical Engineering and the University of Alberta, Terrapin Geothermics and Alberta Innovates(AI)) has been established to develop low temperature Stirling engines to extract usable amounts of electricity from low grade heat sources. These low-grade heat sources include geothermal brines and industrial waste heat streams that will have temperatures of $T_{max} < 100$ °C. The work undertaken is directed towards proposing the most promising low temperature Stirling engine configuration that will best succeed with the low-grade heat operation conditions.

To accomplish this goal, four different configurations were designed and investigated. A 90° Gamma, an inline Gamma (at two scales), an opposed piston Alpha and a Franchot double acting Alpha were designed and brought to different stages of development at the time of the writing of this report, ranging from extensive experimental testing to assembly. In addition to the design and build process, predictive models were developed, instrumentation systems were tested and several specialized experimental setups were designed and used to characterize seals, piston designs and heat exchangers.

A number of challenges delayed the collection of sufficient experimental data to provide a quantified UNIT recommendation. In addressing these challenges, a deeper understanding of rapid prototyping manufacturing process, the impact of forced work on engine performance and manufacturing low-cost piston seals have all been achieved. Many of the initial designs were redesigned to consider these findings and although the goal of the project was not achieved, the project has advanced significantly toward the final goal of extracting useful electrical energy from low temperature sources.

Detailed experimental results for the 90° Gamma have been collected and compared with the predictive models that have been developed. This engine, the most advanced configuration in current use, was originally designed as a high temperature ($T_{max} \sim 650$ °C) but was reconfigured to operate at a significantly lower temperature ($T_{max} > 180$ °C). Investigation of the different loss mechanisms for this configuration has highlighted that mechanical losses and ineffective heat transfer are the main important phenomenon when designing Stirling engine for low temperature operation. A conclusion from this work also, is that these two loss mechanisms will also be paramount in the design of any other configuration of Stirling engine. As these two loss mechanisms can be substantial compared to the amount of power generated from a low temperature source, they will remain dominant regardless of the configuration of Stirling engine.

Future work in this area will need to pay particular attention to all loss mechanisms and how they interact with each other. This will require the development of a third order, fully couple model of a low temperature Stirling engine. To offset mechanical losses, which would remain relatively constant for a particular mechanism, much larger scale engines should be constructed. Understanding of the fluid mechanics and heat transfer in fully reciprocating systems and how these can be scaled to physically large engines is also limited as requires further, significant investigation. Future work should focus on these to ensure that significant power for a particular engine configuration can be achieved.

Personnel

The following is a list of personnel who have undertaken activities in the project. Some of these being directly funded from the project while others have been associated with the project and provided insight.

Person	Position
Shahzeb Mirza	CO-OP Student (8 months)
Jakub Piwowarczyk	CO-OP Student (8 months)
Jason Michaud	MSc Student
Steven Middleton	Summer Student (now MSc)
David Miller	MSc Student
Michael Nicol-Seto	Summer Student (now MSc)
Connor Speer	MSc Student
Calynn Stumpf	MSc Student
Dr. Mouhammad El Hassan	Research Associate
Alexander Hunt	Research Engineer
Dr. Cagri Ayranci	Assistant Professor
Dr. C.R. (Bob) Koch	Professor
Dr. Alexandra Komrakova	Assistant Professor
Dr. David S. Nobes	Professor

Table of Contents

Disclaimer	i
Executive Summary (Non-Confidential)	ii
Personnel.....	iii
1 Introduction	1
1.1 Need and Opportunity	1
1.2 Low grade heat opportunities.....	1
1.2.1 Geothermal energy.....	1
1.2.2 Waste heat energy.....	2
1.3 The Stirling engine.....	3
1.4 Aim and Scope	5
2 Methods and Materials	7
2.1 Mathematical Modelling of the Stirling Engine Cycle	7
2.1.1 Basic physical modeling	7
2.1.2 First order model – ideal isothermal analysis	9
2.1.3 First order model - Adiabatic model.....	10
2.1.4 Second order models.....	11
2.2 Configurations.....	13
2.2.1 The 90° Gamma	13
2.2.2 The In-Line Gamma.....	15
2.2.3 The increased scale In-Line Gamma.....	16
2.2.4 The Opposed Piston Alpha	17
2.2.5 The Franchot Double Acting Alpha.....	19
2.3 Engine Test Bed	21
2.3.1 Data acquisition system	21
2.3.2 Engine control.....	22
2.4 Design considerations	23
2.4.1 Use of rapid prototyping.....	23
2.4.2 The effect of 3D printing on the design	25
2.4.3 Use of rolling diaphragms.....	26

2.4.4	Materials for strength and heat transfer	26
3	Results and Discussion	28
3.1	Limitations in the project	28
3.1.1	Generating reliable parts from additive manufacturing	28
3.1.2	Using 3-D printed components under pressure.....	30
3.1.3	The effect of forced work	32
3.1.4	Heat transfer in reciprocating systems.....	34
3.1.5	Sealing.....	37
3.1.6	Conclusions from the project limitations.....	38
3.2	Heat exchanger design	39
3.2.1	Characterizing heat exchangers in oscillating and pulsatile flow.....	39
3.3	Determining engine performance.....	42
3.3.1	The indicator diagram.....	42
3.3.2	Decoupled Stirling engine losses	43
3.3.3	Effect of geometry on engine performance	45
3.4	Literature review of the thermo-fluids of a Stirling engine	47
3.4.1	Reciprocating flows and heat transfer correlations in Stirling engines	48
3.4.2	Similarly parameters of a reciprocating flow.....	48
3.4.3	Experimental studies in reciprocating flows.....	48
3.4.4	Enhance mixing inside Stirling engine chambers.....	50
3.4.5	Enhance heat transfer using vortex generators	50
3.4.6	Numerical investigations of Stirling engine reciprocating flow	52
3.4.7	Conclusion	53
3.5	Determining the effect of engine scale on engine performance.....	53
3.5.1	Configuration comparison	53
3.5.2	The use of swept volume to derive an evaluation length scale.....	54
3.5.3	The use of overall engine size to derive an evaluation length scale	55
3.5.4	The use of displacer diameter to derive an evaluation length scale.....	57
3.5.5	Configuration comparison conclusions.....	58
3.6	Evaluation.....	59
4	Next Steps.....	61

4.1	Development of complete predictive models.....	61
4.2	Increasing UNIT scale.....	62
4.3	Configurations of CELLS	63
4.3.1	The 90° Gamma cell	63
4.3.2	The ILG cell	64
4.3.3	The opposed piston Alpha cell.....	65
4.4	Continued project funding.....	66
4.5	Research Presentations and Public Events	66
4.6	Research publications.....	67
5	Conclusion	68
6	References	69
	Appendix A – Published work.....	73

Table of Figures

Figure 1: A map showing the ground temperatures on top of the Precambrian basement in Western Canada showing a significant portion of the hottest ground temperatures within Alberta.[2]	2
Figure 2: The pressure versus volume (P-V) diagram of a (a) ideal Stirling engine and (b) real Stirling engine.....	3
Figure 3: Schematics of each of the three general classes of Stirling engine designs: (a) the oppositely opposed piston Alpha, (b) the in-line Gamma, (c) the 90° Gamma.....	4
Figure 4: Schematic showing the multi-unit design philosophy to go from a single unit to a complete system.....	5
Figure 5: The isothermal Stirling engine model showing (a) the temperature profile through the compression and expansion spaces in the engine, and (b) the resulting indicator diagram where the area inside the diagram represents the indicated power of the cycle	9
Figure 6: The adiabatic Stirling engine model showing the temperature profile through the compression and expansions spaces in the engine.....	10
Figure 7: Surface plot showing the effect of engine speed and mean engine pressure on the gas spring hysteresis losses of the 90° Gamma engine. The plane represents interpolated and extrapolated data from the experimental measurements shown with blue markers	12
Figure 8: The current 90° Gamma engine shown as (a) an annotated solid model render and (b) and digital image of the experimental setup	14
Figure 9: The current in-line Gamma shown as, (a) a solid model of the system and (b) a digital image of the constructed engine	15
Figure 10: The current Terrapin ILG shown as, (a) a solid model of the system and (b) a digital image of the constructed engine	16
Figure 11: The current opposed piston Alpha shown as, (a) a solid model and (b) a digital image of the constructed engine	18
Figure 12: The Franchot double acting Alpha shown as an annotated solid model, indicating the main components of the engine	19
Figure 13: Solid model render of the flat diaphragm testing setup designed to test the function of the piston/diaphragm system which will be used in the Franchot double acting alpha.....	20
Figure 14: Annotated image of the multi-purpose data acquisition system used to monitor Stirling engine performance.....	21
Figure 15: Screenshot of the user interface for the data acquisition software that includes real-time monitoring and long-term data acquisition at defined test conditions.....	22
Figure 16: Images of the additive manufacturing technology used, (a) FDM Printer (Ultimaker 3) and (b) SLS (Form 2).....	23

Figure 17: Images of typical parts manufactured with the different 3D printing technologies, the translucent parts in (a) and (b) were printed using SLA technology and shows the ability to imbed fasteners and bushings (a) and the ability to print threads (b). The blue part shown in (c) was printed with the FDM printer and allows complex structural components to be manufactured... 24

Figure 18: Schematic of a component of the OPA which was designed according to the maximum dimensions of the 3D printing build volume. 25

Figure 19: An example image of a rolling diaphragm. These types of devices are used to create a frictionless seal between the piston cylinder and piston. Different sizes are used for each of the different configurations..... 26

Figure 20: Thermal conductivity versus material melting point for common metal and polymeric materials which shows the low temperature insulators (Nylon, ABS, bismuth), the high temperature insulators (Inconel, steel) and the highly conductive metals (zinc, aluminium, copper) 27

Figure 21: Comparison between the as-printed water jacket (a) and the damaged water jacket from heated residual acetone from the acetone smoothing process 30

Figure 22: O-ring groove of a 3D printed part which has been filled with silicone to repair imperfections from the printing process 31

Figure 23: An image of the forced work concept which shows the block motion is in the opposite direction of the net force applied to the block 32

Figure 24: A simulated indicator diagram shown in blue, with a linear buffer pressure shown in black and the forced work is shown in red 33

Figure 25: Simulated indicator diagrams with two different buffer pressure conditions leading to (a) positive work due to a greater amount of indicated work compared to the forced work, and (b) negative work due to the a lesser amount of indicated work compared to the amount of forced work 34

Figure 26: CAD solid model section view of a flat plate heat exchanger on the ILG engine showing the tube inlet, outlet and water channels 35

Figure 27: CAD solid model of an annular finned tube heat exchangers in the increased scale ILG 36

Figure 28: Experimentally measured hot and cold wide gas temperatures as a function of time from increased scale ILG engine. The displacer was moved between top and bottom dead center and allowed to dwell for five seconds at each position due to the transient response of the thermocouples 36

Figure 29: CAD model of the ILG with the glass cylinder and graphite piston assembly 37

Figure 30: CAD model of the 90° Gamma engine with the glass cylinder and graphite piston assembly..... 38

Figure 31: Experimental heat exchanger characterization plots obtained from pulsatile flow conditions [24]	39
Figure 32: Process and instrumentation diagram (a) and solid model render (b) of an experimental setup for characterizing radiator style heat exchanger performance in oscillating flow	41
Figure 33: Spatial temperature distribution within the experimental duct	41
Figure 34: An experimental PV diagram and buffer pressure of the 90° Gamma engine with forced work shown in red.....	42
Figure 35: Experimental indicator diagrams with overlaid reference cycle models for the 90° Gamma (a) with a heater temperature of 400 °C, and (b) with a heater temperature of 300 °C with the modified piston	43
Figure 36: Normalized power losses (a) as a function of heater wall temperature for the 90° Gamma engine, (b) as a function of mean pressure	44
Figure 37: Temperature drops between the (a) heater and (b) cooler set point and the measured gas temperature as a function of mean pressure.....	45
Figure 38: Measured gas temperatures at the interface between the regenerator and the cooler with the engine running at a heating cap temperature of 200 °C.....	46
Figure 39: Polar plot of measured heater pressure drop magnitude [kPa] as a function of azimuthal heater cap position	47
Figure 40: A predictive plot of Shaft work obtained using the Beale correlation versus the cube root of the swept volume length scale.....	55
Figure 41: CAD model of the inline Gamma engine annotated to show the control volume which can be used to determine the evaluation length scale related to the physical scale of the UNIT .	56
Figure 42: A comparative plot of shaft work obtained using the Beale correlation for a range of control volume length scale values for each of the UNIT configurations	56
Figure 43: A comparative plot of shaft work obtained using the West correlation for a range of control volume length scale values for each of the UNIT configurations	57
Figure 44: A comparative plot of shaft work obtained using the Beale correlation for a range of displacer piston diameters for each of the UNIT configurations.....	58
Figure 45: CAD model comparing the current scale 90° Gamma to a scaled up representation of a scaled up 90° Gamma UNIT.....	62
Figure 46: Conceptual CELL connecting two 90° Gamma Units	63
Figure 47: A conceptual ILG CELL containing four coupled in-line Gamma UNITS	64
Figure 48: Schematic of a multi CELL system of inline Gamma engines inside of a 40-foot shipping container.....	64
Figure 49: Conceptual CELL containing two coupled OPA units	65

Figure 50: Schematic of a multi-CELL system of OPA engines inside of a 40-foot shipping container..... 65

Table of Tables

Table 1: Basic heat transfer equations and important non-dimensional numbers for ideal models of Stirling engines	8
Table 2: Comparative table of limitations for FDM and SLA printing	24
Table 3: Common 3D printed part issues and solutions for troubleshooting	29
Table 4 The assessment matrix for evaluating different Stirling engine configurations	60
Table 5: List research presentations and lab visits.....	66

Definitions

List of Abbreviations and Symbols

θ	Cycle angle
DTECL	Dynamic Thermal Energy Conversion Laboratory
E	Mechanical effectiveness
FDM	Fused deposition modelling
FSE	Franchot Stirling engine
HTG	High temperature Gamma
ILG	In-Line Gamma
K	Thermal conductivity
LTG	Low temperature Gamma
OPA	Opposed piston Alpha
PIV	Particle image velocimetry
PLIF	Planar laser-induced fluorescence
RANS	Reynolds Averaged Navier Stokes
SLA	Stereolithography
V_c	Compression space volume
V_e	Expansion space volume
VG	Vortex generator

1 Introduction

1.1 Need and Opportunity

There is significant energy available from geothermal reservoirs and waste heat streams in Alberta. Currently, there are few technologies that can convert significant amounts of low-grade heat into electricity. This project is undertaken by the Dynamic Thermal Energy Conversion Laboratory (DTECL) at the University of Alberta in collaboration with Terrapin Geothermics. The implementation of using Stirling engines as tools to convert low-grade heat into usable electrical energy is being explored

Both the government incentives to address climate change and the significant quantity of geothermal and waste heat streams in Alberta create a great opportunity for potential technology in this area. This opportunity goes beyond the renewable energy application. The use of heat engines to harness the low temperature (<100 °C) sources opens opportunities to use a much wider range of engine construction materials. These include aluminum, with its high thermal conductivity and plastics, with their excellent thermal insulation properties. These types of materials are not commonly used in Stirling engine manufacturing due to the high temperatures typically used to run the engines. Apart from their material property advantages, plastics are well suited for mass manufacturing methods including 3D printing and injection molding, thus allowing these units to be produced in volume and at low cost. Advances in mechanical engineering design tools also allow sophisticated geometries to be simulated. Coupled together with advanced manufacturing techniques, these sophisticated designs can become a reality.

1.2 Low grade heat opportunities

1.2.1 *Geothermal energy*

Geothermal energy is created when the heat of the earth is used as direct use heat, or to produce fuel and power. Large-scale geothermal plants are typically restricted to regions where hot geothermal resources are either easily accessible or which lie close to the surface and high temperature sources are available. A report written by the Earth and Atmospheric Sciences department at the University of Alberta titled *A Deep-Dive Analysis of the best Geothermal Reservoirs for Commercial Development in Alberta* [1] studied the geothermal potential in this province. As shown in Figure 1, the presence of 50 geothermal pools with temperatures greater than 100 °C, and another 300 with temperatures greater than 50 °C gives Alberta great potential for producing geothermal energy [1]. Typically, the drilling process to access these resources is costly. However, the presence of over 65,000 wells which are deeper than 1500 meters in Alberta are great opportunities to harness the latent heat of the earth [1].

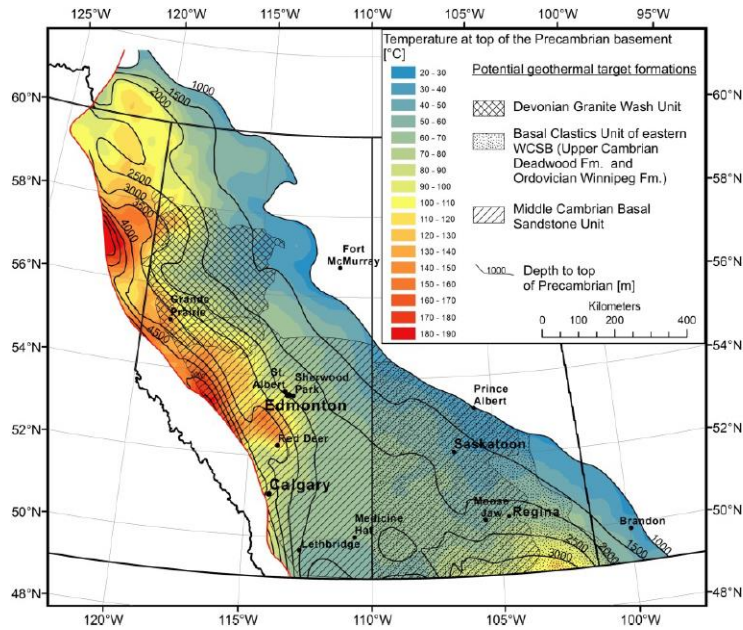


Figure 1: A map showing the ground temperatures on top of the Precambrian basement in Western Canada showing a significant portion of the hottest ground temperatures within Alberta.[2]

1.2.2 Waste heat energy

Waste heat streams in Alberta’s industrial sector also contain a significant amount of energy that has previously gone unused. These heat streams, which primarily consist of flue gasses, equate to an estimated 300 MW in the Edmonton area alone [3]. An estimated 20%-50% of all input energy is lost as waste heat [4] and being able to capture even a portion of this will significantly improve the efficiency of Canada’s industries. Work has been done to develop the framework required to harness this waste heat. This includes the development of metrics to evaluate the opportunities [5] and various approaches taken to reclaim this energy [6]–[8].

1.3 The Stirling engine

By using the thermodynamic cycle outlined in Figure 2, Stirling engines are capable of extracting work from a wide variety of temperature differentials. This is done by heating, cooling and extracting work from the working gas in the closed cycle [9], [10]. The Stirling engine design is driven by the addition and removal of heat from the working fluid. The majority of the literature discusses engines with hot side temperatures greater than 500 °C [11]–[13] with commercial combined heat and power systems using natural gas combustion to provide heat [14]. These high temperatures place limits on the types of materials that can be used for both the heat exchangers and the structural elements of the engine.

The thermodynamic cycle shown in Figure 2 (a) highlights the ideal Stirling cycle, which consists of four stages:

1. Isothermal expansion
2. Constant volume cooling
3. Isothermal compression
4. Constant volume heat addition

A slider crank mechanism is commonly used in Stirling engine design [15], [16] where the power piston and displacer are rigidly coupled to one-another. A combination of the coupled pistons and the slider crank piston motion creates a rounded and elliptical pressure versus volume diagram, also referred to as the indicator diagram. An example of this is shown in Figure 2 (b). Three different versions of the indicator diagram are represented here from two different ideal reference cycles (Schmidt and Adiabatic) and experimental measurements from a real Stirling engine.

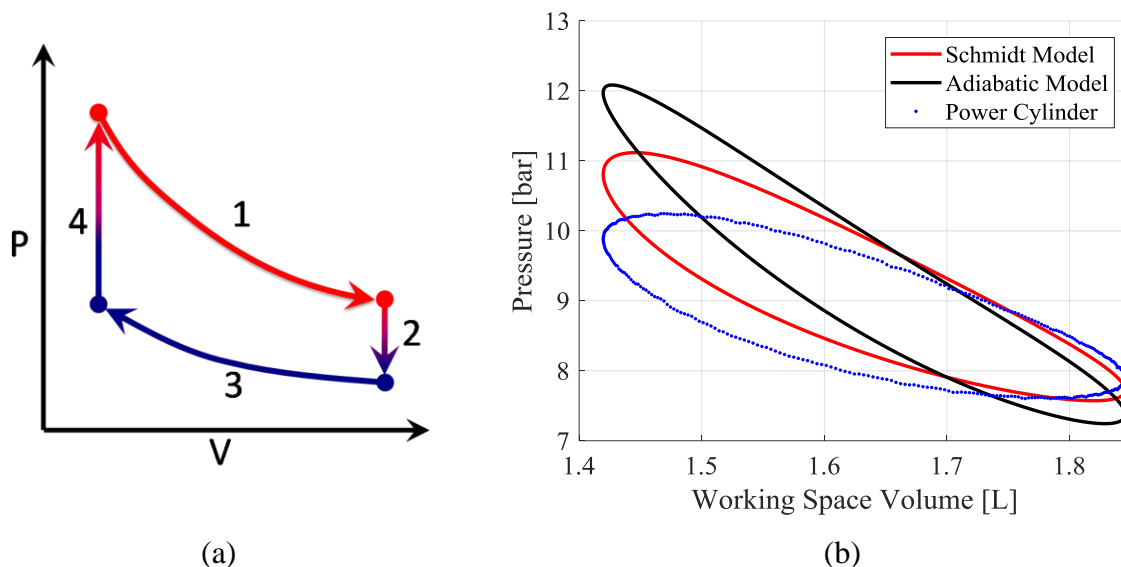


Figure 2: The pressure versus volume (P-V) diagram of a (a) ideal Stirling engine and (b) real Stirling engine.

The unique challenge of using low-grade heat sources, which can only provide a small amount of energy compared to traditional energy sources, opened up various previously unexplored design opportunities. These include unique Stirling engine materials (polymers), unique manufacturing methods (rapid prototyping) and new design approaches (scaling and coupling multiple units to increase usable power, the use of rolling diaphragms). In addition, the effect of Stirling engine geometry was explored through the development of four different Stirling engine configurations. The configuration of Stirling engine is defined by the arrangement of the displacer and power piston and their size ratios. Examples of different potential configurations are shown in Figure 3 and are Figure 3 (a), an opposed piston engine based on an Alpha Stirling engine configuration, Figure 3 (b), an in-line Gamma Stirling engine configuration and Figure 3 (b) a 90° Gamma Stirling engine configuration. The aim of the project has been to explore the potential of each of these configurations by building an engine of these types. A fourth engine has also been constructed, termed a Franchot double acting Alpha configuration (not shown).

Along with the engine geometry, the heat exchangers used to extract and transfer the heat to the working fluid have a significant impact on the final product. Separate experimental setups have been designed to characterize their performance under representative flow conditions. Throughout the design and build phases of each of the engines, factors including predicted output power and ease of manufacturing have been recorded, which will be essential for comparing the configurations against one another.

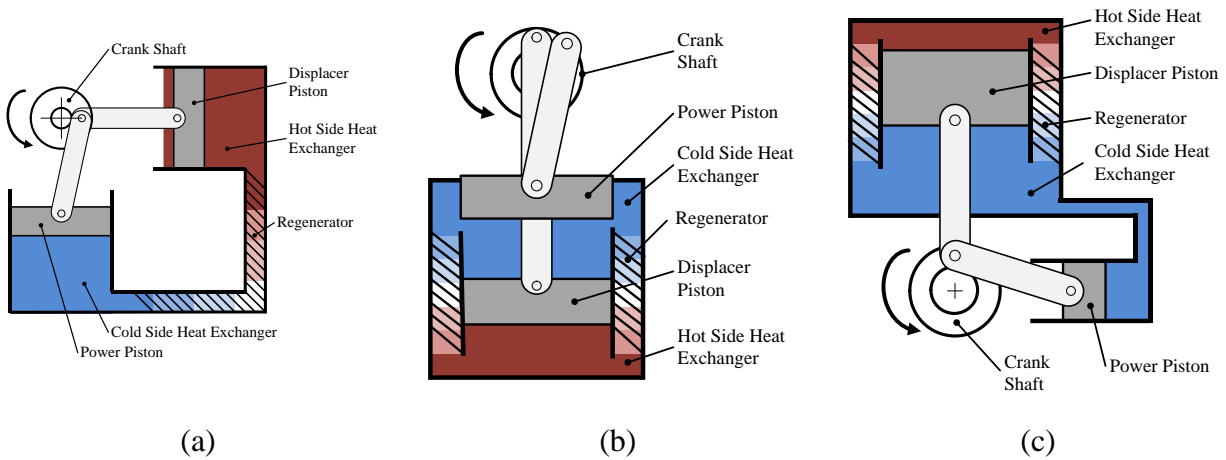


Figure 3: Schematics of each of the three general classes of Stirling engine designs: (a) the oppositely opposed piston Alpha, (b) the in-line Gamma, (c) the 90° Gamma.

The work done in this project has laid the groundwork for future developments in terms of not only engine design and manufacturing, but also engine control, coupling and scaling of designs in order to increase the power output. First order models have been developed for each engine configuration and the experimental data collected has allowed the development of second order models. These models are essential for predicting performance and operating conditions. They are also required for the implementation of an automated control scheme. Design and manufacture of the individual units was done in a way that allows instrumentation to be coupled to the units to gauge performance.

The 12 month project developed and implemented technologies to capture and extract low grade energy using the thermodynamic Stirling cycle. The goal of this project was to develop a single Stirling engine with suitable characteristics in terms of engine power output, reliability and manufacturability to serve as a base unit for the complete system design. To increase output power of the energy conversion system, the proposed units will be coupled together in a later stage of this project. The coupling scheme is shown in Figure 4 and shows the role of a single unit in the long-term goal of the project. The main focus of the work has been developing an understanding of the UNIT, with the role of the UNIT with respect to the overall project shown in Figure 4. This is a single Stirling engine configuration that can be mechanically coupled to other Stirling engines to construct a single CELL. Several of these cells could be then mechanically coupled to build an engine made up of many individual Stirling engines.

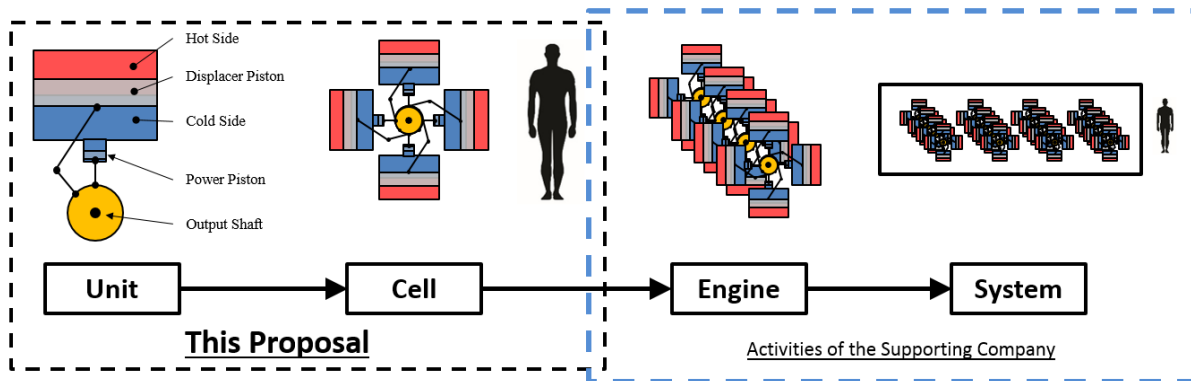


Figure 4: Schematic showing the multi-unit design philosophy to go from a single unit to a complete system

1.4 Aim and Scope

The main aim of this work has been to develop an understanding of what would be the best configuration of Stirling engine for the envisaged low-grade heat applications. To undertake this, a number of constraints have been considered that include materials, manufacturing and mechanical coupling to increase the scale of the power output. A significant focus and aim of this work has been to develop a design philosophy based on mathematical models that can predict engine performance while at the same time taking into account the constraints of the problem. In this report, the major learnings that the group has obtained will be presented and discussed. Topics will range from fundamental thermodynamic modelling, to conceptual multi-unit configurations. For each topic, the impact of the work undertaken will be related to the primary objective of the work, which is to propose the most promising Stirling engine UNIT.

An aim of the original proposal that helped to define the scope of work, was to perform a metric analysis of different engine configurations and make a recommendation of a potential solution which would be the base UNIT. For this to be complete, different engines needed to be designed and CAD modeled, individual thermodynamic models needed to be developed for each configuration, and each engine needed to be constructed and instrumented to allow for the collection of experimental data. A comparison could then be made between the thermodynamic models and the experimental data to determine levels of power output and efficiency. Each of the

four different configurations have proceeded along this path however, there has been limited success in achieving complete end goals. This has been mostly related to the manufacturing of different components to achieve both strength of the components and pressure sealing. Failure of individual components has required redesign of the component and remanufacturing. In some cases, a completed redesign of the engine configuration was needed to address these problems. While every effort has been made to avoid time delays, these issues have limited the success of the project by introducing significant time delays. This report therefore documents the progress in evaluating different engine designs and configurations and provides recommendations that can be made from the work that has been carried out.

2 Methods and Materials

2.1 Mathematical Modelling of the Stirling Engine Cycle

Mathematical models of the thermodynamics of the Stirling engine cycle for the particular configurations under investigation are essential to the design process. As a result, a significant amount of time was spent in development of these predictive models for the engines that are discussed in this report. Predictive models are essential to understand the relationship between the design choices and the resulting output power. Additionally, the development of these models allow the quantification of losses in the system and are required for the future implementation and development of a control system. The approach to developing a model relies on beginning with either isothermal or adiabatic assumptions. By comparing these models to experimental data, higher order decoupled loss models can be developed. These are then used as part of the design cycle to predict engine and system performance.

2.1.1 *Basic physical modeling*

First order performance models, such as the West number, W_n , shown in Equation 1, allow the output power of an engine to be estimated. This type of modelling is based on the assumption that the particular dimensionless number, here the West number, remains constant for a particular engine configuration over a range of operating conditions. An assumption in itself that needs to be tested for the low maximum temperature situation being investigated here. These estimates are used to guide the design, to understand the effect of engine scale and to justify the selection of piston size. The West number relates the operating temperatures, T_H and T_C , to the operating speed, f , the piston swept volume, V and the average operating pressure, P of the engine to offer insight into the effect that these parameters have on the power output of the engine [10].

Table 1: Basic heat transfer equations and important non-dimensional numbers for ideal models of Stirling engines

Eqn 1	$W_n = \frac{W_o}{PVf} \frac{T_H + T_C}{T_H - T_C}$	A : surface area	Q : Heat energy \dot{Q}_{conv} : convective heat transfer
Eqn 2	$\dot{Q} = \dot{m}c_p\Delta T$	c_p : specific heat	ΔT : change in temperature
Eqn 3	$\dot{Q}_{conv} = hA(T_{wall} - T_{fluid})$	f : engine cycle frequency h : convective coefficient L : wall thickness m : mass P : average gas pressure	T_C : abs temperature of the cooler T_H : abs temperature of the heater T_{max} : max available temperature W_o : power output of the engine W_n : West number V : swept volume

The Stirling cycle is driven by energy transfer (Equation 2) to the working fluid, and convective heat transfer (Equation 3) from the heat exchangers to the working fluid. As a result, values such as the specific heat of the working fluid, c_p , the convective heat transfer coefficient, h and the heat exchange area, A , will have a significant impact on the Stirling engine performance. As an example, the specific heat of helium is approximately five times that of air and has been shown to improve the performance of Stirling engines [13].

The low temperature differential associated with the waste heat and geothermal applications of these engines requires the increase of the convective heat transfer coefficient, h and/or the heat transfer surface area, A to improve performance. Thus, in order to increase the amount of useable power for a given ΔT , the engine will need to be made large to allow for a larger heat transfer surface area while at the same time increasing energy exchange between heat transfer surfaces in the working fluid. This approach is opposite to the design approach of typical power dense engine systems. For example, for internal combustion engines the engine design philosophy drives towards a small engine scale with minimal heat or energy transfer to the engine with the aim to maximise energy conversion from the combustion process to rotational motion. However, in these scenarios, a surplus of energy is often available from the exothermic reaction to overcome losses or limitations in the engine design. In the case of the low temperature Stirling engines, the amount of available heat is small, thus to maximize the outputs from the Stirling engine, all the mentioned factors will need to be strongly considered throughout the design process.

2.1.2 First order model – ideal isothermal analysis

The isothermal, or constant temperature analysis of a Stirling engine is the simplest approach used to model a Stirling cycle. The primary assumption used in this model is that the gasses in the expansion and compression spaces are not only at a uniform temperature, but also instantly reach the upper and lower source temperatures after the regenerator [17]. This assumes a perfect energy exchange between the heat exchangers and the working fluid. A schematic of the isothermal model can be seen in Figure 5 where the uniform temperature distribution in the expansion and compression spaces can be seen.

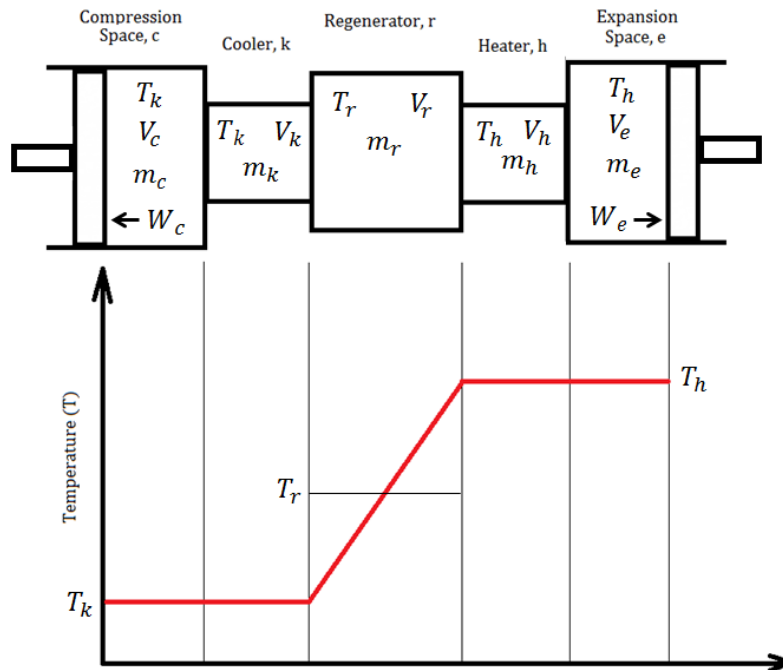


Figure 5: The isothermal Stirling engine model showing (a) the temperature profile through the compression and expansion spaces in the engine, and (b) the resulting indicator diagram where the area inside the diagram represents the indicated power of the cycle

2.1.3 First order model - Adiabatic model

Whereas the isothermal model assumed perfect energy exchange and uniform temperature distributions in both the expansion and compression spaces, the adiabatic model instead treats the expansion and compression spaces as adiabatic or no heat transfer to the environment. As shown in Figure 6, the temperatures of the expansion and compression spaces are no longer constant, but vary over the course of the cycle. Additional assumptions made in the development of the adiabatic model are: there is no gas leakage and that there is no flow friction pressure loss [17]. Unlike the ideal isothermal model, the adiabatic model does not have a closed form solution and therefore must be solved numerically. This will generate a similar indicator diagram as shown in Figure 5 (b) from which the total energy in the cycle can be determined.

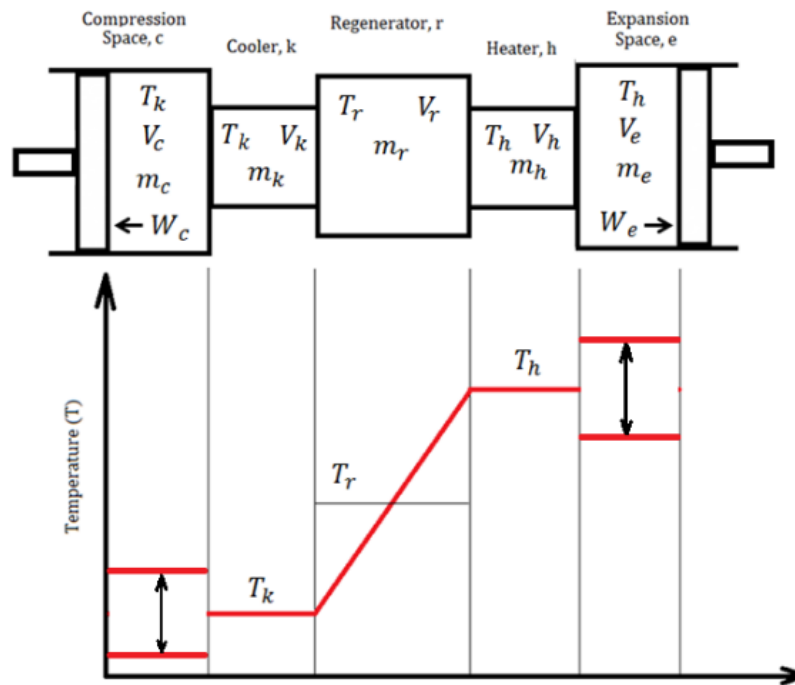


Figure 6: The adiabatic Stirling engine model showing the temperature profile through the compression and expansions spaces in the engine

2.1.4 *Second order models*

Second order modelling assumes that the various engine losses are subtracted from a reference cycle, such as the isothermal or adiabatic model, to obtain a more accurate power estimate. These losses are referred to as decoupled losses and in addition to there being multiple methods to calculate each of these losses, they are dependent on the engine geometry. These include, but are not limited to, the following losses [11]:

- Incomplete gas flushing from the displacer motion
- Mechanical friction
- Flow friction
- Imperfect heat transfer
- Gas spring hysteresis in the crank case
- Mechanical losses (friction and mechanical effectiveness)
- Gas leakage past the displacer piston

To highlight this complex interaction between the design and the specific operating conditions of an engine an example dataset from the model and experiments is shown in Figure 7 collected from the 90° Gamma engine. This plot shows the effect of the gas spring hysteresis inside of the pressurized crank case and shows that this particular loss is affected by both the operating pressure inside of the engine, and the engine speed.

The development of a complete second order model would require similar approaches to be applied to each of the decoupled losses through processing experimental results. Because these losses are related to the specific engine design, this process will be done for each developed engine configuration.

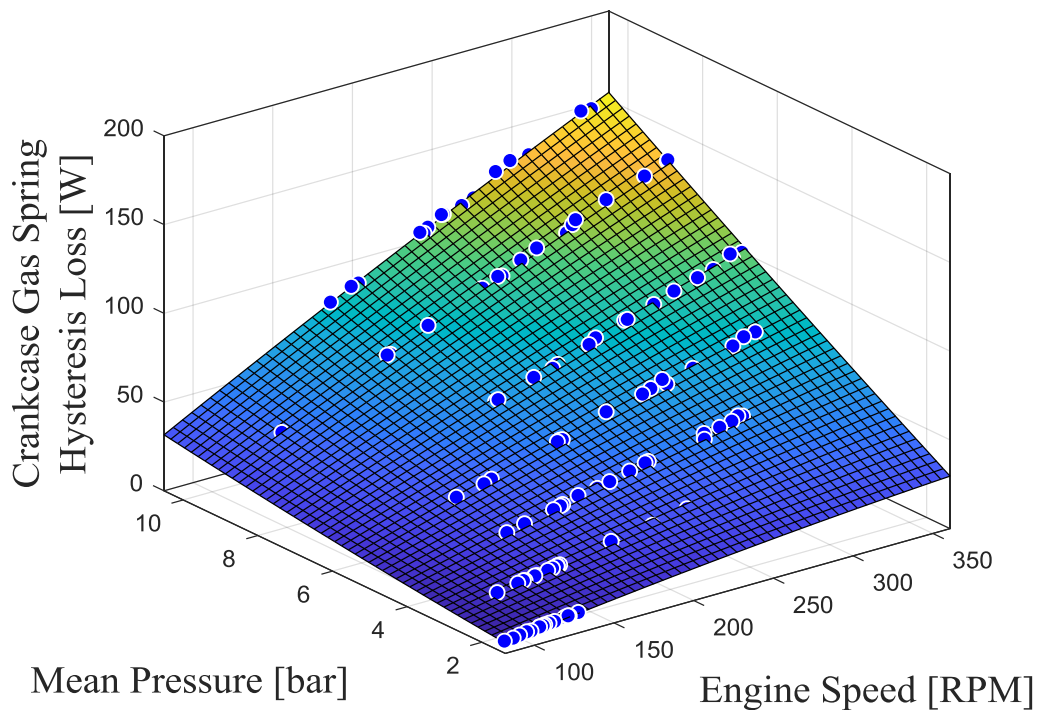


Figure 7: Surface plot showing the effect of engine speed and mean engine pressure on the gas spring hysteresis losses of the 90° Gamma engine. The plane represents interpolated and extrapolated data from the experimental measurements shown with blue markers

A significant body of work in the literature is dedicated to the development of second order Stirling engine models. Formosa and Depesse [18], among many others, added decoupled losses to the isothermal model (Section 2.1.2). They found good agreement between their conduction, regenerator enthalpy, mechanical friction and heat exchanger losses and published results of a GPU-3 beta Stirling engine. A second body of work studied the addition of decoupled losses to the adiabatic model reference cycle. One example of this work is the study done by Strauss and Dobson [19]. They added the regenerator enthalpy and conduction losses to the heat rejection rate rather than the heat input rate and found that when compared to experimental results from the GPU-3 engine, better agreement between the model and experiment was found.

Current experimental results from the 90° Gamma engine are being used to develop decoupled loss models. The experimental work conducted on this engine has allowed the methodology of this approach to be developed. Further results and approaches will be described in later sections of this report.

2.2 Configurations

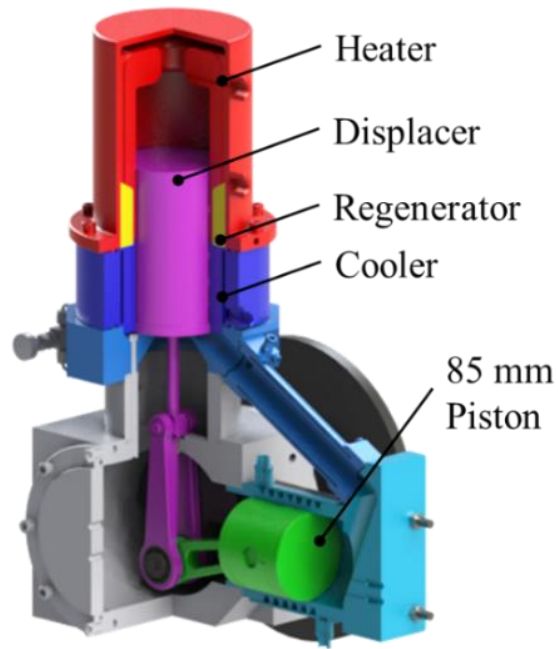
A significant portion of this work involved investigating different configurations of the base UNIT of low temperature energy generation. In terms of Stirling engine design, the engine configuration has a significant influence on the final design. The different engine configurations are defined primarily by the orientation and size of the two pistons that make up a Stirling engine geometry. However, these configurations also have an impact on mechanical coupling, manufacturability, and heat exchanger geometry, ability to service the engines, among many other factors.

For the work undertaken so far, time has been spent on developing five Stirling engines with four different piston geometries. Each of these engines are at a different stage of development ranging from completed and operational, to under-construction. These multiple configurations provide an opportunity to not only validate the existing predictive models, but to also develop higher order models while at the same time assess many other parameters that may affect the overall success of the particular unit. For each of the configurations, a minimum of a first order thermodynamic model has been developed to predict performance. Each initial design was manufactured to the limit of the lab-scale capabilities, and these designs and limitations will be discussed in upcoming sections of this report.

2.2.1 The 90° Gamma

The 90° Gamma Stirling engine shown in Figure 8 (a) was designed and built based on a ST05G Stirling engine design [20] for which a number of research investigations have been undertaken in the literature. A portion of the development of this engine involved adapting the design for operation with a lower hot source temperature compared to the original design temperature of 650 °C. This was done by reducing the diameter of the piston from 85 mm to 44 mm, as shown in Figure 8 (a). With the 85mm piston, the engine was run at a source temperature of 400 °C. The piston modifications allowed the engine to operate with a source temperature as low as 135 °C [21]. The development of this engine was accompanied by the development of a complete instrumentation system. This is shown in Figure 8 (b) and a description of all the instrumentation used is given in Speer *et al* [21] and the thesis by Speer [22].

One of the main advantages of this configuration is the compact crank mechanism. Both the displacer and the piston share a plane of symmetry normal to the output torque, which improves the simplicity of the mechanism design. Additionally, the co-planarity of the pistons simplifies the crank-shaft supports. Simplifying the mechanism is valuable in the Stirling engine design as it reduces the presence of tolerance stack and increases the mechanism effectiveness [9]. Another advantage of this configuration is the completely enclosed crankcase. This allows pressurisation of the crank region minimising the pressure drop across the power piston affecting the overall force work generated.



(a)



(b)

Figure 8: The current 90° Gamma engine shown as (a) an annotated solid model render and (b) and digital image of the experimental setup

2.2.2 The In-Line Gamma

The In-Line Gamma (ILG) is shown as a CAD model in Figure 9 (a) and built in Figure 9 (b). This configuration is defined by a collinear displacer and piston motion. The red, blue and green features in Figure 9 (a) are custom designed heat exchanger components with flow channels, flanges with captive nuts, and fluid inlet and outlet ports. The manufacturing of this geometry was achieved using 3D printing techniques.

To heat and cool the fluid, the ILG uses multiple stages of flat plate heat exchangers, both in the retaining plates above and below the displacer, as well modular sections on either side of the regenerator housing. Each flat plate heat exchanger has a 3D printed water jacket with flow channels that directs the hot/cold water across the plate. The performance of these types of heat exchangers were characterized in oscillating flow by Stumpf *et al* [23].

The way in which this configuration was designed has the piston mounted on top of the displacer; requiring additional distance to be placed between the mechanism and the engine body. This affects the design of the ILG in several ways. The increased distance between the mechanism and the engine body increases the overall unit height, thus decreasing the number of units and cells which can be arranged in the future working space. This increased distance, over which components must be rigidly connected, will also require a greater control over manufacturing tolerances to ensure proper alignment and concentricity of the shafts and pistons, potentially increasing the production costs of each unit.

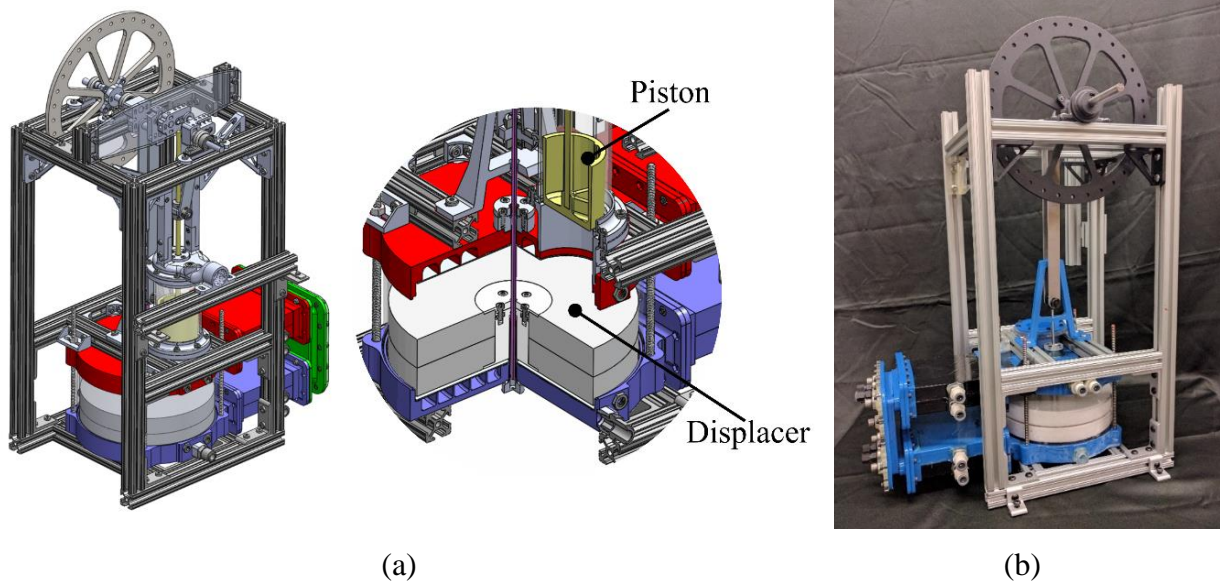


Figure 9: The current in-line Gamma shown as, (a) a solid model of the system and (b) a digital image of the constructed engine

2.2.3 The increased scale In-Line Gamma

Requirements from collaborative partner Terrapin Geothermics prompted the design of a second in-line Gamma engine (Terrapin ILG) at a larger scale with an emphasis on standard components for the displacer cylinder and body. The CAD model is shown in Figure 10 (a) and the physical build, in Figure 10 (b). The engine body is made up of size 12 ANSI 150 weld neck and blind flanges and the displacer cylinder is made of standard pipe sleeves. The chosen set of materials ensure a leak-free body, which can be safely pressurized to different charge pressures. The benefit of this construction is that it provides a robust engine body which can be reused. One example of this is the development of a new mechanism, which can be integrated with this body made from standard pressure retaining components.

This increased scale of the Terrapin ILG configuration has a similar geometry to the ILG discussed in Section 2.2.2. The primary difference between this In-Line Gamma and the previously discussed design are the finned tube heat exchangers which is seated between the annular space between the displacer cylinder and the inner bore of the weld neck flanges. This type of heat exchanger significantly increases the heat transfer area for heating and cooling the working fluid when compared to a flat plate design and the heat exchanger geometry is an efficient use of this annular space.

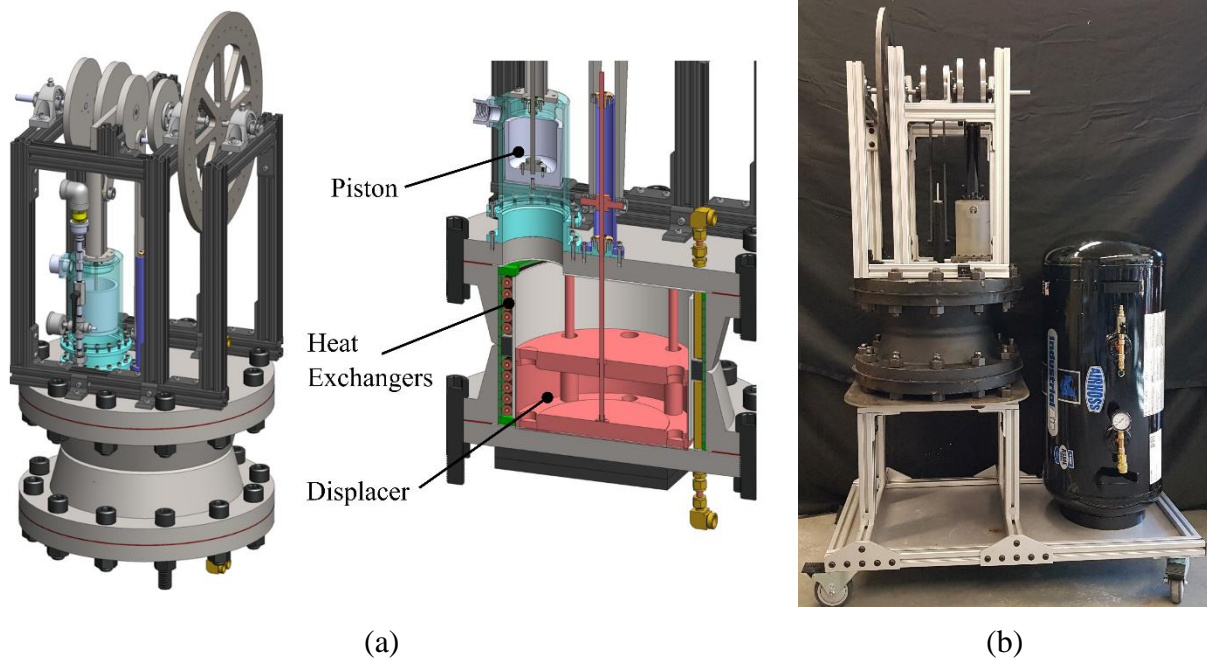


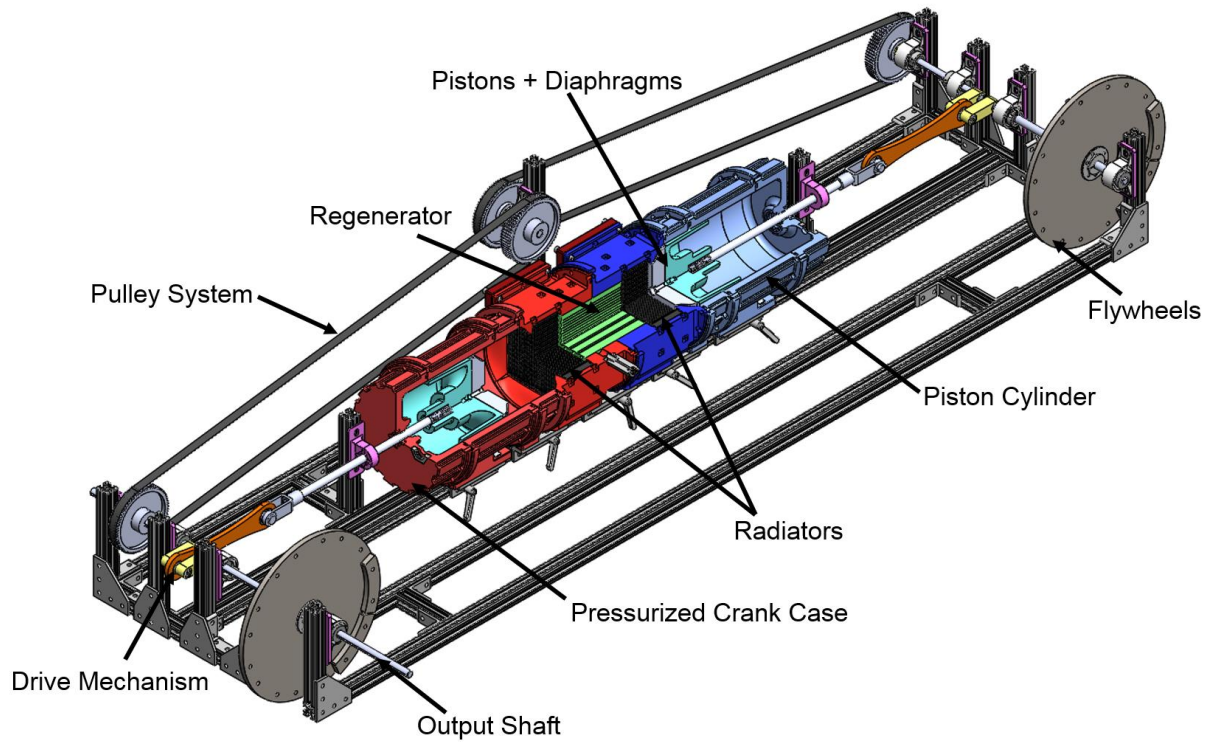
Figure 10: The current Terrapin ILG shown as, (a) a solid model of the system and (b) a digital image of the constructed engine

2.2.4 The Opposed Piston Alpha

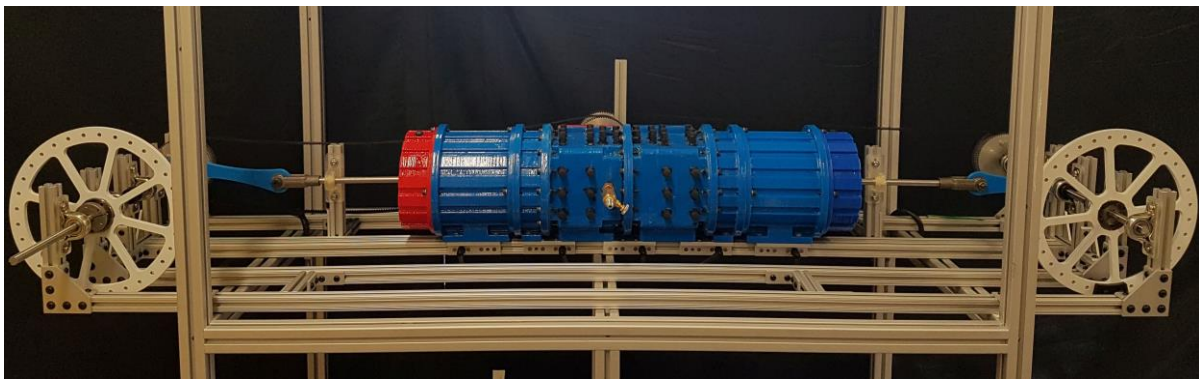
The opposed piston Alpha (OPA) is shown as a CAD model in Figure 11 (a) and in the as-build configuration in Figure 11 (b). The primary difference between the Alpha design and the previously discussed ILG configurations is that instead of a separate displacer and piston, the Alpha configuration has two pistons which are both used to extract work from the working fluid. In the case of the OPA, this manifests itself as two separate crankshafts coupled together. Belts have been chosen in this design to compensate for slight misalignment. The piston motion pushes air through centrally located radiator style heat exchangers.

The selection of these heat exchangers prompted some additional work to be undertaken on characterizing their performance in a reciprocating flow field. Nusselt number relationships exist for steady flow, which is a flow regime that is not seen in Stirling engines. Experimental setups were developed by Michaud *et al*, allowing these radiator style heat exchangers to be characterized for pulsatile [24] and oscillating flow [25]. The results from this analysis, and the simple through-flow of these heat exchangers add merit to the use of radiator style heat exchangers.

The first advantage of this design is the symmetry of the configuration, which reduces the number of unique parts to manufacture. From the as built image shown in Figure 11 (b), the entire tubular body of the engine was made using 3D printing technology. The second strength of the OPA is the comparatively simple crank mechanism. With each piston having its own crank shaft, concentricity between the pistons and the cylinders is simpler to achieve compared to the Gamma engine, where the pistons are rigidly coupled onto the same assembly. Additionally, the ability to use belts for power transmission allows for a looser tolerance for alignment and position of the shafts and pulleys, which suit the reduced precision associated with the 3D printing processes when compared to traditional machining.



(a)



(b)

Figure 11: The current opposed piston Alpha shown as, (a) a solid model and (b) a digital image of the constructed engine

2.2.5 The Franchot Double Acting Alpha

The final configuration is the Franchot double acting Alpha and is currently early in the design phase. Similar to the OPA, the Franchot also has two power pistons, which is characteristic of all Alpha configuration Stirling engines. The unique aspect of the Franchot compared to all other configurations is that it is a double acting Stirling engine, meaning that a single Franchot unit contains two closed systems, simultaneously undergoing separate Stirling cycles. This offers certain advantages, one being that there is no longer the need to have a pressurized crank case because each side of the piston is in contact with the working fluid [26]. Like the OPA, the engine symmetry and the identical pistons reduces the number of unique parts which influences manufacturing cost.

A significant difference in this configuration is the piston geometry. The Gamma and opposed piston Alpha configurations used standard piston geometries in which rolling diaphragms were used to achieve a frictionless seal. In the double acting Franchot, the double acting pistons hold flat polymer diaphragms, separating the two separate working spaces from one another. Flat diaphragms offer the same sealing advantages as rolling diaphragms and were chosen due to unique geometry of this configuration.

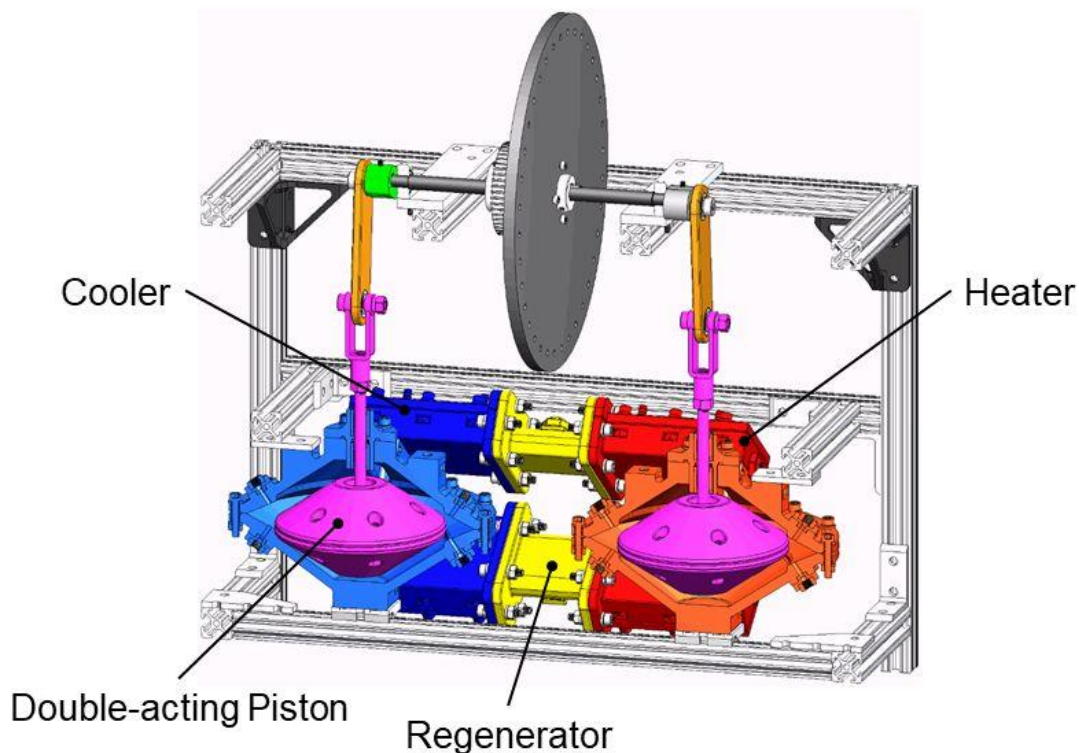


Figure 12: The Franchot double acting Alpha shown as an annotated solid model, indicating the main components of the engine

To test feasibility of using flat diaphragms in this application, an experimental setup, shown in Figure 13, was designed to test the performance of flat diaphragms. This setup uses the identical piston design as the Franchot engine to not only test the performance of various polymeric materials, but to also test the ability of the pistons to hold the diaphragms in place.

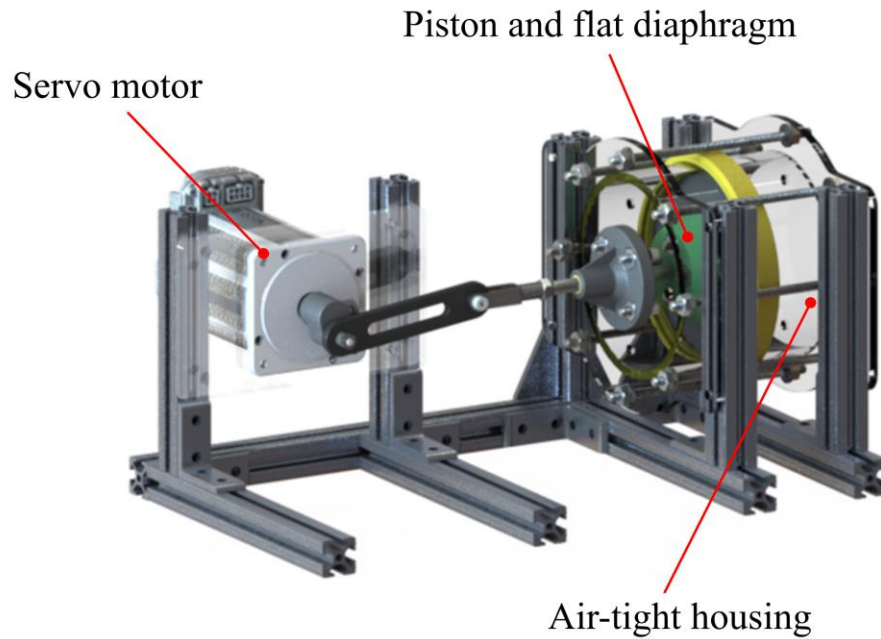


Figure 13: Solid model render of the flat diaphragm testing setup designed to test the function of the piston/diaphragm system which will be used in the Franchot double acting alpha

2.3 Engine Test Bed

To test the validity of the developed thermodynamic models, engine parameters are measured experimentally. These parameters include operating temperatures, operating pressures, engine speed and the developed torque. To measure these, a custom-built engine test bed was developed that included appropriate instrumentation, data acquisition system and custom written software to both monitor the engine and collect data.

2.3.1 *Data acquisition system*

A data acquisition system was developed to record and display temperature, pressure, torque and encoder data from the UNITS. The hardware, shown in Figure 14 consists of multiple data acquisition units and is run from software which was written by DTECL in a commercial programming environment (Lab Windows CVI, National Instruments Inc.). A screenshot of a sample user interface is shown in Figure 15. This data acquisition system was designed to be a multi purpose acquisition unit, and each of the UNITS described in Section 2.2 have been designed to ensure compatibility with this data acquisition system. This is an essential laboratory system required to assess the performance of the developed engines and will be heavily used in the continuation of this project.

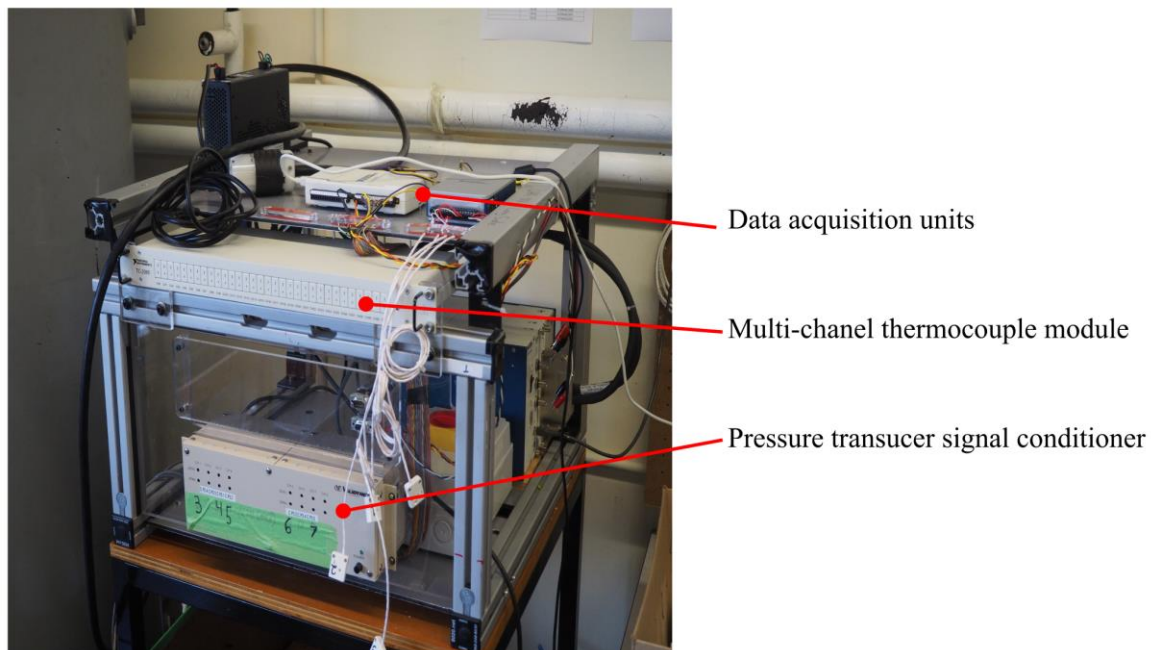


Figure 14: Annotated image of the multi-purpose data acquisition system used to monitor Stirling engine performance

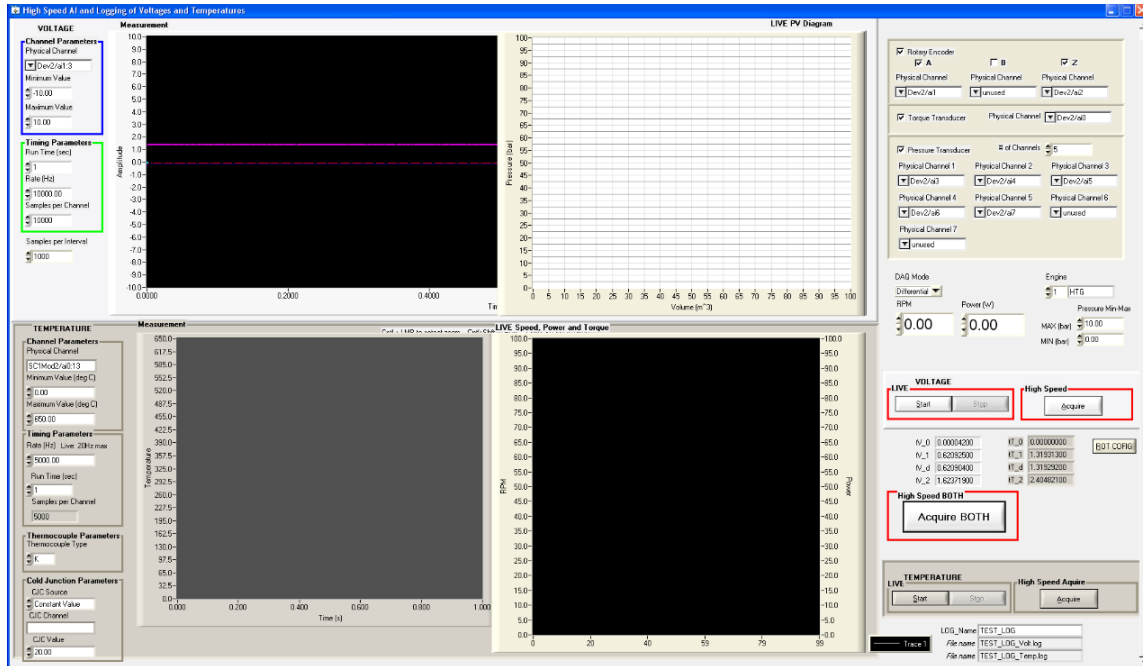


Figure 15: Screenshot of the user interface for the data acquisition software that includes real-time monitoring and long-term data acquisition at defined test conditions.

2.3.2 Engine control

The development and validation of the models described in Section 2.1 combined with the necessary systems to measure the engine performance are necessary for the design of an on-board control system for controlling engine inputs. These include the heating and cooling loads applied to the engine. By varying these inputs, the output power and engine speed can be controlled. Work completed as a part of this project, such as the development of predictive models and a complete data acquisition system are critical to the framework of such a control system. However, before such a control system can be developed, a better understanding of the losses in these systems is required to develop higher order predictive models. Once these models have been established, an on-board framework will be required to monitor and control the performance of each unit independently. This can be done using single board computers and microcontrollers.

2.4 Design considerations

2.4.1 *Use of rapid prototyping*

3D printing technology based on fused deposition modelling (FDM) and stereolithography (SLA) technologies were commonly used tools in this project. These tools allowed components with complex geometries to be produced rapidly at a relatively low cost. These two 3D printing technologies differ fundamentally from one another. FDM printers melt and extrude thermoplastics to form parts whereas SLA printers use a tray of liquid photosensitive resin and a UV laser. Commercial systems made by Ultimaker [Ultimaker, Geldermalsen, Netherlands] and FormLabs [Formlabs, Somerville, MA, USA] , shown in Figure 16, use the FDM and SLA approaches respectively.

Rapid prototyping allows unique geometries to be manufactured. In the images shown in Figure 17, complex geometries such as captive nuts, pipe threads and large diameter circular bores with custom flanges are just a small subset of what can be produced with 3D printing. The availability of this technology allows sophisticated designs to be implemented without incurring long time delays and manufacturing expenses.

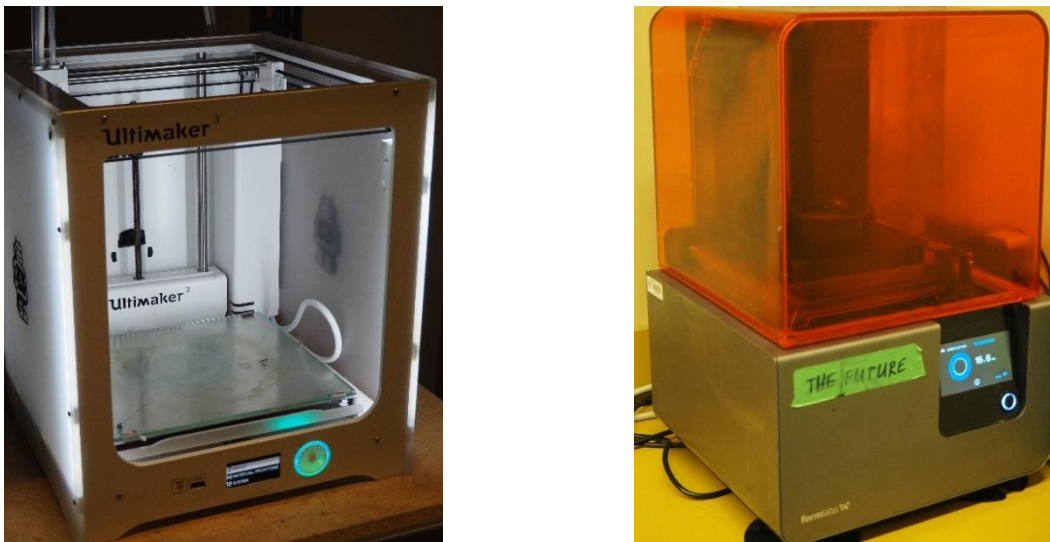


Figure 16: Images of the additive manufacturing technology used, (a) FDM Printer (Ultimaker 3) and (b) SLS (Form 2)

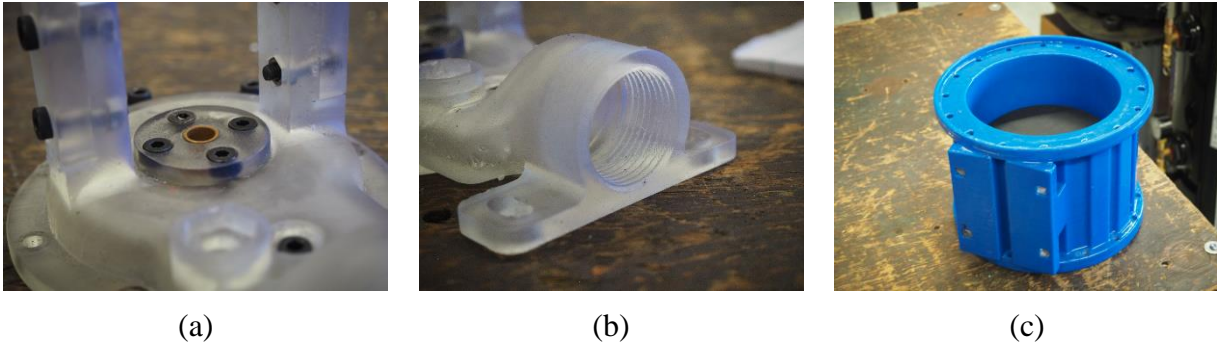


Figure 17: Images of typical parts manufactured with the different 3D printing technologies, the translucent parts in (a) and (b) were printed using SLA technology and shows the ability to imbed fasteners and bushings (a) and the ability to print threads (b). The blue part shown in (c) was printed with the FDM printer and allows complex structural components to be manufactured.

Each of the 3D printing techniques are accompanied by their own set of limitations, which can be broken down into three categories: the available materials, the precision of the printing technique, and the printing technology itself. A breakdown of these limitations can be found in Table 2.

Table 2: Comparative table of limitations for FDM and SLA printing

Limitations	FDM	SLA
Material	Thermoplastics only	Proprietary resins only
Precision	Limited by nozzle size, axis alignment	Limited by focused mirror
Printing technology	Heating effects	UV effects

The material limitation is a result of the fundamental printing mechanism used in each of the techniques. The melting process used in FCM printing requires thermoplastics, and the SLA process requires a liquid thermosensitive resin.

The precision of the two types of machines is dependent on the physical calibration of the machines. However, due to the different physical mechanisms, FDM printers are more susceptible to inaccurate calibration. The print head in FDM machines must physically move the length of the build volume and any misalignment of the machine axis will result in dimensionally inaccurate parts. On top of this, the nozzle size, which is typically 0.4mm or greater, dictates the smallest printable feature. SLA printers use rotating mirrors to direct the focused laser – which eliminates the need to have significant motion of any of the components. Additionally, the spot size of the laser, which dictates the smallest printable feature, is much smaller than that of an FDM printer allowed for print features down to ~50µm.

The type of printing technology also has some limitations that affects the printing process and lifetime of the printed parts. The melting process of FDM printers creates a heat distribution through the part during the printing process. For certain materials, such as ABS, this can cause warping and cracking of the part, leading to an increased number of failed prints. For SLA printed

materials, the UV sensitive nature of the parts means that excess exposure to the sunlight. The consideration of these limitations requires experience and understanding of the machine, and the intended use of the components to be printed in order to select a technique that best suits the application.

2.4.2 *The effect of 3D printing on the design*

The materials used in FDM machines were selected based on the needs of the project. ABS plastic is a commonly used 3D printing material and was extensively used in this project due to its thermal properties. The point at which ABS begins to lose its rigidity, the glass transition temperature [27], is higher than the expected hot side temperature of $\sim 90\text{ }^{\circ}\text{C}$ and can therefore withstand the thermal loads from the expected temperatures within the engine. A combination of the material properties, commercial availability and the existing material property literature [28]–[30] make ABS a good choice for the chosen application.

The use of this technology has influenced the scale of the printed parts. The largest printer that was available for use had a build volume of $223\times 223\times 205\text{ mm}$ and this drove the maximum dimensions of certain components, namely the diameter and the length of the cylindrical pieces of the OPA described in Section 2.2.4, shown in Figure 18. When the engines need to be scaled up beyond the size limits of the 3D printers, 3D printing technology will remain useful, by reserving its use for smaller, non-structural components

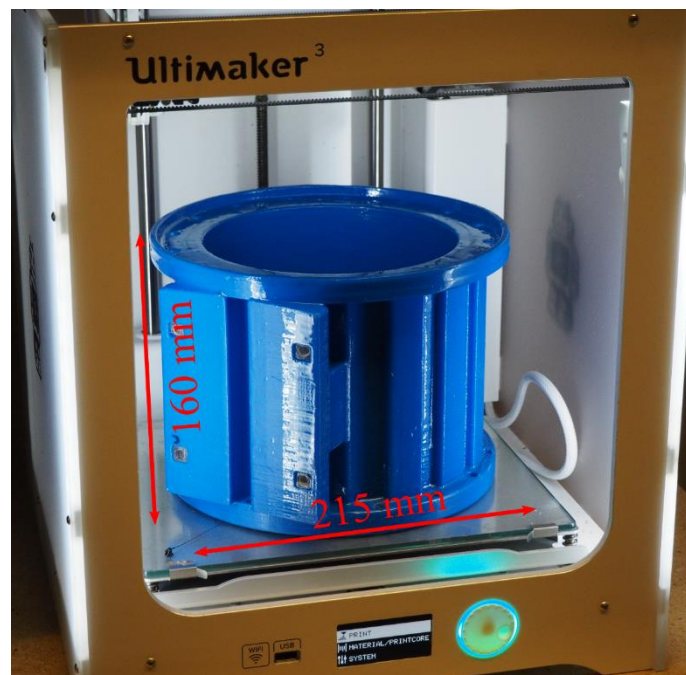


Figure 18: Schematic of a component of the OPA which was designed according to the maximum dimensions of the 3D printing build volume.

2.4.3 Use of rolling diaphragms

The seal between pistons and cylinders in modern engines is accomplished with high precision machining. However, the use of rapid prototyping and polymer materials does not give this same level or precision at the expense of lower cost and the ability to generate more complex geometries. A solution to these issues lead to the use of rolling diaphragms, which are polymer coated textile fabric components, shown in Figure 19.

The textile gives the components additional strength and allow for an air-tight seal between a properly designed piston and cylinder. To ensure proper function, piston design guidelines are provided by the diaphragm manufacturer [31]. The rolling action of the diaphragm also decreases the friction between the piston and cylinder, allowing 3D printed polymeric materials, which typically has high surface roughness compared to precision ground metals, to be used for these components.



Figure 19: An example image of a rolling diaphragm. These types of devices are used to create a frictionless seal between the piston cylinder and piston. Different sizes are used for each of the different configurations

2.4.4 Materials for strength and heat transfer

The range of operating temperatures for this project introduce opportunities for previously unused materials in Stirling engine design. With the comparatively small amounts of heat that accompany these lower temperature differences, unwanted heat transfer and heat losses become increasingly undesirable. The ideal scenario is an adiabatic one, where the only energy transferred to the environment is in the form of work, in this case, shaft work [26]. Thus, being able reduce the amount of heat transferred to the environment benefits the application.

Thermal conductivity is a measurement of the ease at which heat can flow through a certain material. The smaller the value for a particular material, the greater the resistance to heat flow. Figure 20 shows a plot of the melting point of various materials verses thermal conductivity. This plot shows three distinct zones: materials with high thermal conductivities, such as aluminium and copper, high melting points and low thermal conductivities, such as steel and Inconel and insulator materials with low thermal conductivities, consisting of polymers and casting metals.

Copper and aluminium are typically chosen as heat exchanger materials due to their high thermal conductivity values and would not be suitable choices for insulated structural components. Material selection for traditional Stirling engine design has been limited by conditions imposed by the hot source temperature. Materials such as steel and Inconel offer a suitable melting point for the high hot source temperatures, however, their thermal conductivity values still allow a significant amount of heat to be lost to the atmosphere. By reducing the expected hot side temperature to $< 100\text{ }^{\circ}\text{C}$, polymers, such as ABS and Nylon can be used as structural components. These materials succeed as insulators, which better aligns with the adiabatic assumptions, and have thermal conductivity values which are 2-3 orders of magnitude smaller than aluminium and copper.

ABS, Nylon and other thermoplastics are used by rapid prototyping technologies, highlighting that these materials can be used to manufacture complex components. Complex flow channels, flow elements and instrumentation ports can be manufactured out of insulator materials, which suit the low temperature applications of this project.

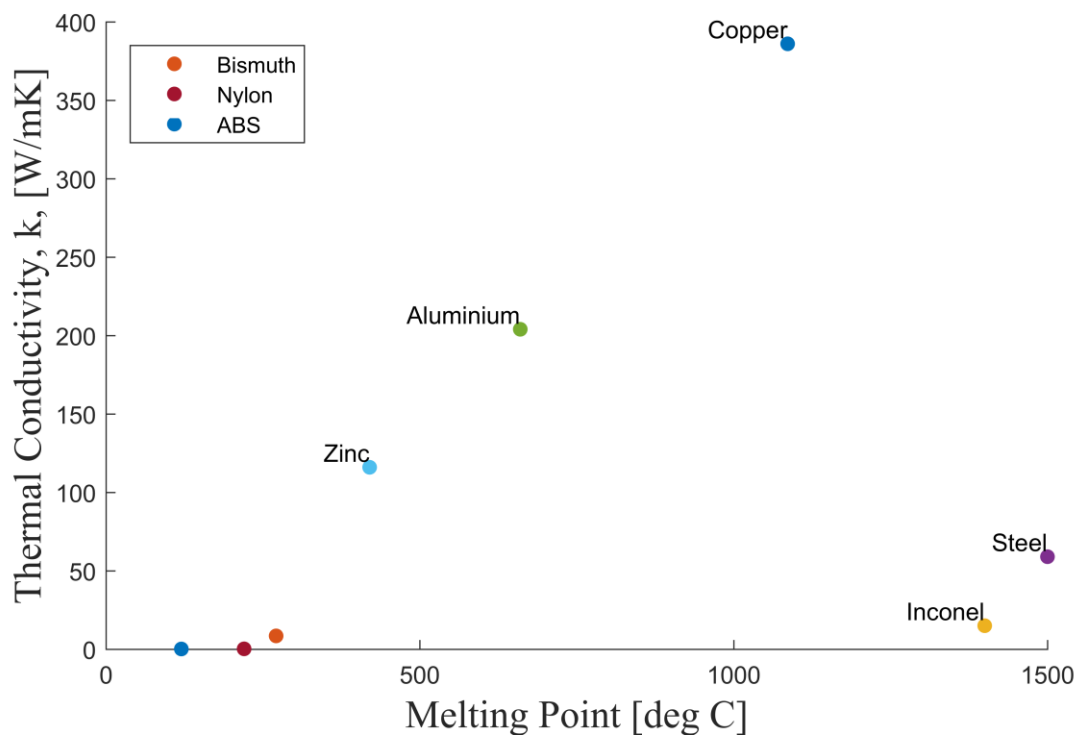


Figure 20: Thermal conductivity versus material melting point for common metal and polymeric materials which shows the low temperature insulators (Nylon, ABS, bismuth), the high temperature insulators (Inconel, steel) and the highly conductive metals (zinc, aluminium, copper)

3 Results and Discussion

In support of the overall aims of the project a number of experimental tests were conducted on the UNITS as they became available after manufacturing. A significant component of this work was in conjunction with bringing the UNITS to a readiness for testing such as pressure testing and determination of individual losses. While all testing work is not documented here an overview of the results are discussed in this section.

3.1 Limitations in the project

The general overall goal of the project as described in the original plan was to make recommendations on what would be the best configuration of Stirling engine for the low temperature application. This could then be used as a UNIT to form individual CELLS. While the work has progressed in this direction there have been limitations in the amount of progress that was originally anticipated. The following outline some of these limitations and provides examples to highlight the issues as well as the steps taken to resolve them.

3.1.1 Generating reliable parts from additive manufacturing

A considerable amount of work was undertaken to develop an understanding of how to properly use the 3D printing technology that was discussed in Section 2.4.2 for engineering design. Achieving the required level of precision and repeatability out of these machines required a much deeper level of understanding than the basic recommended settings.

A significant number of parameters can be changed when preparing the machine code for an FDM printer. These include, but are not limited to:

- Bed temperature (as a function of layer number)
- Nozzle temperature (as a function of layer number)
- Filament retraction distance and speed
- Travel speed
- Printing speed, acceleration and jerk
- Infill percentage
- Wall thickness
- Number of solid layers
- Minimum layer time
- Layer height
- Support material height, offset, density and position
- Extrusion multiplier

These parameters are a subset of what must be chosen to print a part and these are in addition to the motor calibration factor that is required to ensure the machine will produce dimensionally accurate parts. In order to improve the quality of the printed parts and to reduce the number of print failures, calibration pieces must be printed numerous times and must be visually inspected and measured. To determine the optimal slicing settings, troubleshooting approaches, such as those listed in Table 3 are used iteratively, which are specifically for FDM printing technology.

Table 3: Common 3D printed part issues and solutions for troubleshooting

Issue	Possible solution
Poor finish on overhangs	Nozzle temperature too high, or support material is required
Stringing between features	Increase filament retraction distance or speed
Gaps in top layer of part	Increase infill percentage or number of solid layers
Part warping	Increase bed temp or add adhesive aid
Poor surface finish on sides of part	Possible vibrations in mechanical components
Deformation of small features	Decrease nozzle temperature or increase minimum layer time

The physical scale and duration of the major FDM prints (potentially >50 hours) increased the chances of print failures. These most commonly came in the form of print warpage due to large thermal gradients throughout the ABS part. The heated bed is maintained at a temperature of approximately 100 °C, and the current layer is extruding at 260 °C. The layers in between cool to a temperature above room temperature. These gradients can cause significant warpage, which can ruin flat mating faces and can cause interlayer fracture. The as-built design of the Ultimaker printers do not have an enclosed volume, which means that buoyancy effects will constantly remove the heat from the heated bed. By insulating these machines, the magnitude of the thermal gradients was reduced by allowing a temperature of 50 °C to be maintained within the printer volume. This insulation, combined with development of an optimal printing profile, significantly reduced the number of print failures.

3.1.2 Using 3-D printed components under pressure

The majority of the large FDM components were either for heat exchangers or for engine body components and proper function of these components require that they be air/water tight. For all of these components, post processing techniques were developed to prepare the surfaces of the parts.

Acetone smoothing is a commonly documented process for improving the surface finish of 3D printed thermoplastic parts [32] and was commonly used in the early stages of this project. This process consists of placing the part in contact with acetone vapour and allowing the acetone to diffuse into the part and to dissolve and remodel the outer surfaces to smooth the layer lines and to fill in small regions of under-extrusion.

An undocumented effect of the acetone smoothing process however was not discovered until heat-exchanger tests on the ILG engine were being conducted. After the smoothing process, the 3D printed parts must be given a sufficient amount of time in a well-ventilated environment to allow the acetone that has diffused into the part, to diffuse out of the part. If this does not occur, the acetone vapour can boil and destroy the part, especially when the part is heated. This occurred to a hot side heat exchanger on the ILG engine and the results of this are shown in Figure 21.

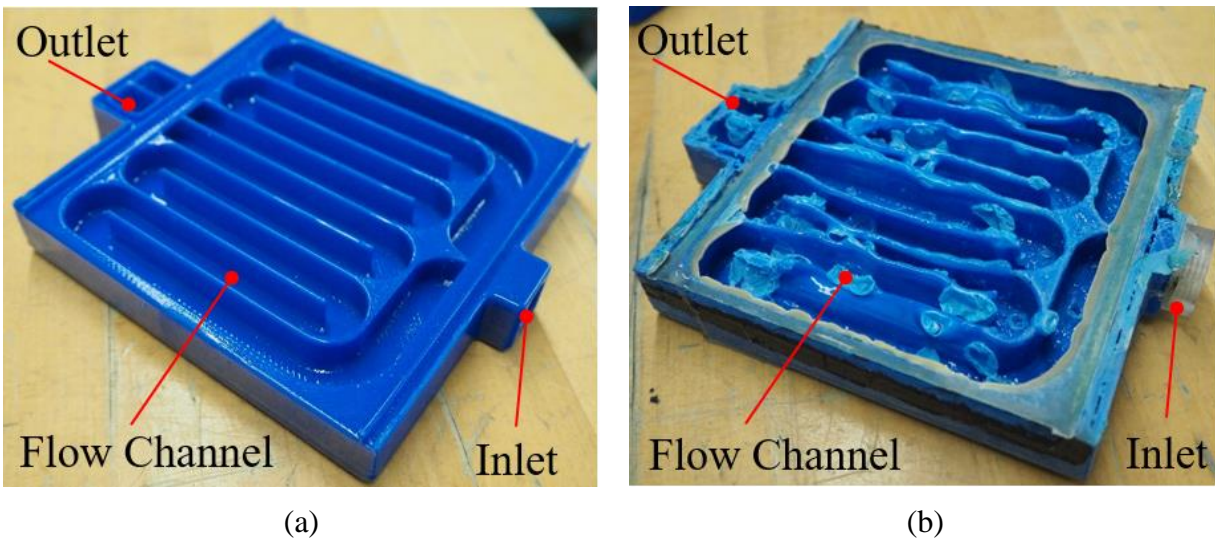


Figure 21: Comparison between the as-printed water jacket (a) and the damaged water jacket from heated residual acetone from the acetone smoothing process

The undesired effects of the acetone smoothing motivated the use of epoxy coatings in place of a chemical process. The epoxy coatings have the same benefits as acetone smoothing with the additional advantage that the epoxy does not change the chemistry of the material and will not end up altering the material properties in an undesired way.

The construction of the OPA required a large, multi-piece, 3D printed body to be sealed. Throughout the manufacturing process, several issues were encountered. These include interlayer cracking around instrumentation ports and several poor gasket and o-ring surfaces. Any issues related to small cracks were resolved with the epoxy coating, which was previously discussed.

Improving the sealing surfaces for the o-rings and gaskets required the use of soft silicone. This allowed the large imperfections to be filled, and the undesired surface curvature to be compensated for. The result of this process is shown in Figure 22. Using these techniques as post processing methods allowed the number of leaks in the OPA body to be significantly reduced.

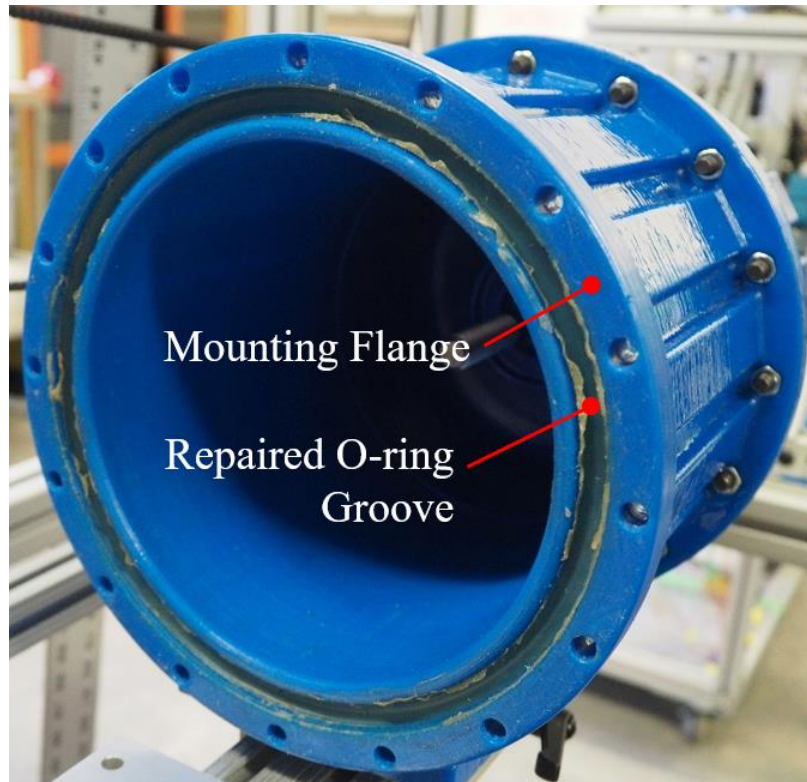


Figure 22: O-ring groove of a 3D printed part which has been filled with silicone to repair imperfections from the printing process

The design of the flat plate heat exchangers used in the ILG engine (shown in Figure 26) required bonding aluminum plate to 3D printed water jackets. Bonding the two materials together using epoxy and silicone created a water-tight assembly, however, the difficulties in maintaining a seal in the heat exchangers arose from the differences in thermal expansion coefficients between the two materials. It was found that the water flowing through the heat exchangers had to be slowly heated or cooled to reach the desired end point and if the temperatures became too hot/cold, the epoxied interface would crack, causing a leak. This issue is ongoing and the difficulty to manufacture heat exchangers made from metal and 3D printed materials makes a strong case for using purchasable heat exchangers, such as copper coils and radiators.

3.1.3 The effect of forced work

Forced work is a phenomenon that occurs when the velocity vector of a body opposes the balance of forces on a body, as shown in the block diagram in Figure 23. A major component of the research activities has been to develop an approach for modeling forced work as well as mechanically implementing solution. This was based on the work of Senft who first identified the effect that forced work has on Stirling engine design [26].

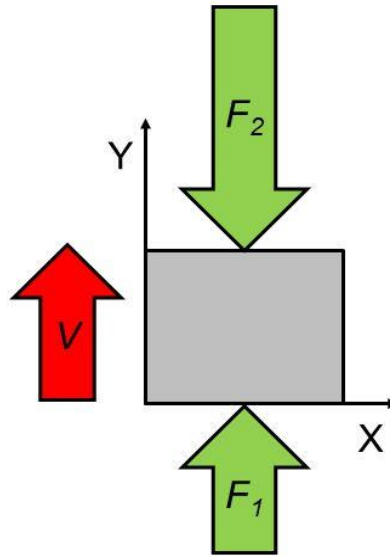


Figure 23: An image of the forced work concept which shows the block motion is in the opposite direction of the net force applied to the block

Forced work will always occur within the Stirling cycle of a Stirling engine with traditional slider-crank based coupled pistons. This will occur when there are differences between the buffer pressure, which is the pressure acting on the non-working space side of the piston and the pressure of the working fluid inside the expansion cylinder [26]. This can be seen in Figure 24 where the regions that forced work can occur in the cycle are shown in red. Improving engine performance through the reduction of forced work involves minimizing the difference between the buffer pressure and the engine pressure. A number of approaches have been used to reduce the effect of forced work. These include the use of a pressurized crank case to increase the pressure at the non-working fluid side of the piston, and springs pressing against the piston during the expansion phase of the Stirling cycle.

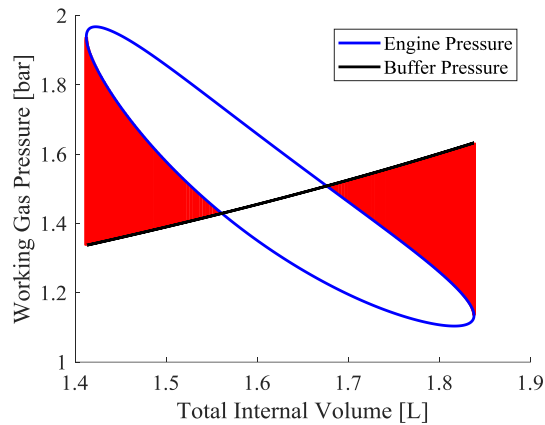


Figure 24: A simulated indicator diagram shown in blue, with a linear buffer pressure shown in black and the forced work is shown in red

Developing an understanding of how forced work affects Stirling engine performance has affected the Stirling engine design process with regards to this project. The inclusion of forced work in the predictive models allows operating conditions to be determined for which an engine can and cannot run. From the perspective of forced work, a scenario where an engine can run means the area enclosed by the forced work in red is less than the area inside the loop of the indicator diagram. This means that with a properly constructed engine, there will be a sufficient amount of work to overcome the forced work in the cycle. This modelling also gives an understanding of operating conditions that will be unsuccessful. Figure 25 (b) shows the indicator diagram of a system with a buffer pressure that is significantly higher than the maximum cycle pressure, resulting in a greater amount of forced work compared to the indicated work.

The effect of forced work has led to an understanding of the importance of being able to manipulate the buffer pressure of the system. This has motivated many design decisions, including pressurized crank cases, springs on the non-working side of the piston and the purchase of high precision pressure controllers which allow engine operating conditions to be accurately controlled.

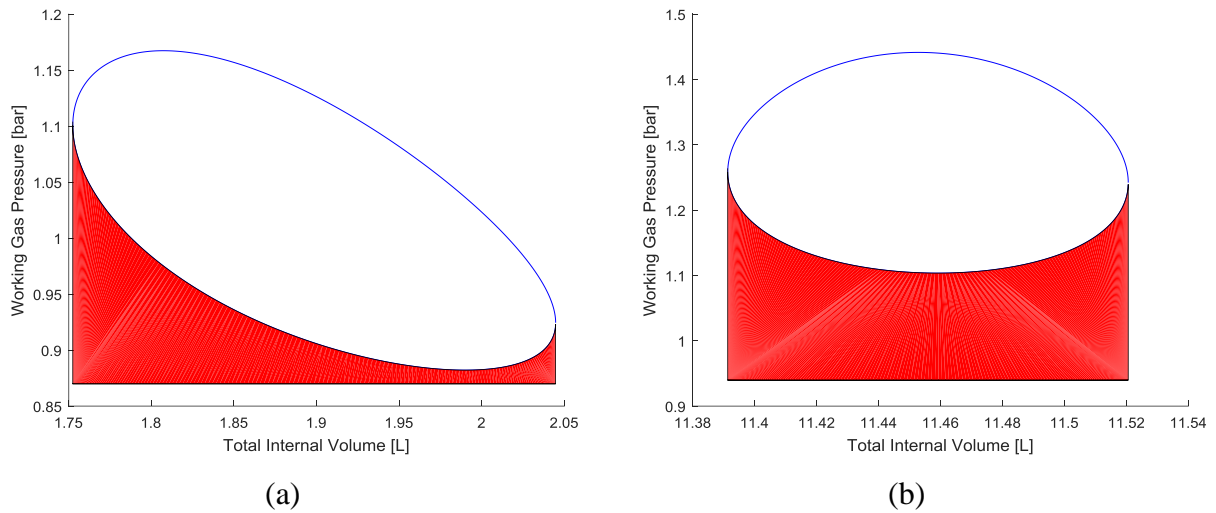


Figure 25: Simulated indicator diagrams with two different buffer pressure conditions leading to (a) positive work due to a greater amount of indicated work compared to the forced work, and (b) negative work due to the a lesser amount of indicated work compared to the amount of forced work

3.1.4 Heat transfer in reciprocating systems.

Over the course of the project, engine design and heat exchanger characterization were undertaken in parallel. Fundamental research has been done regarding the reciprocating heat transfer in ideal geometries, however, for more complex geometries, such as the ILG heat exchangers, shown in Figure 26, experimental work was conducted on the as-built geometry [23].

Conducting these experiments on the as-built geometry lead to a better understanding of the implications of the heat exchanger selection on the engine design. For the ILG engine, discussed in Section 2.2.2, the current scale flat plate heat exchangers did not have sufficient heat transfer area. The engine would slow down and dwell for periods of time while operating to allow for more heat to be added to the system.

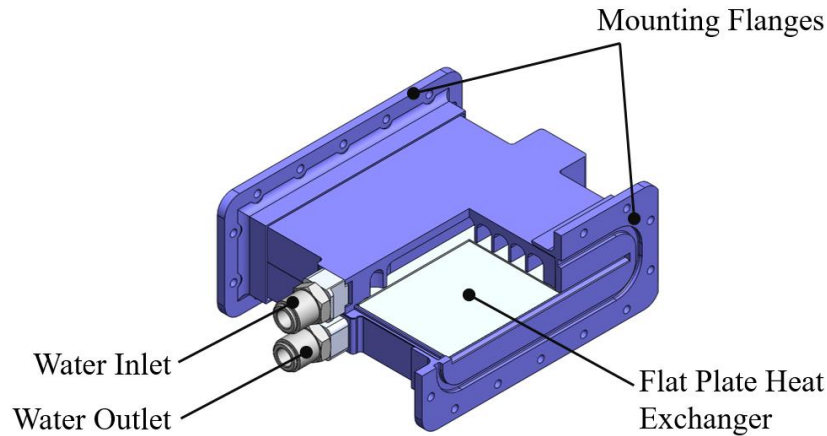


Figure 26: CAD solid model section view of a flat plate heat exchanger on the ILG engine showing the tube inlet, outlet and water channels

These issues were addressed when designing the increased scale ILG, discussed in Section 2.2.3. Annular finned tube heat exchangers placed in cross-flow were used to significantly increase the heat transfer surface area. The fin size and number of tubes were determined through engineering simulations. However, when the gas temperatures were measured, they were significantly different than expected. Water at 95 °C and 2 °C were used for the hot and cold sides of the engine respectively and the displacer was raised and lowered to flush the air across the heat exchangers. The results from this test are shown in Figure 28 and shows that there is a temperature differential of less than 10 °C between the hot and cold sides of the engine.

These findings are the result of the thick steel flanges used in the construction of the engine. The 40mm thickness of the blind flange makes it difficult to properly sample the gas temperature without making contact between the steel and the thermocouple tip and the high heat capacity of the steel acts as a cold sink, which creates additional heat transfer losses on the hot side of the engine. To address both of these issues, an acrylic flange has been manufactured and the engine is currently being rebuilt to allow the installation of this component. Additional thermocouple ports have also been added to better diagnose the effect of the heat exchangers.

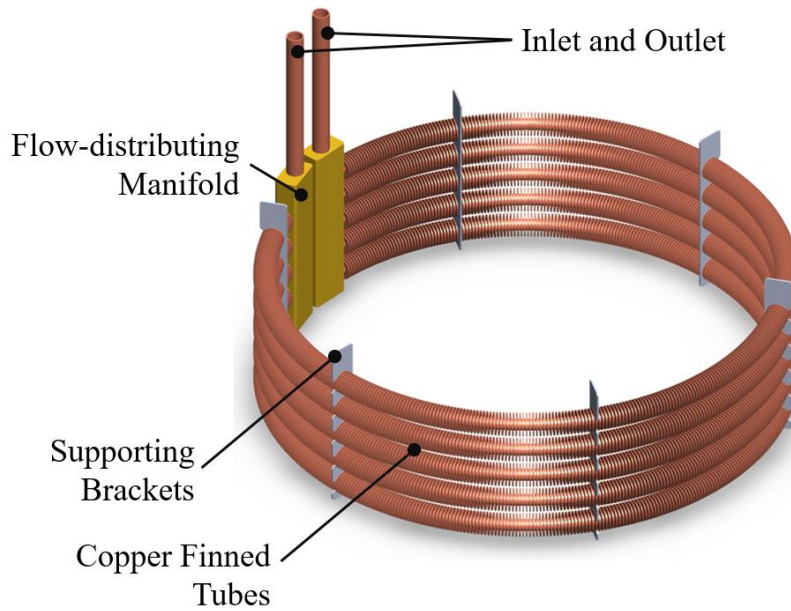


Figure 27: CAD solid model of an annular finned tube heat exchangers in the increased scale ILG

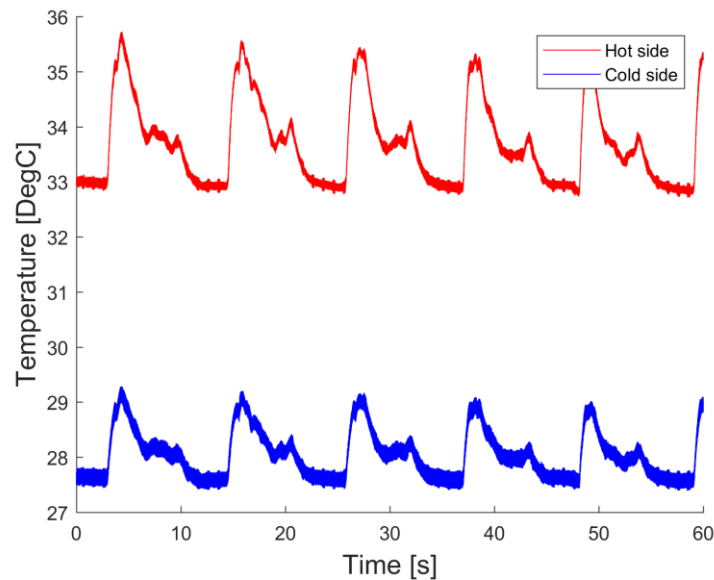


Figure 28: Experimentally measured hot and cold wide gas temperatures as a function of time from increased scale ILG engine. The displacer was moved between top and bottom dead center and allowed to dwell for five seconds at each position due to the transient response of the thermocouples

3.1.5 Sealing

The rolling diaphragm, discussed in Section 2.4.3 allowed a perfect seal to be achieved with an imperfect piston and piston cylinder. However, proper operation of the rolling diaphragm requires a minimum 2 psi pressure differential across the diaphragm to achieve the proper rolling function of the component. This increase in charge pressure leads to an increase in forced work and the implications of using a diaphragm from the perspective of forced work was only understood midway through this project.

As a result, the ILG was redesigned to allow for the use of a different piston/cylinder system. A graphite piston and glass cylinder set were used as the piston, as shown in Figure 29. This eliminated the need to have a 2 psi pressure differential on either side of the piston, and this allowed the ILG engine to run.

The 90° Gamma engine also had issues with the piston seal during initial construction. The initial piston had no issues maintaining a seal, however, the tolerances were too tight between the piston and cylinder that were manufactured at the university machine shop and as a result, the frictional losses from piston were too great, and the aluminium cylinder eroded. The engine was redesigned, and a similar graphite piston/glass cylinder piston was installed in its place, as shown in Figure 30. The effect that this glass piston had on engine performance is discussed in [21].

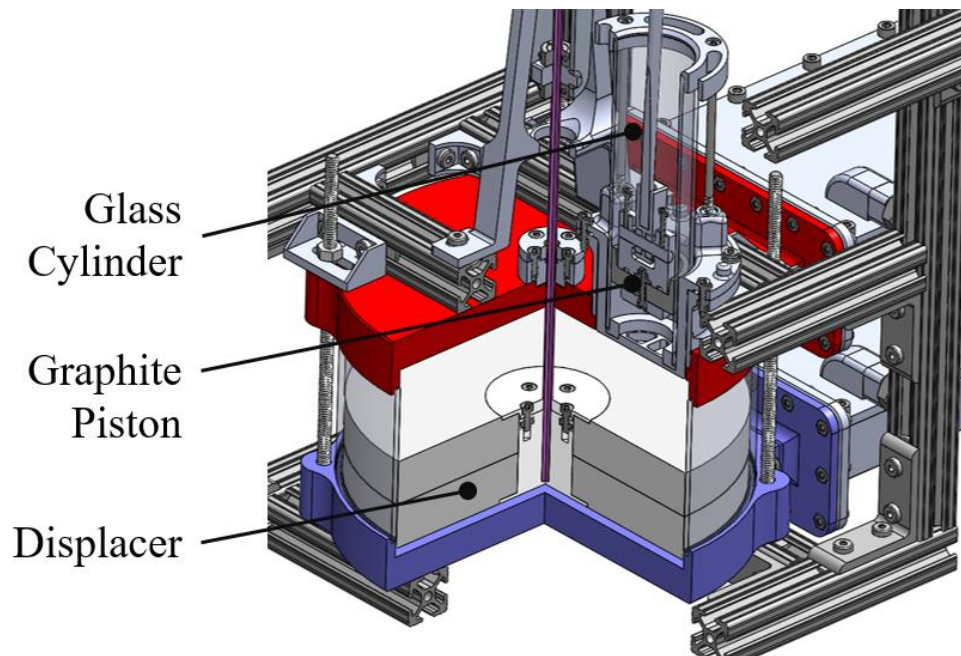


Figure 29: CAD model of the ILG with the glass cylinder and graphite piston assembly

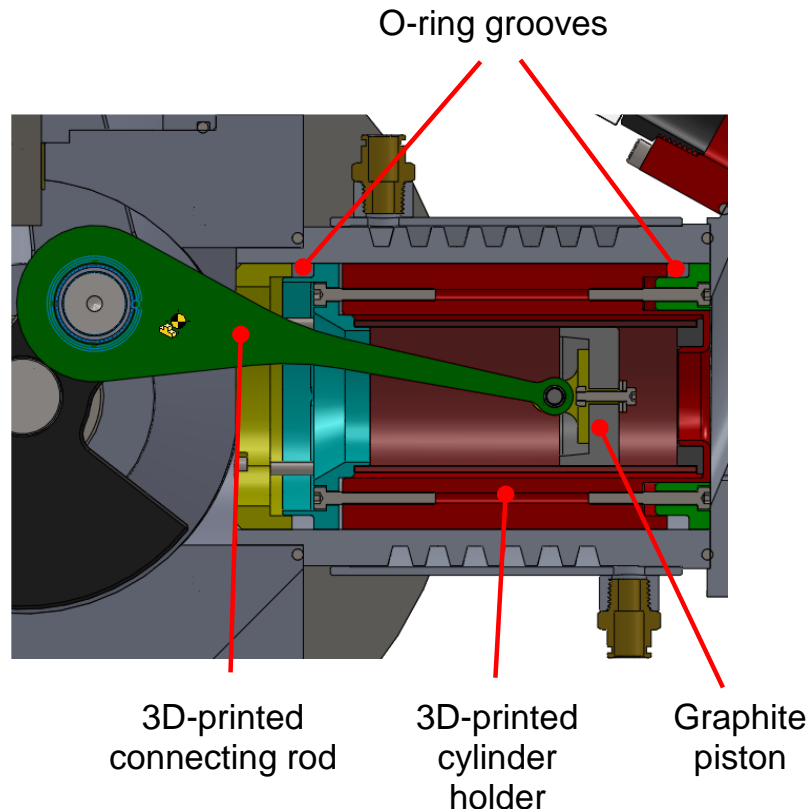


Figure 30: CAD model of the 90° Gamma engine with the glass cylinder and graphite piston assembly

3.1.6 Conclusions from the project limitations

The limitations discussed in this section were a result of some of the assumptions that were made early on in the project. The use of 3D printing did allow the manufacture of prototypes with complex geometries, yet our assumption that the printed parts would function as intended was challenged once physical testing began. Techniques to improve the quality and function of these parts were developed to address each of these issues and a much better understanding of the process was gained as a result.

The significance of forced work in low temperature Stirling engine designs was not understood in the early stages of this project and had drawn attention away from the physical engine built. The developed predictive models now account for the presence of forced work and design processes have been adapted to better control the engine buffer pressure to minimize forced work associated with the pressure differential across the rolling diaphragm.

The heat transfer and reciprocating flows inside of the engines was also a limitation of this work. The fundamental heat transfer research and the UNIT design and prototyping were conducted in parallel and as a result, it was found that the assumptions used to characterize the heat exchangers were invalid for the engine operating conditions. The body of research associated with

understanding these reciprocating flows will be essential to this project and will be heavily emphasized moving forward.

Each of these major limitations has caused engine redesigns and rebuilds. These include the redesign and re-printing of major components to achieve the proper function from the 3D printed parts, the redesign of sealing interfaces on both the engine bodies and heat exchangers, and the redesign due to improper material selection due to excessive heat losses. Each of these rebuilds has resulted in significant learnings regarding UNIT design, but has also unfortunately delayed the collection of experimental data essential to the development of higher order predictive engine models, which are essential to determine qualitative measures of performance from the different engine configurations. As a result, making a detailed recommendation of the most successful UNIT would be based on qualitative measures of manufacturability rather than quantitative measures of performance. The approach that will be used to make the recommendation will be discussed in Section 3.6, however, a recommendation will not be provided.

3.2 Heat exchanger design

3.2.1 *Characterizing heat exchangers in oscillating and pulsatile flow*

The effectiveness of the heat exchange has a significant impact on the performance of Stirling engines. Typical heat exchanger design involves determining the heat transfer characteristics for a particular heat exchanger geometry for the expected flow conditions in the system. This is typically obtained from measuring the heat transfer rate or from Nusselt number vs. Reynolds number relationships [33]. Examples of these types of results are shown in Figure 31 which were collected experimentally for pulsatile flow conditions [24]. The development of these data processing approaches will be applied to all future heat exchanger characterization experiments.

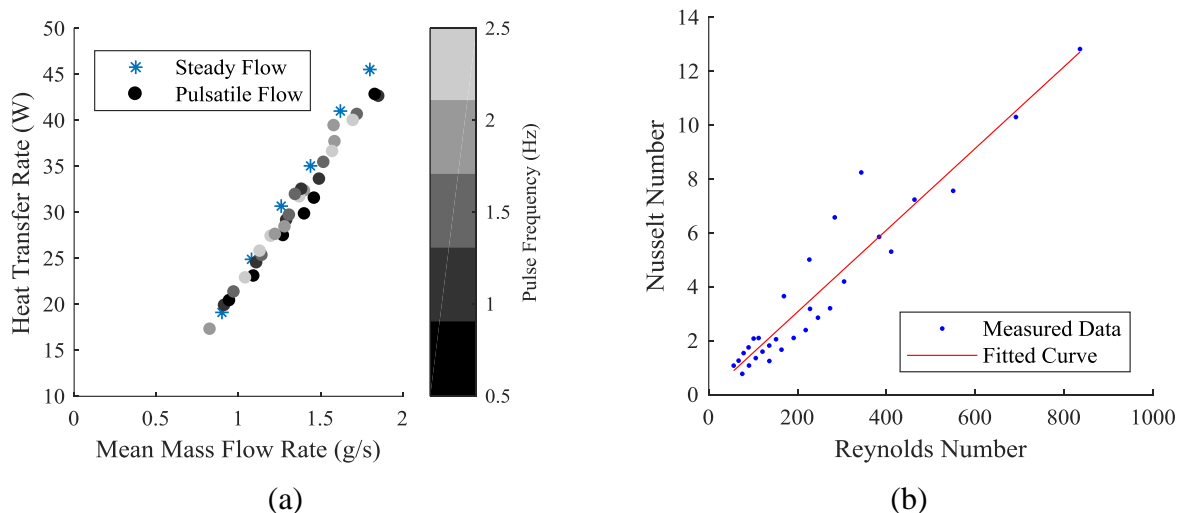


Figure 31: Experimental heat exchanger characterization plots obtained from pulsatile flow conditions [24]

The Stirling engine invokes an oscillatory flow across the heat exchangers [25], [34], [35], and is a relatively unexplored flow regime when compared to bulk, steady flows. In situations where these relationships do not exist, they must be determined experimentally. An experimental setup, like the one shown schematically in Figure 32, as was designed by Michaud *et al* [25] for this purpose. With the use of a piston and electric motor, this experimental setup moves fluid through hot and cold heat exchangers and measures the resulting air temperatures at various locations within the duct with 29 thermocouples. These types of measurements are used to develop Nusselt-Reynolds relationships. This methodology will be used to test and characterize heat exchanger performance in later stages of this project.

These types of experimental investigations often lead to interesting results. The temperature measurement results from Michaud *et al* [25], shown in Figure 33, outline the importance of proper fluid mixing on heat transfer. A difference of up to 10 °C was found between the floor and ceiling of the duct which suggests that buoyancy driven phenomena in the oscillating flow affects the heat transfer performance of the heat exchangers. Buoyancy effects would be undesirable as this would couple engine performance with engine orientation and would limit possible CELL configurations. Determining methods where these buoyancy effects can be minimized and controlled will be important.

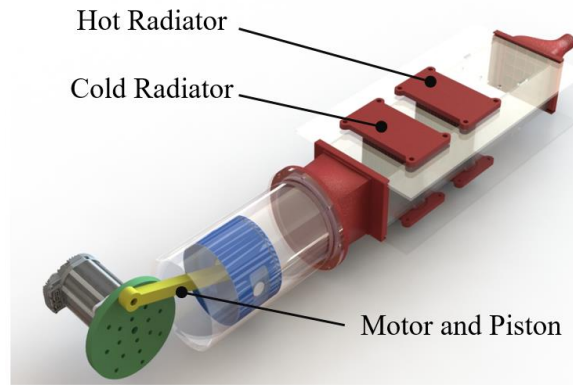
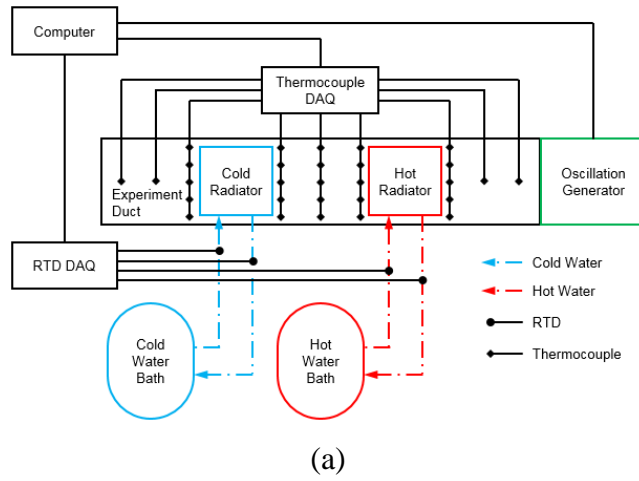


Figure 32: Process and instrumentation diagram (a) and solid model render (b) of an experimental setup for characterizing radiator style heat exchanger performance in oscillating flow

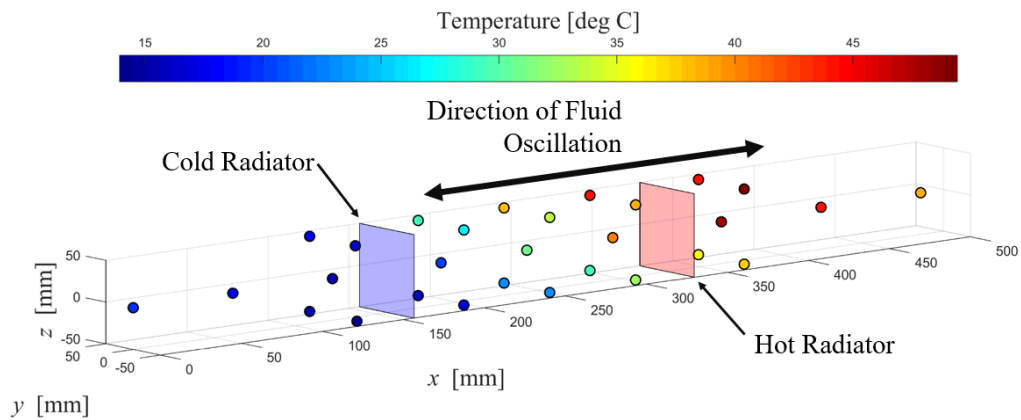


Figure 33: Spatial temperature distribution within the experimental duct

3.3 Determining engine performance

3.3.1 *The indicator diagram*

The indicator diagram plots the pressure of the working fluid as a function of total internal volume. In its simplest form, the indicated work of the cycle is given by the area within this curve minus the forced work [10], which is the difference between the buffer pressure and the engine pressure. This data is experimentally collected using the experimental setup and software described in Section 2.3 and is shown in Figure 34. This experimentally measured indicator diagram shows that there are also buffer pressure fluctuations, increasing the amount of forced work that must be overcome by the engine. This is one of the many losses that will be discussed in an upcoming section.

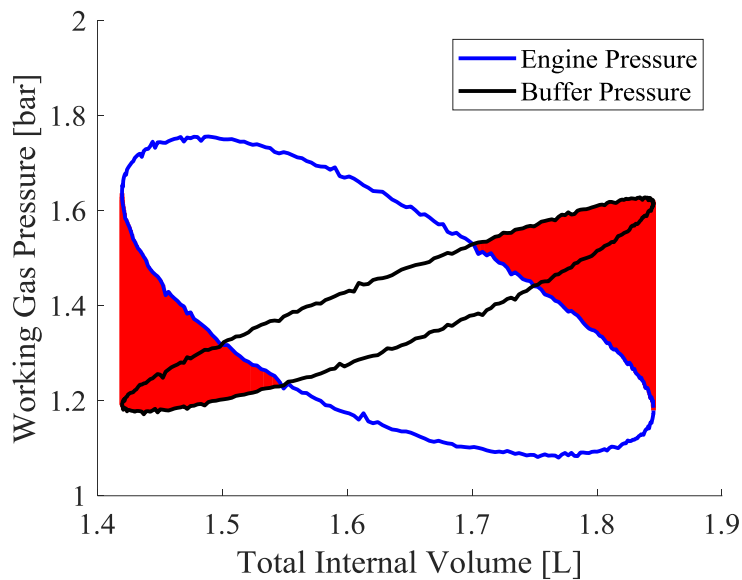


Figure 34: An experimental PV diagram and buffer pressure of the 90° Gamma engine with forced work shown in red

Indicator diagrams can give insight into the level of agreement between measured and predicted performance. Figure 35 shows a pair of experimental indicator diagrams with their accompanying isothermal and adiabatic reference cycles. This experimental data was collected from the 90° Gamma engine; Figure 35 (a) was produced from data collected at a heater temperature of 400 °C, and shows a much closer agreement between experimental results and predictive reference cycles compared to what is shown in Figure 35 (b), which was collected at a heater temperature of 300 °C. These plots show that model agreement at higher engine temperatures is significantly better than at lower temperatures. This reinforces the need to develop a higher order model to better predict engine performance.

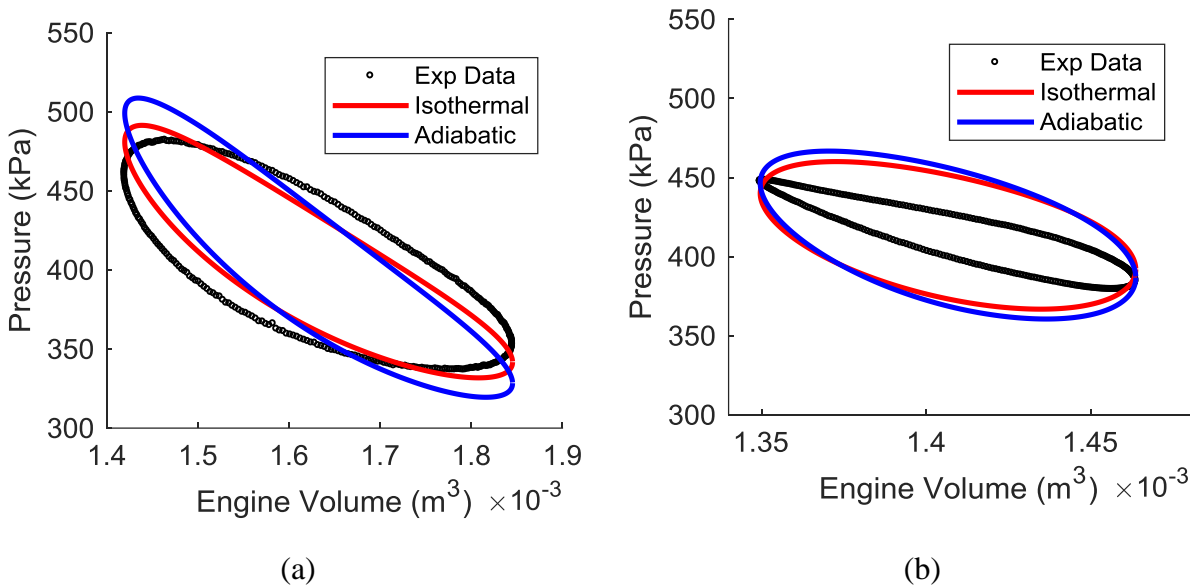


Figure 35: Experimental indicator diagrams with overlaid reference cycle models for the 90° Gamma (a) with a heater temperature of 400 °C, and (b) with a heater temperature of 300 °C with the modified piston

3.3.2 Decoupled Stirling engine losses

An introduction to second order models and decoupled losses was given in Section 2.1.4 and a detailed analysis was performed with experimental data from the 90° Gamma engine described in Section 2.2.1. Generating this data consisted of setting up a myriad of tests, including but not limited to:

- Shaft power as a function of operating speed
- Torque and shaft power as a function of expansion space temperature
- Crank case pressure as a function of expansion space temperature
- Indicated and forced work as a function of expansion space temperature
- Engine speed as a function of expansion space temperature
- Gas spring hysteresis loss as a function of expansion space temperature

Figure 36 shows the results of this second order analysis in terms of normalized power losses as functions of both heater temperature and mean pressure. Figure 36 (a) shows that the mechanical friction and the imperfect heat transfer dominate the decoupled losses, especially at low temperatures. Figure 36 (b) indicates that mechanical friction and imperfect heat transfer still dominate the losses, however, as the mean pressure is increased, the losses due to imperfect heat transfer increase.

Although the quantified values of these decoupled losses are dependent on the specific scale and geometry of the engine for which they have been calculated for, the observed trends provide insight into the underlying physics. For a low temperature Stirling engine, the maximum heater temperature will be limited to the low grade heat sources (<120 °C) which lie within the scope of

this project. In addition to this, operating conditions with an elevated mean pressure will increase the amount of indicated work from the engine. Based on the trends seen in Figure 36, the desired low temperature, pressurized operating point of these engines means that mechanical friction and heat transfer must be held paramount in future design iterations of this project. Mechanical friction can be improved by working with higher tolerance components and best-practice approaches to mechanism design. However, improving the imperfect heat transfer is a question of fundamental fluids mechanics and heat transfer research. Such questions include the passive and active control of reciprocating flows through heat exchangers and complex geometries at a range of engine speeds.

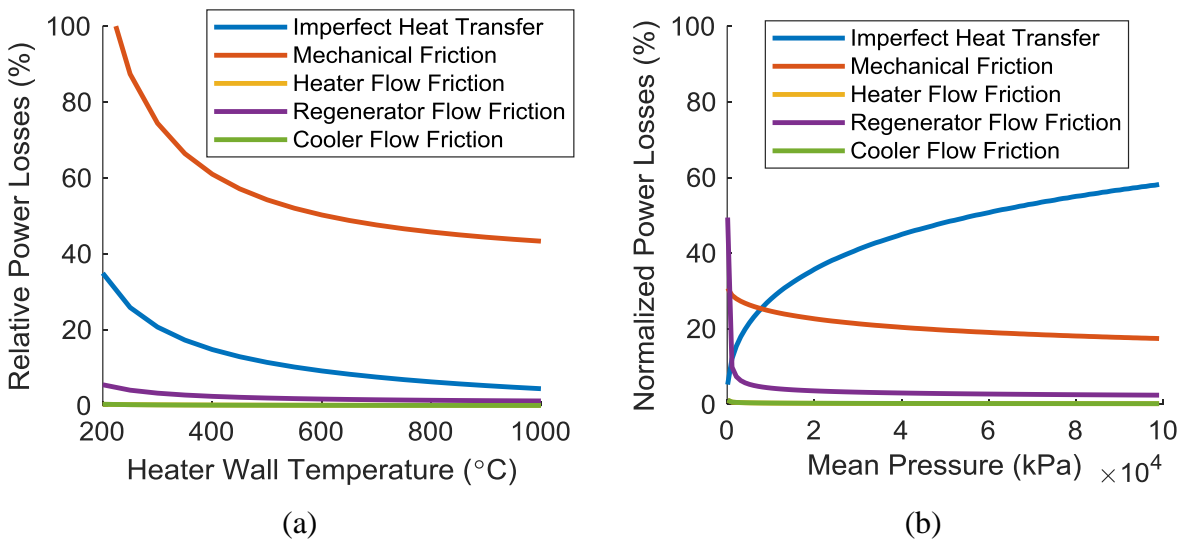


Figure 36: Normalized power losses (a) as a function of heater wall temperature for the 90° Gamma engine, (b) as a function of mean pressure

The importance of the flow/heat transfer phenomenon can be seen when looking at the heat exchanger performance as a function of engine speed, as shown in Figure 37. For both the heater and the cooler, the difference between the heat exchanger and the measured gas temperature increases with mean pressure. This is due to the increasing number of gas molecules to be heated and cooled. The temperature drops also begin to decrease with increasing engine speed. If the same flow pattern was expected across the range of engine speeds, this phenomenon would be unexpected as the heat exchangers would have a shorter amount of time to heat and cool the gas, leading to a larger temperature drop for the higher engine speeds. An explanation for the observed trend is a shift in the flow regime which alters the convective heat transfer coefficient of the flow. The observed improvement in the heat transfer is significant and having the ability to design systems with the desired convective properties and to control the flow regime will be critical to ensuring the imperfect heat transfer losses, shown in Figure 36, can be minimized at lower operating temperatures.

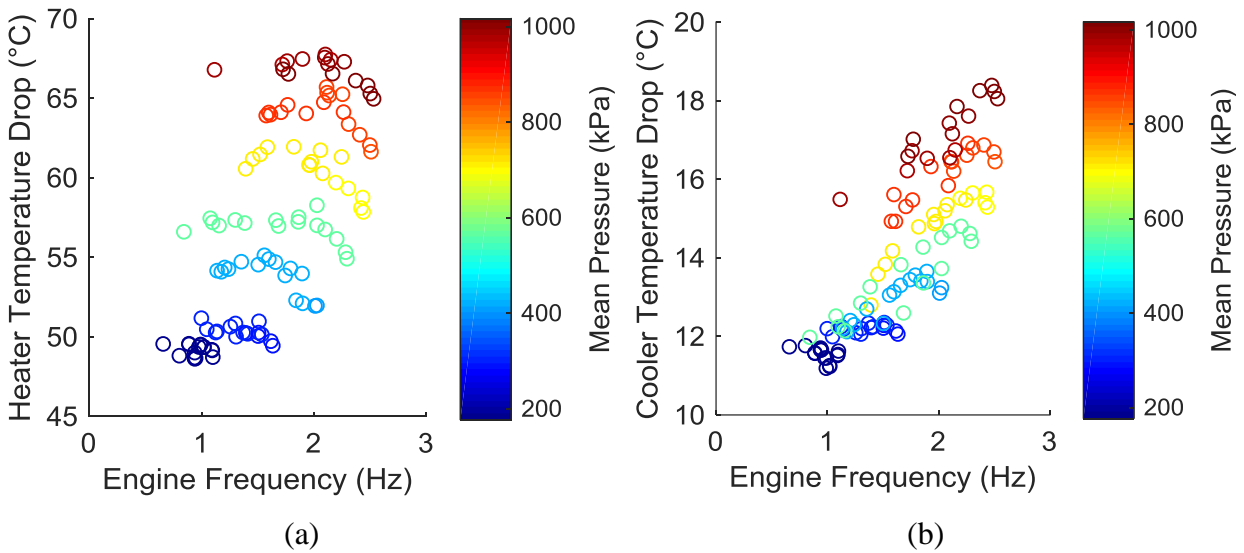


Figure 37: Temperature drops between the (a) heater and (b) cooler set point and the measured gas temperature as a function of mean pressure

3.3.3 Effect of geometry on engine performance

Preferential flow through the engine can negatively affect the expected heat transfer within the engine and evidence of these flows has been found in the 90° Gamma engine. Figure 38 shows temperature measurements on the cold side of the regenerator for a range of engine pressures. The red and blue data points show temperature measurements on opposite sides of the annular regenerator. This plot reveals that the gas on one side of the regenerator is consistently warmer than the other side across the range of pressures. Additionally, as the mean pressure decreases, the effect of this preferential flow becomes more significant. It is expected that early UNIT prototypes will not have a large internal pressure, and the results in Figure 38 shows that the presence of preferential flow must be accounted for at these operating points.

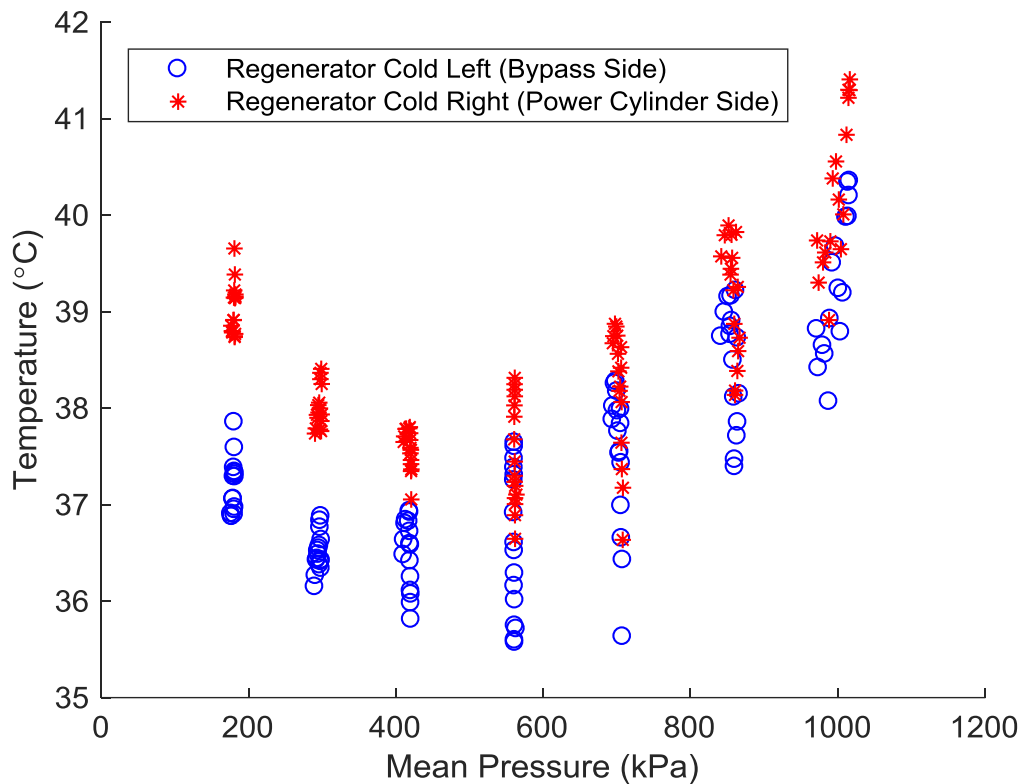


Figure 38: Measured gas temperatures at the interface between the regenerator and the cooler with the engine running at a heating cap temperature of 200 °C

By rotating the 90° Gamma engine with an electric motor, the pressure drop across the heater was also found not to be constant at different azimuthal locations around the displacer. Figure 39 shows a polar plot of the pressure drop magnitude across the heater at eight (8) circumferential locations around the displacer axis. These results show that the pressure drop approximately triples on the power piston side of the engine. This pressure drop suggests a higher gas flow rate through the regenerator on this side, and would alter the local heat exchanger performance and flow regime.

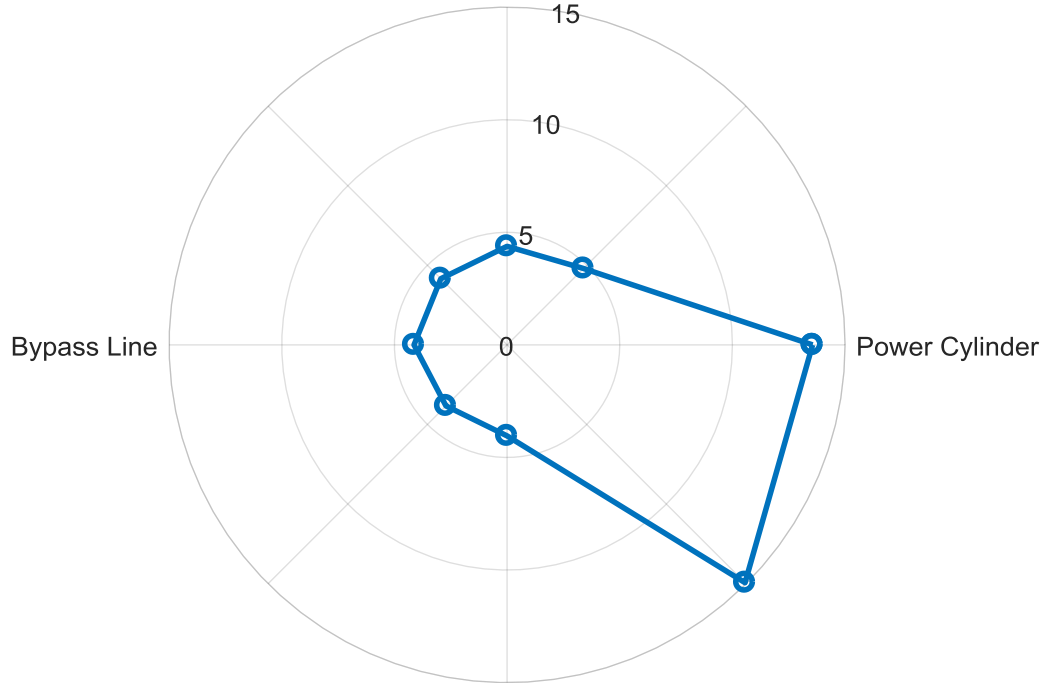


Figure 39: Polar plot of measured heater pressure drop magnitude [kPa] as a function of azimuthal heater cap position

3.4 Literature review of the thermo-fluids of a Stirling engine

As discussed in the previous section, mechanical losses occur in Stirling engines due to friction in bearings, valve gear and piston rings. Once these losses have been minimized [16], [36]–[39], the effects of heat transfer are likely to remain a major factor limiting Stirling engine efficiency. Some heat exchange losses can be dramatically reduced. For example, one can consider quasi-adiabatic processes using a well thermally insulated device. However, the heat exchange to and from the cylinder and heat exchangers walls is inherently irreversible. While investigating the thermo-fluids of the Stirling engine cycle for different engine configurations was not an original aim of this project, it is important to understand this in terms of engine design and potential engine performance. Greater appreciation for the problem can be resolved by reviewing the literature in this area and discussing in relation to this project with consideration of what type of research activities could be undertaken to further understanding of the problem.

3.4.1 Reciprocating flows and heat transfer correlations in Stirling engines

Reciprocating flow is a characteristic feature of Stirling engines, whose heat transfer characteristics are quite different from those of steady flows. Many analytical and semi-empirical models are proposed in the literature with the aim to develop approximations of convective heat transfer coefficients in Stirling engines. These models consist of laminar and turbulent steady unidirectional correlations. In the fully turbulent and fully laminar range the steady unidirectional approximations are fairly good [40]. However, these unidirectional steady correlations are not suitable for reciprocating flow heat transfer in Stirling engine since many modern Stirling engines operate in or near the laminar to turbulent transition region [34]. Previous investigations have shown [41]–[43] conflicting results and different values of the critical Reynolds number for the laminar to turbulent flow transition. The number of studies conducted on laminar to turbulent transition in time-dependent frames are small due to the difficulty to conduct reproducible and accurate time-dependent experimental conditions. This is particularly challenging in terms of a simultaneous analysis of the time-resolved temperature and velocity fields. Previous research has been conducted to measure the overall heat transfer coefficients in heat exchangers subjected to reciprocating flow for different specific applications [44]–[48] and did not consider the role of microscopic fluid flow on heat transfer behavior. Very few experimental research studies ([49]–[51]) have focused on the time-resolved temperature fields in reciprocating conditions for some particular applications. None of which attempted to combine the temperature and velocity field (or fluid displacement) information.

3.4.2 Similarly parameters of a reciprocating flow

Similarity parameters are required to concisely and generally describe the fluid mechanics and heat transfer in physically similar systems. Their proper choice is crucial for the development of an experimental setup and the interpretation of experimental data. The similarity parameters of a reciprocating flow can be derived by normalizing the Navier-Stokes momentum and energy equations [34]. The fluid dynamics similarity parameters are the kinematic Reynolds number ($Re_\omega = \omega d^2 / (4\nu)$) which is the coefficient of the temporal acceleration term, the maximum Reynolds number (Re_{max}) which is the coefficient of the spatial acceleration and the pressure gradient term. Re_δ is often used to characterize the laminar to turbulent flow transition in reciprocating boundary layer flow. It accounts for the oscillating frequency and the peak velocity and is described by $Re_\delta = \frac{\delta U_{max}}{\nu}$ with $\delta = C(2\nu/\omega)^{1/2}$ being the Stokes layer thickness

3.4.3 Experimental studies in reciprocating flows

Fishler and Brodkey [52] characterized the transitional and turbulent oscillatory flow in a rigid pipe using flow visualization to establish the existence of coherent structures. It was found that these coherent structures were a series of deterministic events which occurred randomly in space. However, the structures exhibited time dependence, occurring only during decelerated flow. Five events: local deceleration, local acceleration, excitation-transverse vortex, ejection, and sweep (possibly a relaminarization) were postulated from these findings. The range of values of the

critical Reynolds number based on peak velocity and Stokes (boundary) layer thickness was calculated using the existence of flow structures as the criterion of turbulence.

The qualitative description proposed by Fishler and Brodkey [52] of the coherent structures for different flow regimes lacks an objective criterion for coherent structures detection in the oscillating flow. The visual description of the flow would be a starting point for further physical understanding of the vortex formation and their development in the transitional and turbulent boundary layers encountered in Stirling engine reciprocating flows.

Hino et al. [41] conducted an experimental investigation on the transition to turbulence in a purely oscillatory pipe flow using single hot-wire measurements. The authors found three types of turbulent flow regime: weakly turbulent flow, conditionally turbulent flow and fully turbulent flow. The demarcation of these flow regimes were based on the measured velocity fluctuations. Discrepancies between the critical Reynolds numbers for the turbulent onset were attributable partly to different transition criteria employed. In previous experiments, the instability limit was determined by visual observation of tracer dye, while in Hino *et al* [41], direct measurements of velocity variation were carried out.

The flow analysis presented by Hino et al [41] lacks a statistical analysis of different flow events throughout an oscillating cycle. Also, understanding the behavior of coherent motions requires obtaining spatially correlated data: i.e. simultaneous measurements of the velocity field at several points in space. To this end, time-resolved Particle Image Velocimetry (PIV) could be implemented in context of this proposal. Data of this type would also provide detailed validation of the CFD predictions for the mean field for the wall flow and the flow mixing.

Since the heat transfer enhancement in reciprocating flow is mainly due to the interactions between the thermal and viscous boundary layers, it would be of interest to explore such interactions for a compressible medium (e.g. gas) in order to mimic the operating conditions encountered in Stirling engines. Experiments could be conducted to characterize the flow regimes of different parts of an oscillating cycle over the desired operating conditions. Time-resolved experimental investigation can be used to analyze the flow dynamics inside different chambers of a Stirling engine. Temperature and velocity fields will be simultaneously quantified using high-speed volumetric PIV and PLIF measurements. The focus would be on the processes occurring within the thermal and viscous boundary layers in terms of vortex dynamics and its effect on the temperature distribution. The measured phase-dependent temperature fields combined with the velocity fields will be developed to properly describe the interactions between the velocity and temperature fields.

In addition to characterizing the coherent motion for different flow regimes, unsteady pressure sensors will be used to capture surface properties that are sensitive to the state of the flow above the surface. Since the unsteady surface pressure field can capture the variation in the flow unsteadiness, the pressure measurements on the Stirling engine walls can be used for flow state estimation and development of an optimal control strategy. Therefore, the chamber walls will be equipped with high frequency response subminiature pressure transducers. Unlike the time averaged flow analysis, these pressure measurements provide temporal information of the specific flow patterns.

3.4.4 Enhance mixing inside Stirling engine chambers

The flow inside the cylinder of a reciprocating engine is characterized by the presence of large recirculation zones for different phases of the Stirling cycle [53]–[55]. Salazar et al. [55] conducted a CFD investigation on the flow inside the piston of a simplified Beta-type Stirling engine geometry. These authors found that the flow impingement is the major heat transfer mechanism in the expansion and compression chamber, and the temperature distribution is highly non-uniform across the engine at any given moment. Their results showed that the variations of heat transfer rates are much more complicated than the constant heat transfer coefficient used by the second-order models of Stirling engines found in the literature.

In order to improve the fluid mixing inside the cylinder and displacer chambers, a different chamber geometry can be proposed. Nam et al. [56] studied the in-cylinder flow for internal combustion (IC) engine with different bowl shapes (A, V and H-shape) using LES models applied to a piston-cylinder assembly with a stationary valve and a harmonically moving piston. The authors found that the A-type piston exhibits the maximum tangential velocity in the compressing phase and that both turbulence intensity and radial velocity were the highest for the A-type piston at near TDC because of the squish area in the three piston bowl shapes. Different cylinder geometries can be investigated in the present study in order to quantify the influence of the cylinder shape on fluid mixing and heat transfer.

These two works highlight that a deeper understanding of the flow dynamics and heat transfer inside different chambers of a Stirling engine is needed. As both the type of flow and the effect of chamber and piston geometry is important, detailed measurements are needed. Simultaneous time-resolved velocimetry and temperature measurements (PIV & PLIF) would provide important information on the heat transfer and flow. A more appropriate semi-empirical model to predict the heat transfer inside Stirling engines could then be developed using a parametric study that accounts for the non-constant heat transfer coefficients and the effect of geometry.

3.4.5 Enhance heat transfer using vortex generators

Vortex generators (VGs), and wall extensions that are either submerged or protrude the boundary layer, have been long researched as potential devices for passive control of heat transfer. These are proposed as passive devices to enhance the heat transfer from the Stirling engine heat exchanger walls. VGs are essentially bluff bodies around which hairpin vortices and horseshoe vortices form. Vorticity shed from the hairpin structures entrain high-speed fluid towards the wall, while horseshoe vortices form a stream wise pair of intense near-wall counter-rotating vortices enhancing the mixing of high and low-momentum fluid in the wall layer. Vortex-induced heat transfer enhancement is based on the deliberate generation of large-scale longitudinal vortices in the flow using vortex generators. Local heat transfer enhancements can be achieved and are explained by enhanced thermal mixing. The local thinning of the thermal boundary layer associated with the secondary flow is responsible for the heat transfer enhancement. A particular care should be taken when designing the vortex generator since areas of reduced heat transfer can be caused through the diminished impact of recirculation eddies behind the vortex generator.

Edwards and Alker [57] studied the effects of size and spacing of the cubes and vortex generators on the heat transfer experimentally in a fully developed duct flow. They found that cubes provided a greater enhancement than delta winglet vortex generators, with a maximum local Nusselt number enhancement of ~76%. Counter-rotating vortices were found to perform better than co-rotating vortices. However, no pressure drop data was provided from this study. Turk and Junkhan [58] obtained a local spanwise-average heat transfer enhancement up to 200% using rectangular wing vortex generators of various heights and angles of attack placed near the leading edge of a heated flat plate.

Fiebig et al. [59] studied vortex generators in the form of one delta wing and one delta winglet pair in a rectangular channel with Reynolds numbers between 1360 and 2270. Using the unsteady liquid crystal thermography method, they also reported local enhancements of up to 200%. The same authors [60] studied the vortex structure, drag, and heat transfer of plate fins with different wing-type VGs placed on fins in developing laminar channel flow using flow visualization, scale measurements and unsteady liquid crystal thermography. They found that the additional drag induced by the VG is independent of Reynolds number and VG geometry but proportional to dynamic pressure and VG area and increases with angle of attack. It was also found that Delta wings are most effective per unit VG area for heat transfer enhancement, closely followed by delta winglets and delta winglet pairs. Rectangular wings and rectangular winglets are much less effective. The heat transfer increases by up to 50%, and the pressure drop increases by approximately 45%. The VGs generate two longitudinal vortices (LVs) which induce cross-flow (azimuthal) velocities that lead to a stagnation line of the cross-flow velocity. The LVs don't break down, they dissipate very slowly, and their effect on heat transfer enhancement persists very far downstream from the VG. It was also interesting to note that the heat transfer ratio of a fin with and without VG is independent of Reynolds number in the investigated range and increases with angle of attack up to 60°.

Vortex generators are defined as those with a device height between 10% and 50% of the boundary-layer thickness. It was shown [61] that submerged VGs with heights below 60% of the boundary layer thickness have the potential to exceed the performance of conventional VGs protruding the boundary layer because of the much lower device drag. In addition, the low-profile VGs are submerged in the boundary layer and thus disturb the outer flow less than the conventional VGs. Vortex generators are also be used to increase mixing since they act on controlling the dissipation rate of turbulence, which is directly related to the mixing length scale [61]. When properly located, the low-profile VGs can significantly enhance the heat transfer, as the boundary layer is thinner and contains lower mixing losses.

Based on the literature review on passive vortex-induced heat transfer enhancement, the Delta wing and winglet offer heat transfer and pressure drop performance superior to that of the rectangular geometry, but the rectangular winglet is competitive in some cases. The use of delta winglets downstream of a tube or with flat-tube heat exchangers under laminar flow conditions is the most successful arrangement examined for application.

Due to the flow complexity through heat exchanger passages of Stirling engines, and the presence of many important length scales and geometric features, further research is needed to provide

definite indications of how and when vortex-induced heat transfer enhancement should be pursued in these complex channels. Deeper understanding of the flow and heat transfer interactions could identify the desirable features of vortex flows for heat exchanger geometries and point toward schemes for exploiting their full potential. Since VGs protrude into the flow, they do increase drag locally, but if designed correctly, the pressure drop penalty can be reduced.

3.4.6 Numerical investigations of Stirling engine reciprocating flow

Many attempts at developing numerical models for the Stirling engine cycle for a particular engine geometry have been made in the past few decades. Resolving the complicated heat and mass transfer processes with multi-dimensional components of a Stirling engine cycle is crucial to the prediction of the overall engine performance. The steady zero- or one-dimensional models (based on the mathematical terms in the governing equations) used by many authors cannot resolve in great detail or very accurately the complicated physical processes and the effects of some geometrical features on the Stirling engine performance. Therefore, more sophisticated 4th order models based on CFD should be used to improve the accuracy of the numerical analysis on Stirling engines. However, there exist many challenges to apply a CFD analysis on a Stirling engine cycle as the cycle is unsteady and multi-scale in nature.

In addition to the unsteady nature of the cycle, the computational domain is constantly changing in time because of the moving parts (power piston and displacer) of the engine. Advanced moving mesh techniques applied to a compressible gas flow that can be laminar, transitional and turbulent through one reciprocating cycle should thus be used. In order to resolve the complicated heat and mass transfer in different Stirling engine chambers simultaneously, it is necessary to use very fine grids and small time steps to solve many coupled governing equations at the same time. Therefore, there have been few studies on using CFD approach to study the full Stirling engine cycle. Mahkamov [62] used both a 2nd-order model and an axisymmetric CFD approach to analyze the working process of a Stirling engine. This work found significant differences between the two methods for predicting both the temperature distribution and engine performance. The CFD model provided a much more accurate output power and a transient temperature variations far from the harmonic distributions given by the second-order approach. The same author [63] studied the influence of some geometrical key factors to improve the engine performance. Such detailed analysis on the effects imposed by multi-dimensional geometrical features can only be resolved by a CFD approach.

Chen et al [54] developed a three dimensional, compressible CFD code to study the flow dynamics and heat transfer inside a Gamma-type Stirling engine. The flow and heat transfer phenomena of the engine cycle were solved by transient three-dimensional laminar and compressible Navier-Stokes equations plus the energy equation and the ideal gas equation of state. Some other assumptions to facilitate CFD simulation were made as follows: fluid viscosity and thermal properties of all materials are assumed constant, the working gas was air and assumed to be an ideal gas and the effects from mechanical friction and thermal radiation were ignored. The authors presented temperature contours, velocity vectors, and distributions of local heat flux at several important stages in an engine cycle as well as average temperature variations, integrated rates of heat input, heat output, and engine power.

A numerical model based on a RANS method with Saffman's turbulence model [64] has also been employed to solve the time-dependent turbulent Navier-Stokes and energy equations for oscillating flows. Hsu et al. [65] demonstrated that Saffman's turbulence model is applicable for unsteady oscillating flows and they also provided a complete account for the oscillatory shear stress on a flat plate. Yan et al. [66] conducted a numerical investigation using the Saffman's turbulence model to provide in-depth description of oscillating pipe flows and the averaged Nusselt numbers on the tube wall over wide ranges of Reynolds numbers. The authors validated their numerical results by comparing the laminar flow results to analytic solutions and turbulence flow results to published experimental data.

3.4.7 Conclusion

This brief review highlights that fully reciprocating flows have many unique features and have not been well investigated in the context of the proposed work. There are many unknowns on the basic flow phenomenon as well as understanding of how these flows can be physically scaled, what features are important for flow and heat transfer and what are the best approaches for modelling. The review also highlights that while there is significant difficulty in undertaking numerical modelling of a Stirling engine, there are many potential insights and benefits from this approach. Importantly, with a suitable model, design iterations can reasonably be undertaken to investigate different physical geometries of Stirling engines which can also provide important insight for changing scale or physical size of the engine. The review of the literature has also highlighted that experimental validation is critical for the validation of a CFD model. The ability to experimentally measure velocity and pressure over a large spatial domain with high temporal resolution will provide important insights into the workings of the Stirling engine. In addition, these experiments will also be used to develop, and to understand the limitations of numerical modeling approaches.

3.5 Determining the effect of engine scale on engine performance

3.5.1 Configuration comparison

Understanding the effect of unit scale on the power output of each of the engine configurations is essential for determining the most promising UNIT. This process requires determining an evaluation length scale which can be used to compare the configurations against one another for a range of physical scales. The ability to relate this length scale to the engine parameters which influence thermodynamic models is the most fundamentally correct approach, as this length scale will directly relate to the power output of the UNIT.

The lack of decoupled loss models for the different configurations means that the four different configurations would be represented by the same ideal reference cycle. The decoupled loss models allow geometric and performance based factors on the engine and heat exchangers to be quantified, which are then subtracted from the ideal reference cycle. Thus, if each engine is given an identical swept volume and the configuration specific losses cannot be accounted for, each configuration will produce an identical output power prediction. There are different characteristic length scales which relate to various design parameters of each configuration which allow comparative predictive shaft work curves to be generated and these will be discussed in the following section.

The engine output prediction was done in terms of shaft work per shaft revolution instead of power. Total produced power is a function of the rotational speed of the engine. Currently, there are no models that predict expected engine speed and the losses include in this type of model is likely to be a function of rotational speed. This makes modelling power unreliable at this point. The approach taken was to isolate the prediction from an assumed operating speed. The Beale and West correlations were used to provide the estimates for shaft work in this analysis, meaning that there is no inclusion of losses in the prediction.

The Beale, Eqn 6 and West, Eqn 7, numbers were originally developed by using empirical data from high temperature Stirling engines. The experimentally measured output power was related to the mean pressure, operating frequency and the swept volume [10]. The West number has been referred to as the temperature corrected Beale number, and consists of an additional temperature term. The shaft work predicted from the West number can be expected to be smaller than the values predicted by the Beale number, due to the inclusion of this temperature correction factor. This factor has a much more significant effect on engines with a lower operating temperature, resulting in the large difference in shaft power and has shown to improve the West number correlation for lower operating temperatures [10].

Eqn 6	$B_n = \frac{W_o}{PVf}$	T_C : abs temperature of the cooler T_H : abs temperature of the heater W_o : power output of the engine W_n : West number V : swept volume f : engine cycle frequency P : average gas pressure
Eqn 7	$W_n = \frac{W_o}{PVf} \frac{T_H + T_C}{T_H - T_C}$	

3.5.2 *The use of swept volume to derive an evaluation length scale*

Engine volume relates both to the size of the piston and the amount of fluid in the system. Hence, one approach is to compare configurations based on the cube root of the piston swept volume. The results of such an analysis is shown in Figure 40. This figure shows the effect of the cube root of the swept volume on the predicted Beale shaft work and that all engine designs fall on the same curve. Each of the Stirling engine configurations that have been built lie on different locations of this curve, with the Gamma and Alpha configurations grouped together. However, the use of this length scale has a major shortcoming in that configurations cannot be compared against one another. Without a fully developed decoupled loss model, our reference for predicted power, shown by the red dashed line in Figure 40, will be identical for each engine configuration as each engine will share identical reference cycles.

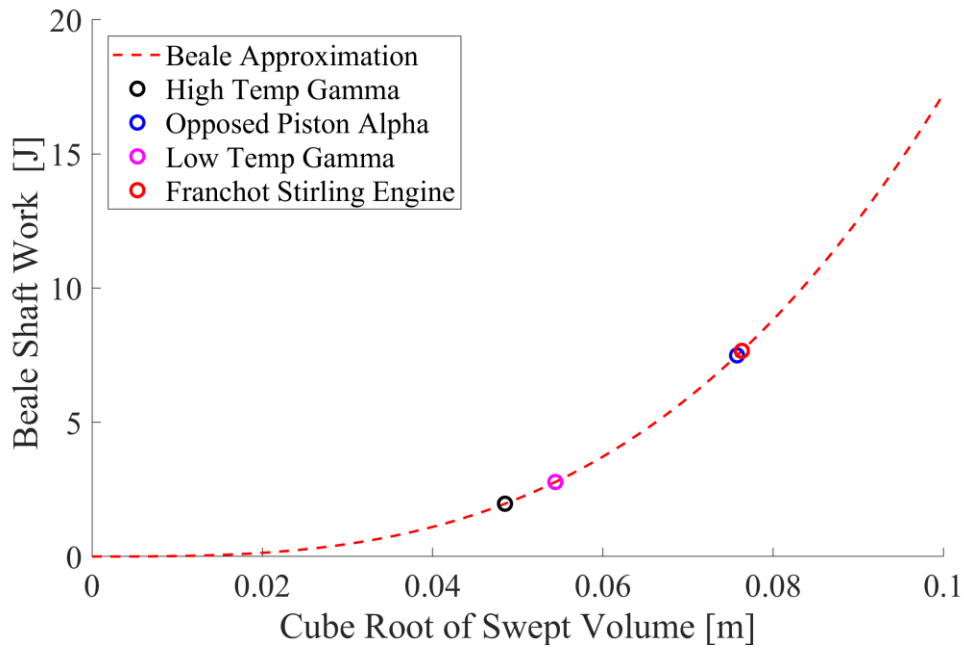


Figure 40: A predictive plot of Shaft work obtained using the Beale correlation versus the cube root of the swept volume length scale

3.5.3 The use of overall engine size to derive an evaluation length scale

In order to obtain a comparative prediction using the Beale and West correlations, a different approach must be taken to develop an evaluation length scale. Instead of using length scales related to thermodynamic parameters, the overall scale of the UNIT can be used. An example of this process is shown in Figure 41 for the in-line Gamma. This control volume approach considers the power density of the volume that the entire unit will occupy. It neglects the flywheel and any associated piping. Results for this analysis are given for both the Beale and West correlations in Figure 42 and Figure 43 respectively, which includes the current build sizes.

The use of this length scale allows different power prediction curves to be generated for each engine configuration by keeping the ratio between the swept volume and the control volume constant for each configuration. This method provides insight into the relative power density of each design. The Franchot UNIT is shown as the most power dense design as it is the only double acting design. The downside of this evaluation approach is that it hinges strongly on superficial design decisions that were made early in the UNIT conceptualization process. For example, the control volume surrounding the ILG engine shown in Figure 41 is strongly influenced by the distance between the displacer cylinder and the crank position. Early in the UNIT design process, minimizing this distance was not a design objective, thus by relying on these design decisions to make a decision regarding the most promising configuration would not be an appropriate design decision.

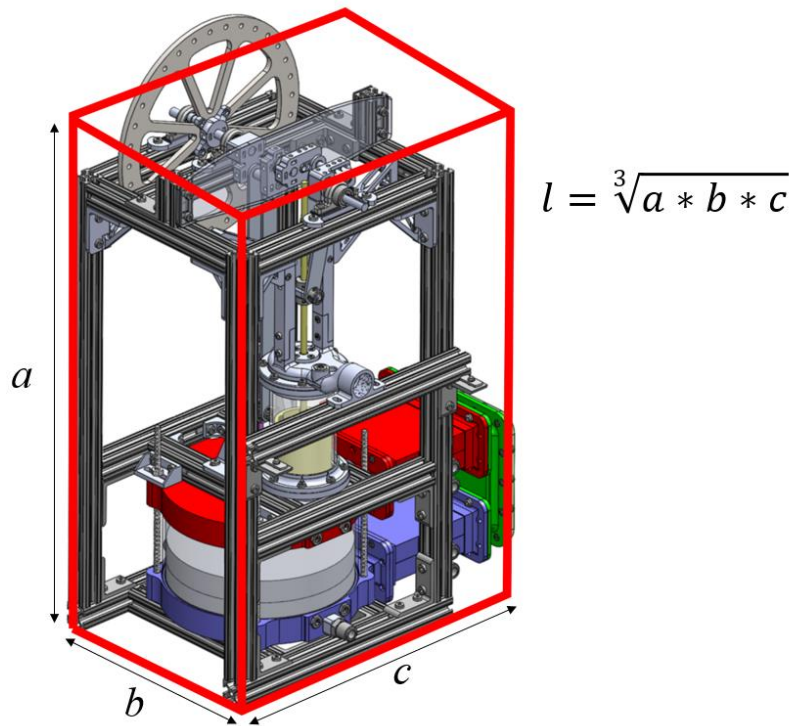


Figure 41: CAD model of the inline Gamma engine annotated to show the control volume which can be used to determine the evaluation length scale related to the physical scale of the UNIT

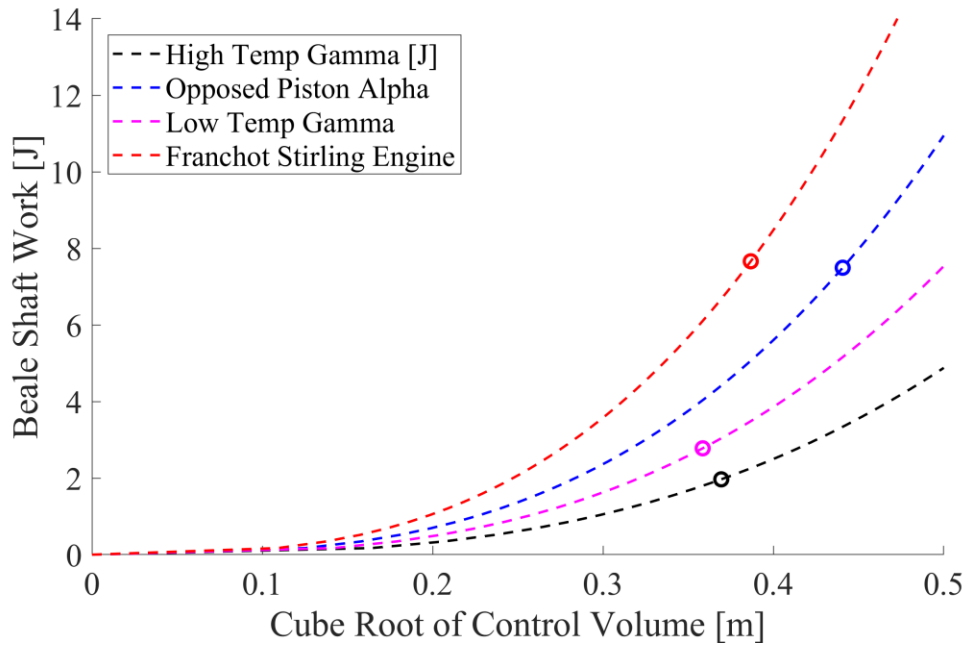


Figure 42: A comparative plot of shaft work obtained using the Beale correlation for a range of control volume length scale values for each of the UNIT configurations

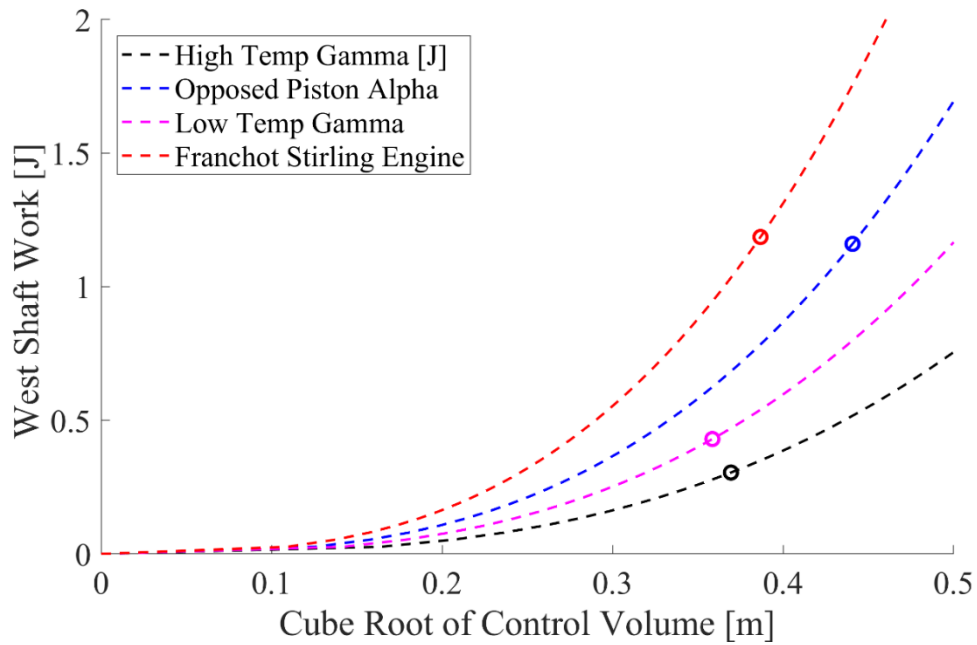


Figure 43: A comparative plot of shaft work obtained using the West correlation for a range of control volume length scale values for each of the UNIT configurations

3.5.4 The use of displacer diameter to derive an evaluation length scale

A second appropriate length scale that could be used is based on the displacer piston diameter. This is the larger diameter of the two pistons in any of the Stirling engine configurations. Results of this analysis are shown in Figure 44 for the different engine configurations and the size of the current engine builds. This allows some comparison of the engine is based on their geometry and the change in piston sizes between the power and displacer pistons for each configuration. Noteworthy is that the OPA will generate a higher shaft work compared to all other configurations especially the Low Temp ILG. This analysis also shows that the Franchot will also underperform compared to the OPA.

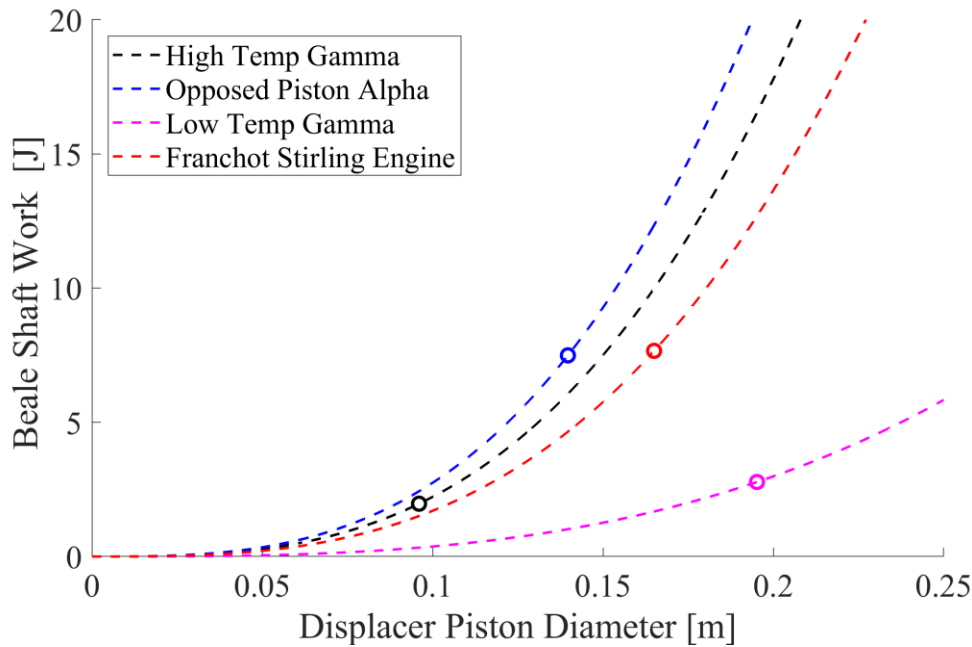


Figure 44: A comparative plot of shaft work obtained using the Beale correlation for a range of displacer piston diameters for each of the UNIT configurations

3.5.5 Configuration comparison conclusions

A comparison based upon predictive models is possible at this stage of the project. However, to determine the effect of physical scale of each of these configurations, a characteristic length scale must be developed. These comparisons are made by determining the expected power as a function of this characteristic length. However, at this stage of the project, the selection of this characteristic length scale affects the outcomes due to the limitations of the developed decoupled loss models.

When using a characteristic length related to the swept volume of the power piston, the UNIT configurations cannot be compared against one another. By relating this characteristic length to the thermodynamic parameters of the model, the lack of decoupled losses means that each configuration is compared to an identical reference cycle. The configurations can be compared against one-another by using a characteristic length related to the displacer diameter, or overall size of the engine. This process is done by keeping critical ratios constant while iterating over the range of length scales. The downside of this approach is that it is dependent on potentially unoptimized design decisions, which may have been made early in the design process.

A final important conclusion here is that any of these analysis approaches need to be modified to include losses. For a particular configuration will typically be fixed and will be related strongly to the mechanical mechanism and the imperfect heat transfer defined by the geometry of the Stirling engine. These need to be individually developed for a particular configuration before any realistic evaluation of different UNIT configuration can be fully undertaken.

3.6 Evaluation

Limitations in the current UNIT design process has prevented the qualitative evaluation process required to properly recommend the most successful engine configuration. However, the process for which the configurations will be compared against one another has been developed and will be discussed in this section. Four categories will be considered when performing the evaluation: engine performance, design scaling, manufacturing, and economic feasibility. A discussion of each of the categories is below, with a sample decision matrix shown in Table 4.

Engine performance

Engine performance primarily considers power output for a specified temperature difference at not only the prototyping UNIT scale, but also when modelling the unit at a larger scale. Additionally, the engine losses unique to the engine geometries are considered, such as the style of mechanism used to couple the power and displacer pistons.

Determining the engine performance will require complete decoupled loss models to be developed for each engine configuration. The methodology for developing these models has been developed from the work done on the 90° Gamma engine. The quantification of engine performance can be performed as soon as a sufficient amount of experimental data has been acquired.

UNIT scaling

UNIT scaling evaluates the influence of the engine geometry on the relative ability to scale up the UNIT design, as well as the possibility to mechanically couple units into multi-unit cells and complete engines.

Evaluating the effect of UNIT scale will be closely related to the development of the decoupled loss models. Quantifying the geometry specific losses across a range of operating conditions will allow performance to be estimated for a varying piston diameter or piston swept volume, thus allowing the performance trends related to engine scale to be determined. By determining the losses associated with the mechanism, losses associated with the use of rigid cranks and belts will provide insight into the most promising UNIT coupling approach.

Manufacturing

The ability to mass produce the finalized unit is important in the final decision. For the compared engine geometries, will scaling the design make alignment more difficult, will the now-printed parts be suitable for conversion to injection molded alternatives and are custom build assemblies required for coupling the units are all questions that are addressed in this category.

Economic feasibility

Minimizing unique parts and producing a design which can easily be serviced will play essential roles in determining the most economic solution. Additionally, using standard structural or piping components for the majority of the major engine components will significantly reduce the cost of each unit.

Table 4 The assessment matrix for evaluating different Stirling engine configurations

Criteria	Description	How to measure this?	Assessment indicator	90deg Gamma	In-Line Gamma	OPA	Franchot DAA
Sealing							
Ability to scale units	Can the unit geometry be scaled? Or are there geometry limitations that hold this back (larger moving	Result of 2nd order model					
How does power scale with size	As the units become larger, is the output power linear? Or exponential?	Result of 2nd order model					
Required level of precision for larger scale designs	As the units become larger, do the alignment tolerances for the design become more strict?	Tolerance analysis of current setups					
Required heating fluid flow rate for large scale engine	Is the required flow rate of heating fluid sensible for a geothermal application	Conversion efficiency					
Other parameters to be added		TBD					
Manufacturing							
Ability to mechanically couple units	The number of units that can be easily coupled in to a cell of the same volume	Result of scaled solid model; available design space; assembly					
Ability to mechanically couple cells	The configuration of a number of cells into an engine of the same volume	Alignment; Assembly; Tolerance range					
Ability to improve performance with system additions	Does the geometry allow/require: sealed crank cases, (eg. springs/pressure vessel)	Assessment of the complexity of the design					
Ability to retrofit/modify portions or units/cells	Component design to accommodate different operating conditions/environments?	Assessment of the design space					
Other parameters to be added		TBD					
Power/Losses							
Power density as a function of length scale	The overall power that can be extracted from the same volume of engine	2nd order model in the same design space					
Mechanical losses/mechanism effectiveness [unit]	Losses due to mechanism effectiveness from piston coupling in unit	Assessment of drive mechanism & 2nd order model					
Mechanical losses/mechanism effectiveness [engine]	Losses due to mechanism used to couple units/cells to one another	Assessment of drive mechanism & 2nd order model					
Minimum hot side temperature	The units ability to run at lower than expected design hot side temperature	2nd order model and heat exchanger efficiencies					
Other parameters to be added		TBD					
Economic Feasibility							
Manufacturing cost	An estimate to manufacture a cell	Based on solid model and costing in software, bulk material costs					
Number of unique parts	Fewer unique parts will decrease the cost of mass producing (ie. Molds for injection molding)	Part count + tolerance in solid model					
Use of standard components	Can standard components be used to fabricated major parts of the unit	Solid model assessment					
Ability to maintain/repair design	Can units/cells be decoupled easily for maintenance without shutting down the entire engine	Assessment of assembly and installation					
Amount of peripheral equipment in a engine	ie. Does each unit need its own alternator, how many output shafts must be mechanically coupled?	Assessment of the design space					
Weight of complete engine	Total weight of the engine without external equipment such as system heat exchanges	From the solid model and 2nd order model					
Physical size of complete engine	The engine plus expected external equipment	From the solid model and 2nd order model					
Other parameters to be added		TBD					
TOTAL							

4 Next Steps

4.1 Development of complete predictive models

Understanding the various loss mechanisms in low-temperature Stirling engines is paramount to the design process and understanding how engines can be optimized and scaled. Modeling approaches exist in varying complexities, which with increasing provides improved accuracy. First order models are comparatively simple and rely on dimensionless number relationships. This provide some understanding of engine geometry and scale. Second order models begin with the ideal thermodynamic cycles, discussed in Section 2.1 and subtract the impact of various loss mechanisms from the predicted ideal cycle. The drawback of the second order modeling approach is the individual losses are assumed to be independent from one another. This can be addressed by a third order model in which each component of the engine is modeled simultaneously in a coupled sense. This allows thermodynamic and mechanical properties to be shared between each of these components. This communication within the model allows losses to interact with one another. As an example, a third order model would be capable of estimating the engine operating speed, which can be thought of as determination of the point at which the flow friction of the gas overpowers the benefits of this increased gas velocity across the heat exchangers. Instead of determining each loss independently and subtracting them from the ideal cycle, a third order model simultaneously models each component (heat exchanger, regenerator, expansion space, etc.) based on the previously computed engine state. For completeness, a fourth order model would be a full 3D, time resolved CFD model of the complete thermo-fluids. This how is not directly coupled to the mechanics of the engine limiting the understanding of the engine speed and potential produced power.

A preliminary second order model for the 90° Gamma engine was discussed in Section 3.3.2. The findings from this work demonstrated the complex interaction between the thermodynamics with the mechanical engine parameters and the importance of certain types of losses at lower temperatures. As well, the effect of engine geometry on the flow field and heat transfer needs to be understood. These effect manifest as a distinct change in the shape of the indicator diagram (Figure 35) from the predicted obtained form the second order model. With the established testing methodology, the immediate next step in the project is to develop similar models for the remaining engine configurations described in Section 2.2, as well as to continue the testing on the 90° Gamma engine to further develop this modeling work.

In conjunction with this modelling work, it is clear that a third order model must also be developed. The capabilities of this model will extend beyond the current modeling work, which was limited to a thermodynamic analysis. For this to be done, individual models for each of the various engine components must developed and implemented into the appropriate coding environment. The development and validation of these coding blocks will be done in parallel with the development of the incomplete second order modelling work that is currently ongoing.

4.2 Increasing UNIT scale

The initial design paradigm of this project was to physically increase the scale of the engines to compensate for the expected low grade heat sources. The need to do this is supported by the challenge of extracting and measuring work and torque from the current lab scale prototype UNITS. An explanation for this is that the scale of the mechanical losses from the piston and mechanism friction is the same order of magnitude of the work produced from the engine. Increasing the UNIT scale while using the identical mechanism will increase the amount of work provided by the engine, while keeping mechanism losses constant. This motivation solidifies the need to increase the UNIT scale as this project progresses.

Increased UNIT scale is accompanied by larger moving masses and a greater possibility for tolerance stacking of components, potentially effecting the concentricity between components. A number of design requirements, that were not critical at the smaller scale, may now become important. One example of this can be the inclusion of linear guide rails on the displacer and piston to educe the presence of piston side loading. Thus, to understand these scale-related considerations, large scale UNITS must be designed.

Figure 45 shows a representation of the required increase in UNIT scale and will be performed on the most promising UNIT design, however, large scale experimental setups to study oscillating heat transfer and reciprocating flow will be designed with the anticipation of engine geometries reaching this increase scale.

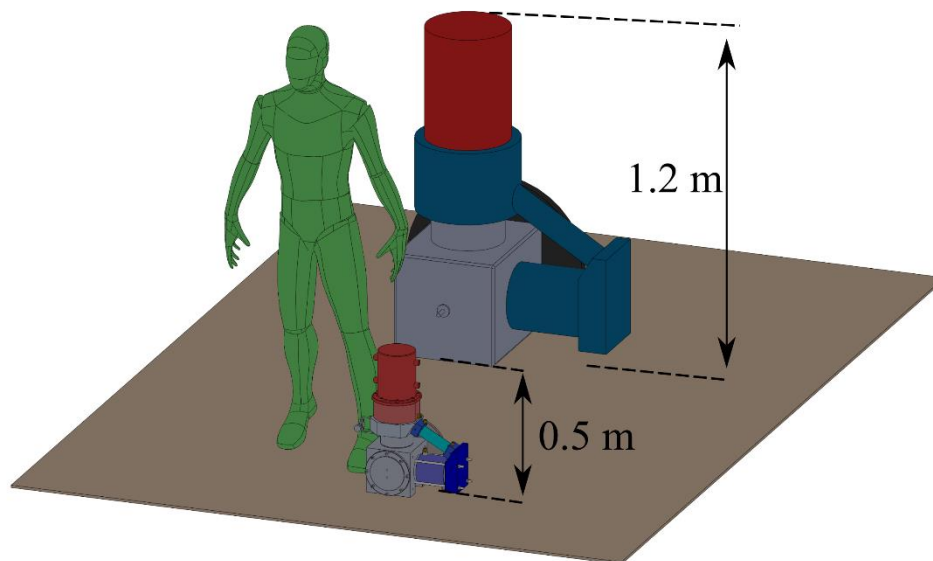


Figure 45: CAD model comparing the current scale 90° Gamma to a scaled up representation of a scaled up 90° Gamma UNIT

4.3 Configurations of CELLS

The mechanical coupling of multiple UNITS was proposed early in this project as a means to increase the usable power from the developed systems. Up until this point in the project, CELL development has consisted of developing potential multi-UNIT configurations, which are shown in the following sections. However, more complete mechanical designs will only be undertaken once more complete third order models have been developed. Complete mechanical and kinematic design cannot be done without an estimate for engine speed as the magnitude of the expected loads are directly a result of this operation condition. However, the development of a system with multiple power strokes per crankshaft revolution offer the advantage of smoother torque transmission to an alternator. Due to these potential benefits, this concept will still be explored at the appropriate stage in the project.

When hypothesising potential cell geometries, emphasis was placed on maximizing spatial efficiency of the cells to increase the maximum power density of the full scale, commercial 40' shipping container systems. The following sections outline a number of concepts to help guide future development of CELLS.

Each of the coupled UNITS in the following figures have been sized to have an evaluation length scale of approximately 1 meter. This scale corresponds to an approximate doubling of the previously discussed evaluation length scale, which corresponds to an increase in the control volume surrounding the scaled up engines by a factor of 8. This increased scale predicts an increase in West shaft work by an order of magnitude.

4.3.1 The 90° Gamma cell

A conceptual CELL shown in Figure 46 shows two coupled 90° Gamma UNITS. They share a common crank shaft and crank case with the two pistons and the two displacers opposed from each other. The shared crank case that encloses the mechanism allows the buffer space to be pressurized to minimize the presence of forced work. This specific concept shown in Figure 46 has the displacer and pistons of the individual units clocked at 180° from one another, however, this can be modified to allow changes in engine balancing or to accommodate more than two units in a cell.

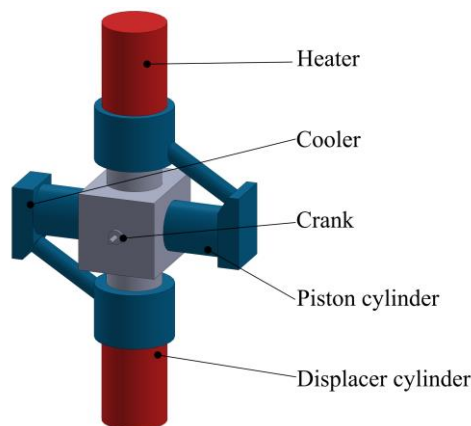


Figure 46: Conceptual CELL connecting two 90° Gamma Units

4.3.2 The ILG cell

Similar to the 90° Gamma cell, coupling the ILG CELL, shown in Figure 47, involves having multiple engines on the same crank shaft. A conceptual cell contains four UNITS coupled in a rotary fashion around a common crank. The primary issue to address with a 90° Gamma cell will be making a compact crank mechanism to improve the space efficiency of the design. This cell design would be coupled to adjacent cells through the central crank. A representation of the scale of this cell relative to a 40' sea container is shown in Figure 48.

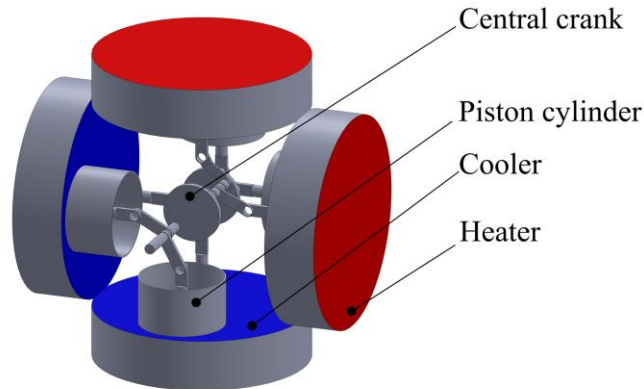


Figure 47: A conceptual ILG CELL containing four coupled in-line Gamma UNITS

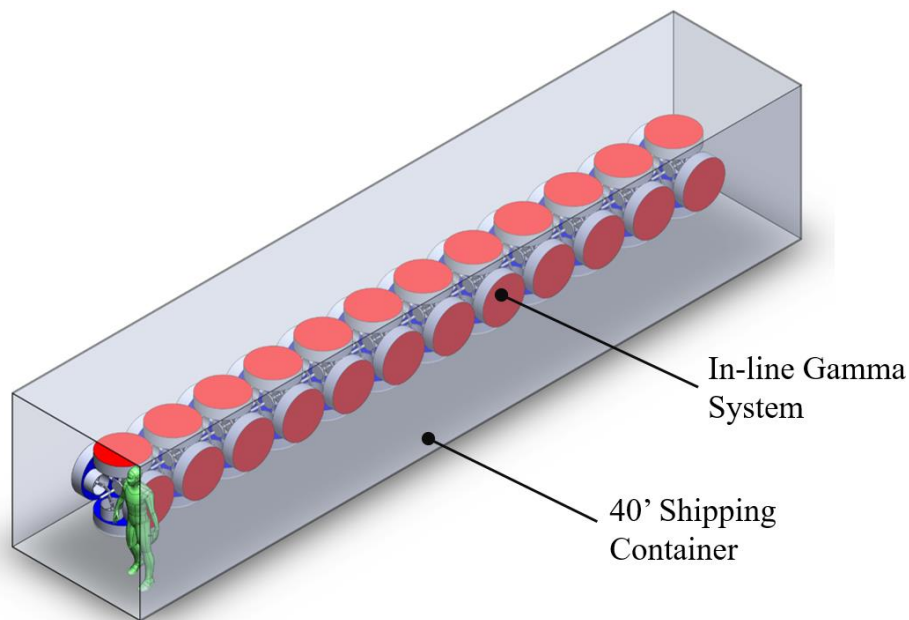


Figure 48: Schematic of a multi CELL system of inline Gamma engines inside of a 40-foot shipping container

4.3.3 The opposed piston Alpha cell

The final conceptual cell is the opposed piston Alpha. This conceptual cell contains four OPA UNITS, which are coupled to adjacent units at each of the two crank mechanisms. For such a cell configuration, power will be transmitted to adjacent cells through a central hub, which is not shown in Figure 49. The estimated scale of a multi-cell OPA system is shown in Figure 50.

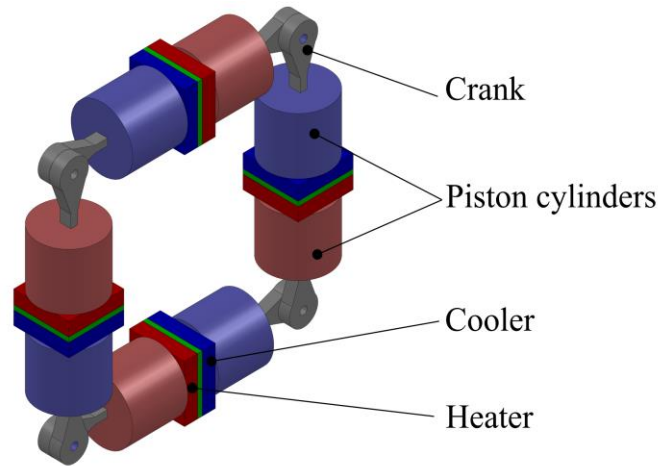


Figure 49: Conceptual CELL containing two coupled OPA units

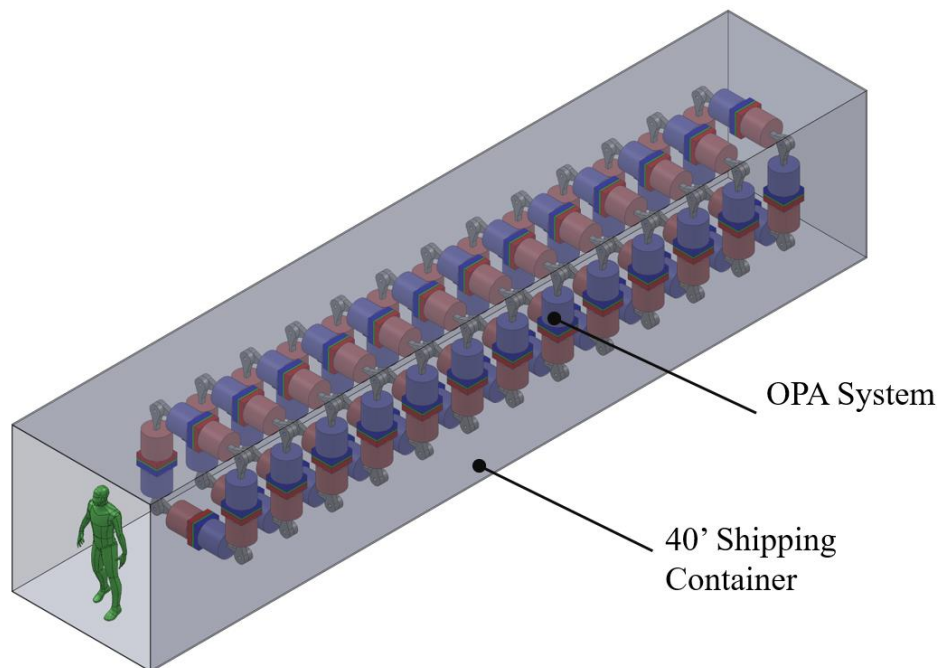


Figure 50: Schematic of a multi-CELL system of OPA engines inside of a 40-foot shipping container

4.4 Continued project funding

A Future Energy Systems grant through the University of Alberta has been secured for 7 years to continue this project. Additionally, a CRD application with Terrapin Geothermics has been submitted and a NSERC site visit has taken place on October 11, 2017.

4.5 Research Presentations and Public Events

The work discussed in this report has been presented at multiple events ranging from academic conferences to coordinated lab tours. Table 5 lists these events and provides a brief description of their intent.

Table 5: List research presentations and lab visits

Title	Date	Location	Description
ICFMHTT 2017	21-Jun-17	Venice, Italy	Academic conference where 1 academic paper was presented
AIAA Propulsion and Energy Forum	10-Jul-17	Atlanta, GA	Academic conference where 1 academic paper was prepared and presented
Okanagan Fluid Dynamics Meeting	21-Aug-17	Kelowna, BC	Academic conference where 4 academic papers were presented
FES Launch Party	14-Sep-17	Edmonton, AB	Grant event with talks from all the Geothermal projects
Helmholtz Delegation Tour	27-Sep-17	Edmonton, AB	Lab tour with the visiting academics for the Helmholtz Delegation from Germany (10-15 people)
NSERC CRD Site Visit	11-Oct-17	Edmonton, AB	CRD Site visit - 5 academics, 5 co-applicants and 5 Terrapin representatives
FES Open House	12-Oct-17	Edmonton, AB	Poster session with all the 40+ projects involved with the FES program, prepared and presented two posters
Terrapin AGM	26-Oct-17	Edmonton, AB	Lab tour for Terrapin investors (30 people)
Government of Alberta Tour	31-Oct-17	Edmonton, AB	Lab tour for Government employees (30 people)
Lab Tour	08-Nov-17	Edmonton, AB	Lab tour for university professor for government relations
Lab tour	09-Nov-17	Edmonton, AB	Lab tour for Government of Alberta Minister and company
Lab Tour	05-Dec-17	Edmonton, AB	Lab tour for high school students
Lab Tour	05-Dec-17	Edmonton, AB	Lab tour for Government of Alberta representatives
Sponsor Event	07-Dec-17	Edmonton, AB	Future Energy Systems Holiday Wrap-Up

4.6 Research publications

Significant portions of the research that is conducted is published and the full length papers are provided in Appendix A. The following is a list of all the publications to date:

- C. Stumpf, S. Middleton, and D. S. Nobes, “Heat Transfer In Oscillating Fluid Flow Through Parallel Flat Plate Channel Heat Exchangers,” in *Okanagan Fluid Dynamics Meeting*, 2017.
- J. Michaud, D. Miller, C. Speer, and D. S. Nobes, “Dimensionless Heat Transfer Correlations Of Finned-Tube Radiators In Fully Reversed Oscillating Flow,” in *Okanagan Fluid Dynamics Meeting*, 2017.
- J. P. Michaud, C. P. Speer, D. A. Miller, and D. S. Nobes, “Empirical Heat Transfer Correlations of Finned - Tube Heat Exchangers in Pulsatile Flow,” in *International Conference on Fluid Mechanics and Engineering*, 2017.
- C. P. Speer, D. A. Miller, C. J. A. Stumpf, J. P. Michaud, and D. S. Nobes, “Modification of an ST05G-CNC Stirling Engine to use a Low Temperature Heat Source,” in *American Institute of Aeronotics and Astronautics*, 2017.
- C. P. Speer, “Modifications to Reduce the Minimum Thermal Source Temperature of the ST05G-CNC Stirling Engine,” University of Alberta, 2018.

5 Conclusion

The primary objective of this project was to determine the most promising low temperature Stirling engine configuration to be scaled up and mechanically coupled to multiple identical units. To accomplish this, four UNITS with different engine configurations were designed. Throughout this design process, a number of challenges were encountered, which lead to acquiring many key learnings in design and thermal sciences.

Developing the designs and undertaking rebuilds have advanced knowledge in many areas. The ability to produce and process functional 3D printed parts is now well understood, and more importantly, the limitations of using FDM and SLA printing techniques are known for a range of applications. The importance of considering forced work is understood, can be modelled, and is compensated for in the UNIT design. The design and commission of an established engine design has offered insight into the importance of engine geometry on flow performance and has allowed a complete decoupled loss model framework to be developed.

A survey of the existing literature provides insight on the importance of properly designing to maximize energy transfer. The use of passive flow control structures will be paramount in optimizing UNIT performance, and the ability to model and predict their effectiveness is essential to the design process. As a result, UNIT designs with simple flow characteristics and geometries will greatly assist the modelling work that will accompany this project.

Configuration comparisons can be provided, yet not when considering them from a purely thermodynamic standpoint. These comparisons must be made using physical scale design decisions and through extrapolation of critical ratios. Once completed decoupled loss models have been developed, this project will rapidly advance. The methods that will be used to evaluate the UNITS have been developed and conceptual CELLS have been modelled for each engine configuration. Efforts will be spent to design scaled-up UNIT designs and once a recommendation can be made, the manufacturing process will be undertaken, along with fundamental heat transfer research to guide the heat exchanger selection and flow geometry.

6 References

- [1] J. Banks, “Deep-Dive Analysis of the Best Geothermal Reservoirs for Commercial Development in Alberta : Final Report Prepared by,” 2017.
- [2] S. Weides and J. Majorowicz, “Implications of Spatial Variability in Heat Flow for Geothermal Resource Evaluation in Large Foreland Basins: The Case of the Western Canada Sedimentary Basin,” *Energies* , vol. 7, no. 4. 2014.
- [3] “Community Integrated Energy Mapping Feasibility Study in Alberta ’ s Industrial Heartland and Strathcona Industrial Area,” 2014.
- [4] K. O’Rielly and J. Jeswiet, “Strategies to improve industrial energy efficiency,” *Procedia CIRP*, vol. 15, pp. 325–330, 2014.
- [5] G. Oluleye, M. Jobson, and R. Smith, “A hierarchical approach for evaluating and selecting waste heat utilization opportunities,” *Energy*, vol. 90, pp. 5–23, 2015.
- [6] A. Kapil, I. Bulatov, R. Smith, and J. K. Kim, “Site-wide low-grade heat recovery with a new cogeneration targeting method,” *Chem. Eng. Res. Des.*, vol. 90, no. 5, pp. 677–689, 2012.
- [7] O. M. Al-Rabghi, M. Beirutty, M. Akyurt, Y. . Najjar, and T. Alp, “Recovery and utilization of waste heat,” *Heat Recover. Syst. CHP*, vol. 13, no. 5, pp. 463–470, 1993.
- [8] R. Shoureshi, “Analysis and Design of Stirling Engines for Waste-Heat Recovery,” 1981.
- [9] J. R. Senft, *Mechanical Efficiency of Heat Engines*. Cambridge University Press, 2007.
- [10] C. D. West, *Principles and applications of Stirling engines*. Van Nostrand Reinhold, 1986.
- [11] C. M. (Clifford M. . Hargreaves, “The Philips Stirling engine.” p. 457, 1991.
- [12] W. Martini, “Stirling Engine Design Manual.” 1983.
- [13] C. Cinar and H. Karabulut, “Manufacturing and testing of a gamma type Stirling engine,” *Renew. Energy*, vol. 30, no. 1, pp. 57–66, 2005.
- [14] P. K. Pradip, “Commissioning and Performance Analysis of WhisperGen Stirling Engine,” *Master Appl. Sci. Univ. Wind.*, vol. 1, pp. 1–85, 2016.
- [15] H. Karabulut, H. S. Yücesu, C. Çınar, and F. Aksoy, “An experimental study on the development of a β -type Stirling engine for low and moderate temperature heat sources,” *Appl. Energy*, vol. 86, no. 1, pp. 68–73, 2009.
- [16] B. Kongtragool and S. Wongwises, “A review of solar-powered Stirling engines and low temperature differential Stirling engines,” *Renew. Sustain. Energy Rev.*, vol. 7, no. 2, pp. 131–154, 2003.
- [17] I. Urieli and D. Berchowitz, “Stirling Cycle Engine Analysis,” *Alternative Sources of Energy*. pp. 71–71, 1984.
- [18] F. Formosa and G. Despesse, “Analytical model for Stirling cycle machine design,” *Energy Convers. Manag.*, vol. 51, no. 10, pp. 1855–1863, 2010.
- [19] J. M. Strauss and R. T. Dobson, “Evaluation of a second order simulation for Sterling engine

- design and optimisation,” *J. Energy South. Africa*, vol. 21, no. 2, pp. 17–29, 2010.
- [20] D. Viebach, “The ST05G Stirling Engine Project.” .
- [21] C. P. Speer, D. A. Miller, C. J. A. Stumpf, J. P. Michaud, and D. S. Nobes, “Modification of an ST05G-CNC Stirling Engine to use a Low Temperature Heat Source,” in *American Institute of Aeronautics and Astronautics*, 2017.
- [22] C. P. Speer, “Modifications to Reduce the Minimum Thermal Source Temperature of the ST05G-CNC Stirling Engine,” University of Alberta, 2018.
- [23] C. Stumpf, S. Middleton, and D. S. Nobes, “Heat Transfer In Oscillating Fluid Flow Through Parallel Flat Plate Channel Heat Exchangers,” in *Okanagan Fluid Dynamics Meeting*, 2017.
- [24] J. P. Michaud, C. P. Speer, D. A. Miller, and D. S. Nobes, “Empirical Heat Transfer Correlations of Finned - Tube Heat Exchangers in Pulsatile Flow,” in *International Conference on Fluid Mechanics and Engineering*, 2017.
- [25] J. Michaud, D. Miller, C. Speer, and D. S. Nobes, “Dimensionless Heat Transfer Correlations Of Finned-Tube Radiators In Fully Reversed Oscillating Flow,” in *Okanagan Fluid Dynamics Meeting*, 2017.
- [26] J. R. Senft, *Mechanical Efficiency of Heat Engines*. New York: Cambridge University Press, 2007.
- [27] W. Callister and D. Rethwisch, “Materials Science and Engineering.” 2014.
- [28] T. D. McLouth, J. V Severino, P. M. Adams, D. N. Patel, and R. J. Zaldivar, “The impact of print orientation and raster pattern on fracture toughness in additively manufactured ABS,” *Addit. Manuf.*, vol. 18, pp. 103–109, 2017.
- [29] Y. Xu, “Experimental Study of ABS Material Shrinkage and Deformation Based on Fused Deposition Modeling,” in *MATEC Web of Conferences*, 2016, vol. 67.
- [30] K. Szykiedans and W. Credo, “Mechanical properties of FDM and SLA low-cost 3-D prints,” in *Procedia Engineering*, 2016, vol. 136, pp. 257–262.
- [31] Bellofram, “Bellofram Rolling Diaphragm Design Manual,” 2012.
- [32] K. A. M. Steele, N. S. Herbert, and V. Pretet, “A study on the effects of resin infiltration techniques on parts produced using the three-dimensional printing (3DP) process,” in *Fifth National Conference on Rapid Design, Prototyping, and Manufacturing*, 2004, pp. 71–78.
- [33] F. P. Incropera and D. P. Dewitt, “Introduction To Heat Transfer,” *Igarss 2014*, no. 1. pp. 1–5, 2014.
- [34] J. R. Seume and T. W. Simon, “Oscillating Flow In Stirling Engine Heat Exchangers.,” in *Proceedings of the Intersociety Energy Conversion Engineering Conference*, 1986, pp. 533–538.
- [35] G. Xiao, C. Chen, B. Shi, K. Cen, and M. Ni, “Experimental study on heat transfer of oscillating flow of a tubular Stirling engine heater,” *Int. J. Heat Mass Transf.*, vol. 71, pp. 1–7, 2014.
- [36] R. W. Moss, A. P. Roskilly, and S. K. Nanda, “Reciprocating Joule-cycle engine for

- domestic CHP systems,” *Appl. Energy*, vol. 80, no. 2, pp. 169–185, 2005.
- [37] A. J. White, “Thermodynamic analysis of the reverse Joule-Brayton cycle heat pump for domestic heating,” *Appl. Energy*, vol. 86, no. 11, pp. 2443–2450, 2009.
- [38] R. Mikalsen and A. P. Roskilly, “The design and simulation of a two-stroke free-piston compression ignition engine for electrical power generation,” *Appl. Therm. Eng.*, vol. 28, no. 5–6, pp. 589–600, 2008.
- [39] J. Howes, “Concept and development of a pumped heat electricity storage device,” *Proc. IEEE*, vol. 100, no. 2, pp. 493–503, 2012.
- [40] A. Altman, “Stirling engine heat transfer - A snappy primer heat exchanger design you can understand,” 2000. .
- [41] M. HINO, M. SAURAMOTO, AND S. TAKASU, “Experiments On Transition To Turbulence In An Oscillatory Pipe Flow.,” *J. Fluid Mech.*, vol. 75, no. 2, 1976.
- [42] S. I. Sergeev, “Fluid oscillations in pipes at moderate Reynolds numbers,” *Fluid Dyn.*, vol. 1, no. 1, pp. 121–122, 1966.
- [43] P. Merkli and H. Thomann, “Transition to turbulence in oscillating pipe flow,” *J. Fluid Mech.*, vol. 68, no. 3, pp. 567–576, 1975.
- [44] E. C. Nsofor, S. Celik, and X. Wang, “Experimental study on the heat transfer at the heat exchanger of the thermoacoustic refrigerating system,” *Appl. Therm. Eng.*, vol. 27, no. 14–15, pp. 2435–2442, 2007.
- [45] G. Mozurkewich, “Heat transfer from a cylinder in an acoustic standing wave,” *J. Acoust. Soc. Am.*, vol. 98, no. 4, pp. 2209–2216, 1995.
- [46] K. C. Leong and L. W. Jin, “An experimental study of heat transfer in oscillating flow through a channel filled with an aluminum foam,” *Int. J. Heat Mass Transf.*, vol. 48, no. 2, pp. 243–253, 2005.
- [47] K. C. Leong and L. W. Jin, “Heat transfer of oscillating and steady flows in a channel filled with porous media,” *Int. Commun. Heat Mass Transf.*, vol. 31, no. 1, pp. 63–72, 2004.
- [48] M. Ozawa, M. Shinoki, K. Nagoshi, and E. Serizawa, “Scaling of Heat Transfer Characteristics in an Oscillating Flow,” *J. Enhanc. Heat Transf.*, vol. 10, no. 3, pp. 275–285, 2003.
- [49] M. Wetzel and C. Herman, “Experimental study of thermoacoustic effects on a single plate. Part I: Temperature fields,” *Warme- und Stoffubertragung Zeitschrift*, vol. 36, no. 1, pp. 7–20, 2000.
- [50] M. Wetzel and C. Herman, “Experimental study of thermoacoustic effects on a single plate. Part II: Heat transfer,” *Warme- und Stoffubertragung Zeitschrift*, vol. 35, no. 6, pp. 433–441, 1999.
- [51] R. A. Peattie and R. Budwig, “Heat transfer in laminar, oscillatory flow in cylindrical and conical tubes,” *Int. J. Heat Mass Transf.*, vol. 32, no. 5, pp. 923–934, 1989.
- [52] L. S. Fishler and R. S. Brodkey, “Transition, turbulence and oscillating flow in a pipe a visual study,” *Exp. Fluids*, vol. 11, no. 6, pp. 388–398, 1991.

- [53] K. Naitoh, Y. Takagi, K. Kuwahara, E. Krause, and K. Ishii, "Computation of transition to turbulence in the compression stage of a reciprocating engine," *Fluid Dyn. Res.*, vol. 6, no. 5–6, pp. 277–294, 1990.
- [54] W.-L. Chen, K.-L. Wong, and Y.-F. Chang, "A computational fluid dynamics study on the heat transfer characteristics of the working cycle of a low-temperature-differential γ -type Stirling engine," *Int. J. Heat Mass Transf.*, vol. 75, pp. 145–155, 2014.
- [55] J. L. Salazar and W.-L. Chen, "A computational fluid dynamics study on the heat transfer characteristics of the working cycle of a β -type Stirling engine," *Energy Convers. Manag.*, vol. 88, pp. 177–188, 2014.
- [56] S. M. Nam, K. B. Lee, and S. H. Rhi, "Effect of piston bowl shape on the in-cylinder flow characteristics of IC engines," *J. Mech. Sci. Technol.*, vol. 28, no. 6, pp. 2377–2384, 2014.
- [57] F. J. Edwards and C. J. R. Alker, "Improvement Of Forced Convection Surface Heat Transfer Using Surface Protrusions In The Form Of (A) Cubes And (B) Vortex Generators.," pp. 244–248, 1974.
- [58] A. Y. Turk and G. H. Junkhan, "Heat Transfer Enhancement Downstream Of Vortex Generators On A Flat Plate.," in *Heat Transfer, Proceedings of the International Heat Transfer Conference*, 1986, vol. 6, pp. 2903–2908.
- [59] M. Fiebig, P. Kallweit, and N. K. Mitra, "Wing Type Vortex Generators For Heat Transfer Enhancement.," in *Heat Transfer, Proceedings of the International Heat Transfer Conference*, 1986, vol. 6, pp. 2909–2913.
- [60] M. Fiebig, P. Kallweit, N. Mitra, and S. Tiggelbeck, "Heat transfer enhancement and drag by longitudinal vortex generators in channel flow," *Exp. Therm. Fluid Sci.*, vol. 4, no. 1, pp. 103–114, 1991.
- [61] D. M. Rao and T. T. Kariya, "Boundary-Layer submerged vortex generators for separation Control-An exploratory study," in *1st National Fluid Dynamics Conference, 1988*, 1988.
- [62] K. Mahkamov, "An axisymmetric computational fluid dynamics approach to the analysis of the working process of a solar stirling engine," *J. Sol. Energy Eng. Trans. ASME*, vol. 128, no. 1, pp. 45–53, 2006.
- [63] K. Mahkamov, "Design improvements to a biomass stirling engine using mathematical analysis and 3D CFD modeling," *J. Energy Resour. Technol. Trans. ASME*, vol. 128, no. 3, pp. 203–214, 2006.
- [64] P. G. SAFFMAN and D. C. WILCOX, "Turbulence-Model Predictions for Turbulent Boundary Layers," *AIAA J.*, vol. 12, no. 4, pp. 541–546, Apr. 1974.
- [65] C.-T. Hsu, X. Lu, and M.-K. Kwan, "Les and rans studies of oscillating flows over flat plate," *J. Eng. Mech.*, vol. 126, no. 2, pp. 186–193, 2000.
- [66] Y. Su, J. H. Davidson, and F. A. Kulacki, "Fluid flow and heat transfer structures of oscillating pipe flows," *World Acad. Sci. Eng. Technol.*, vol. 81, pp. 653–662, 2011.

Appendix A – Published work

This section contains the work published within the scope of this project. All papers are provided in this appendix with the exception of item 6, which is the thesis written by Speer.

1. C. Stumpf, S. Middleton, and D. S. Nobes, “Heat Transfer In Oscillating Fluid Flow Through Parallel Flat Plate Channel Heat Exchangers,” in *Okanagan Fluid Dynamics Meeting*, 2017.
2. J. P. Michaud, D. Miller, C. Speer, and D. S. Nobes, “Dimensionless Heat Transfer Correlations Of Finned-Tube Radiators In Fully Reversed Oscillating Flow,” in *Okanagan Fluid Dynamics Meeting*, 2017.
3. J. P. Michaud, C. P. Speer, D. A. Miller, and D. S. Nobes, “Empirical Heat Transfer Correlations of Finned - Tube Heat Exchangers in Pulsatile Flow,” in *International Conference on Fluid Mechanics and Engineering*, 2017.
4. C. P. Speer, D. A. Miller, C. J. A. Stumpf, J. P. Michaud, and D. S. Nobes, “Modification of an ST05G-CNC Stirling Engine to use a Low Temperature Heat Source,” in *American Institute of Aeronotics and Astronautics*, 2017.
5. C. Speer, D. Miller, and D. Nobes, “Preliminary Model Validation For A Gamma Type Stirling Engine,” in *Okanagan Fluid Dynamics Meeting*, 2017, pp. 1–3.
6. C. P. Speer, “Modifications to Reduce the Minimum Thermal Source Temperature of the ST05G-CNC Stirling Engine,” MSc Thesis, University of Alberta, 2018.

HEAT TRANSFER IN OSCILLATING FLUID FLOW THROUGH PARALLEL FLAT PLATE CHANNEL HEAT EXCHANGERS

C. Stumpf, S. Middleton, and D.S. Nobes

*Department of Mechanical Engineering,
University of Alberta, Edmonton, AB.*

Abstract

In Stirling engines, the working fluid undergoes oscillatory flow which causes both unique fluid flow and heat transfer considerations. The aim of this study was to determine the Nusselt number correlations for varying displacer piston strokes and operating frequencies. Tests were completed with a displacer piston being ran by an electric motor at 0.5 Hz, 1 Hz, and 2 Hz with a stroke of 25mm and 50mm. This motion of the displacer piston caused the working fluid to be shuttled through a cold heat exchanger (5°C and 20°C) and a hot heat exchanger (60°C and 75°C). Temperature was measured using two thermocouples at the entrance and exit of each heat exchanger for a total of 8 thermocouples. Raw thermocouple data showed that the time response of the thermocouples was too long compared to the oscillation frequency. Nusselt number correlations were determined that further suggested the thermocouple response time was too long. Future work will entail the replacement of thermocouples, and the addition of a rotary encoder and displacer piston seal. Additionally, steady state unidirectional heat transfer will be completed on the heat exchangers and compared to oscillation fluid flow through the heat exchangers.

Introduction and Motivation

Stirling engines are a type of heat engine, also referred to as an external combustion engine. There are three types of Stirling engines: Alpha, Beta, and Gamma. A gamma Stirling engine uses a displacer piston to cycle a working fluid from a thermal source where heat is added, through a regenerator which pre-cools and pre-heats the working fluid by acting as both an internal heat exchanger and heat storage device, to a thermal sink where heat is rejected. A power piston is used to extract work out per cycle from the change in pressure caused by the heating

and cooling of the working fluid. The power piston and displacer piston are coupled together with the displacer piston typically leading the power piston by 90° in the cycle.

The performance and geometry of a Stirling engine primarily relies on the temperature difference of the thermal source and sink, and the heat transfer rate of the heat exchangers (source and sink), this makes Stirling engines a heat transfer limited problem. The larger the difference between the maximum and minimum temperature of the working fluid is, the larger the Carnot efficient is and more power that can be extracted from the engine. Additionally, to get more power out of a Stirling engine, the charge pressure can be increased, but only if the heat exchangers are able to sustain the minimum and maximum working fluid temperature.

When the temperature of the thermal source ($T_{source} < 150^{\circ}\text{C}$), and the temperature difference between the thermal source and sink is small ($\Delta T = 100^{\circ}\text{C}$), the Stirling engine is called a Low Temperature Difference (LTD) Stirling engine. LTD Stirling engines must minimize the amount of dead volume (volume not swept by the power or displacer piston) to only the required dead volumes of the heat exchangers and the regenerators. Dead volume is volume that does not change temperature throughout the cycle, thus reducing the overall pressure change of the engine throughout the cycle. To maximize the available surface area of the heat exchangers while minimizing the dead volume, flat plates channel heat exchangers are recommended.

This study aims to determine Nusselt number correlations for Nusselt number and average Reynolds number for oscillatory flow.

Literature Review

Studies in oscillating fluid flow heat transfers have primarily been performed in tubes (Patil and Gawali 2016), (Fan, Fulmer, and Hartenstine 2008), and little experimental work done on square ducts (Nonino and Comini 2002), (Kurzweg 1985) with flat plates. Additionally, no work has been performed on flat plate channel heat exchanges with high aspect ratios.

Work has been done in investigating Stirling engine heat exchanger performance (Simon and Seume 1988), however this is done for tube heat exchangers and in thermo acoustic Stirling engines (Jaworski and Piccolo 2012). The oscillatory fluid flow caused by the acoustic wave in a thermos acoustic Stirling engine differs from the oscillatory fluid flow caused by piston movement.

Nusselt number relations have been found for Stirling engine heat exchangers for larger operating frequencies and hotter heat exchanger temperatures than the tested in this study (Kuosa et al. 2012)

Experimental Setup and Procedure

The experimental setup used is a modified gamma Stirling engine that removes the power piston so that the displacer piston is the only piston that causes fluid motion as seen in Figure 1 and Figure 2. An internal schematic of the system can be seen in Figure 3.

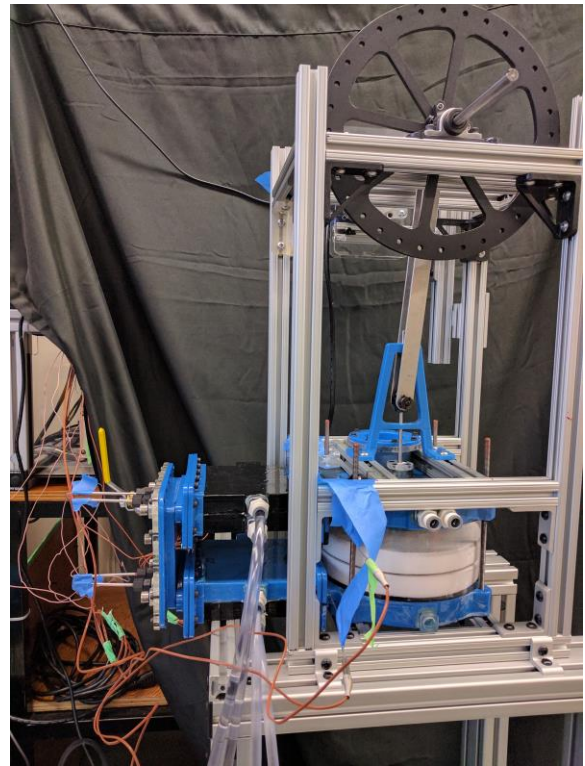


Figure 2: Experimental Setup with DAQ

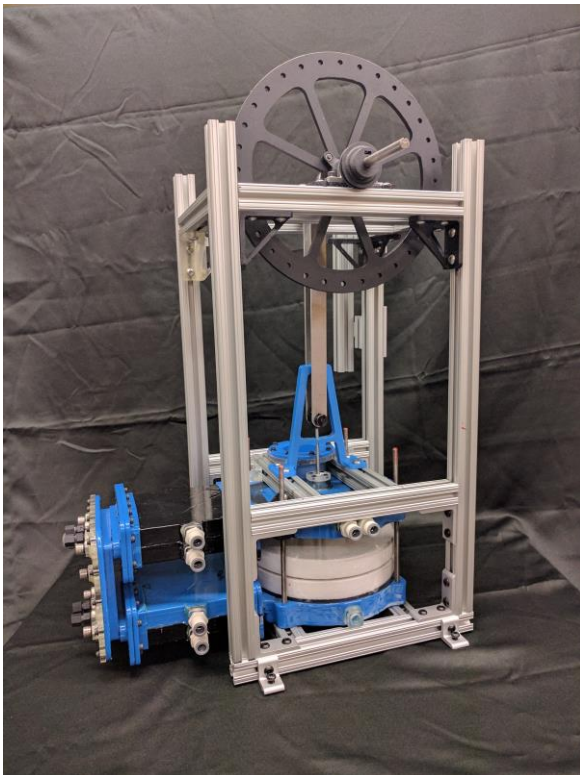


Figure 1: Experimental Setup

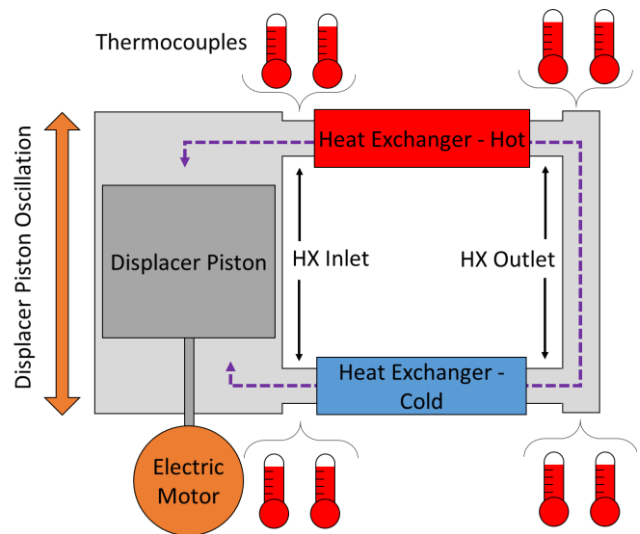


Figure 3: Experimental Setup – Internal Schematic

The displacer piston was ran by a Teknic Clearpath electric motor (CPM-MCVC-3441S-RLN) to produce the oscillatory fluid motion. Temperature was measured on the inlet and outlet of the heat exchanger for the working fluid, two thermocouples were used on each inlet and outlet for a total of eight thermocouple. The thermocouples used on the inlet were Exposed junction Type-T thermocouples (TJFT72, Omega Engineering Inc.), while the outlet thermocouples were Beaded Tip Type-T

Thermocouples (Omega Engineering Inc.). The thermocouples had a response time of 0.8 seconds and 1.6 seconds respectfully. The heat exchangers were heated and cooled from a hot (NESLAB EX 10) and cold water bath (Cole Parmer 12101-41) with both employing constant flow rate as seen in Table 2.

The DAQ device used for the thermocouples was the TC 2095 from National Instruments Inc., data was then transferred through a NI MAX SCXI 1000 low-noise chassis before arriving at the computer. The manipulated variables of the experimental setup can be seen in Table 1. The controlled variables of the experimental setup can be seen in

Table 2.

Table 1: Manipulated Variables

Parameter	Value			Unit
	Low	Med	High	
Heat Exchanger Temperature (Hot)	60	-	75	°C
Heat Exchanger Temperature (Cold)	5	-	20	°C
Displacer Piston Stroke	25	-	50	mm
Oscillation Frequency	0.5	1	2	Hz

Table 2: Controlled Variables

Parameter	Value	Unit
Heat Exchanger Width (Hot & Cold)	120	mm
Heat Exchanger Length (Hot & Cold)	130	mm
Heat Exchanger Surface Area (Hot & Cold) (2 Plates/HX)	15600	mm ²
Heat Exchanger Gap Height	2.5	mm
Hot Water Bath Volumetric Flow Rate	2.57	l/min
Cold Water Bath Volumetric Flow Rate	2.57	l/min

Assumptions

To determine the heat transfer coefficients for both the heat exchangers the following assumptions were made. The temperatures of the wall of the heat exchangers were constant. The working fluid was incompressible. Ideal gas law applies. The motion produced by the displacer piston was sinusoidal. The

working fluid has a constant specific heat. The system was leak free and no leakage took place across the displacer piston interface.

Calculations

Within calculations of non-dimensional a characteristic length equal to the hydraulic diameter of the tested exchangers was used by applying the following equation. For high aspect ratio ducts the hydraulic diameter is approximately equal to twice the thickness.

$$l_{HX} = \frac{2 \cdot w_{HX} \cdot t_{HX}}{w_{HX} + t_{HX}} \quad \text{Equation 1}$$

Density within each heat exchanger is established by the following equation.

$$\rho = \frac{P_{air}}{R \cdot (HXT_{avg} + 273.15 K)} \quad \text{Equation 2}$$

The dynamic viscosity was found be using the Sutherland equation as seen in Equation 3.

$$\mu = 1.458E - 6 \cdot \frac{(273.15 K + HXT_{avg})^{\frac{3}{2}}}{HXT_{avg} + 110.4} \quad \text{Equation 3}$$

The thermal conductivity is established by the following equation.

$$k = (1.5207E - 11) \cdot (HXT_{avg} + 273.15)^3 - (4.8574E - 08) \cdot (HXT_{avg} + 273.15 K)^2 + (1.0184E - 04) \cdot (HXT_{avg} + 273.15) - (3.9333E - 04) \quad \text{Equation 4}$$

Volume displaced is the area of the displacer multiplied by the displacer piston stroke length as seen in the following equation

$$V_{displaced} = A_{DP} \cdot s_{DP} \quad \text{Equation 5}$$

The virtual distance the air is thrust through the exchangers may be calculated by dividing this volume displaced by the displacer piston by the cross-sectional area of the heat exchanger.

$$x_{HX,max} = \frac{V_{displaced}}{CSA_{HX}} \quad \text{Equation 6}$$

By assuming an approximately sinusoidal motion of the displacer piston the maximum volumetric flow rate is established as:

$$V_{max} = V_{displaced} \cdot \frac{f}{2} \quad \text{Equation 7}$$

With the maximum and average velocity following as:

$$v_{HX,max} = \frac{V_{max}}{CSA_{HX}} \quad \text{Equation 8}$$

$$V_{avg} = \frac{V_{max}}{2} \quad \text{Equation 9}$$

The fluid flush ratio defines the number of times the air in the heat exchanger is replaced in each half cycle.

$$ffr = \frac{V_{displaced}}{V_{HX}} \quad \text{Equation 10}$$

The non-dimensional frequency, represented by the Valensi number, is calculated by the following equation.

$$Va = \rho \cdot f \cdot 2 \cdot \pi \cdot \frac{l_{HX}^2}{\mu} \quad \text{Equation 11}$$

The average and maximum Reynolds number are established using the hydraulic diameter as follows.

$$Re = \rho \cdot l_{HX} \cdot v_{HX} / \mu \quad \text{Equation 12}$$

The convective heat transfer coefficient is calculated by combining Equation 13 and Equation 14 as seen in Equation 15. The temperature of the air at the inlet and exit of each heat exchanger was averaged over ten seconds. While the average temperature was taken to be the average of the inlet and outlet temperatures. For Equation 14 the temperature of the wall was taken as the temperature of the water from the water bath. While the temperature of the working fluid was taken as the average of the temperature of the temperature of the inlet and outlet.

$$Q = V_{avg} \cdot \rho \cdot c_p \cdot |T_{air,i} - T_{air,e}| \quad \text{Equation 13}$$

$$Q = h \cdot SA_{HX} \cdot |T_{wall} - HXT_{avg}| \quad \text{Equation 14}$$

$$h = V_{avg} \cdot \rho \cdot c_p \cdot \frac{abs(T_{air,i} - T_{air,e})}{SA_{HX} \cdot abs(T_{wall} - HXT_{avg})} \quad \text{Equation 15}$$

The Nusselt number, is the ratio of convection over conduction effects is derived from the convective heat transfer coefficient as.

$$Nu = h \cdot l_{HX} / k \quad \text{Equation 16}$$

Data Processing

The raw data was loaded into MATLAB and the data for thermocouples at the same location were averaged as seen in Figure 4 and Figure 5. It was found that the response time of the thermocouples were too large to track the change in the temperature of the working fluid and instead was recording something closer to the average air temperature at that location.

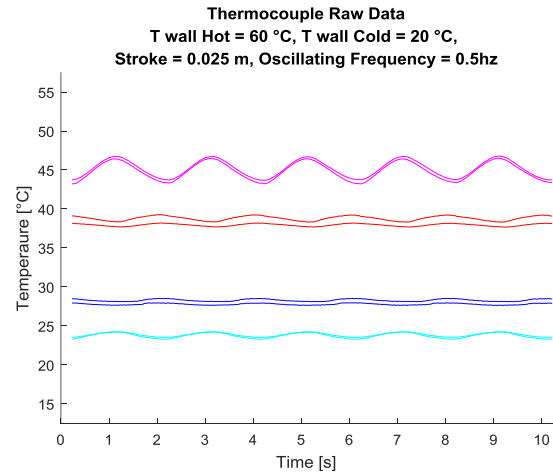


Figure 4: Thermocouple Raw Data

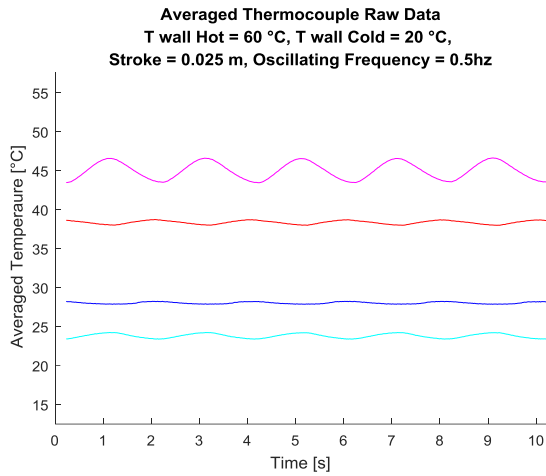


Figure 5: Averaged Thermocouple Raw Data

Results and Discussions

The Nusselt number for both the hot and cold heat exchanger cases was found to be less than one as seen in Figure 6, Figure 7, Figure 8, and Figure 9, this suggests that conduction was the dominate heat transfer method in both heat exchanger. This could be due to the small thickness of the heat exchanger where the boundary layers make up a significant portion of the distance between the two heat exchanger plates.

For the hot heat exchanger the Nusselt number was found to increase for all Valensi number with no significant differences in the trends between the 25mm and 50mm stroke as seen in Figure 6. A similar trend was found when the Nusselt number was plotted with respect to the average Reynolds numbers in the heat exchanger with data for both strokes providing a strong correlation.

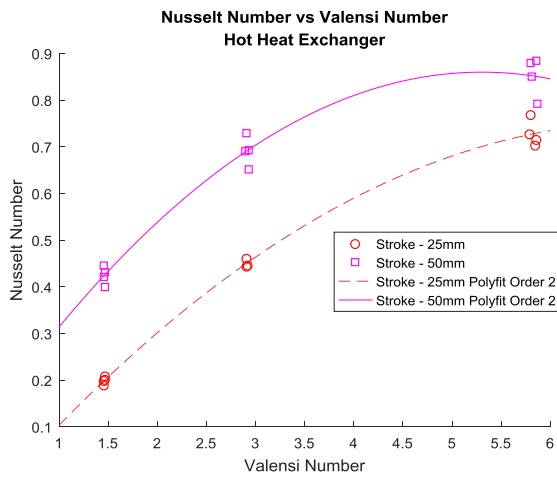


Figure 6: Nusselt Number vs Valensi numbers for hot heat exchanger with temperatures @ $T = 60^{\circ}\text{C}$, 75°C

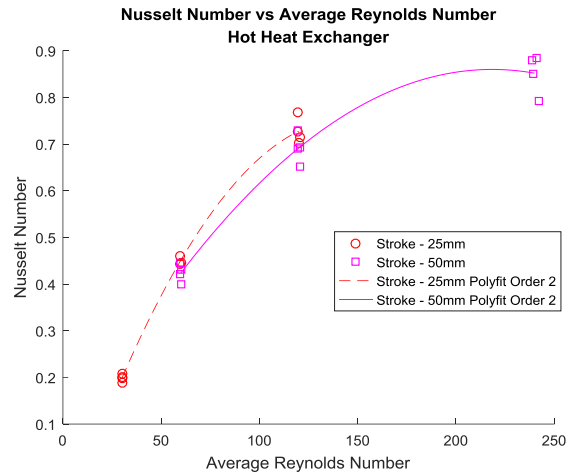


Figure 7: Nusselt Number vs Reynolds numbers for hot heat exchanger with temperatures @ $T = 60^{\circ}\text{C}$, 75°C

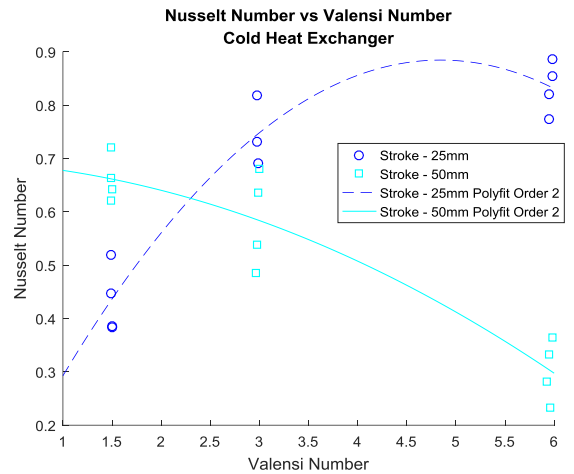


Figure 8: Nusselt Number vs Valensi numbers for cold heat exchanger with temperatures @ $T = 5^{\circ}\text{C}$, 20°C

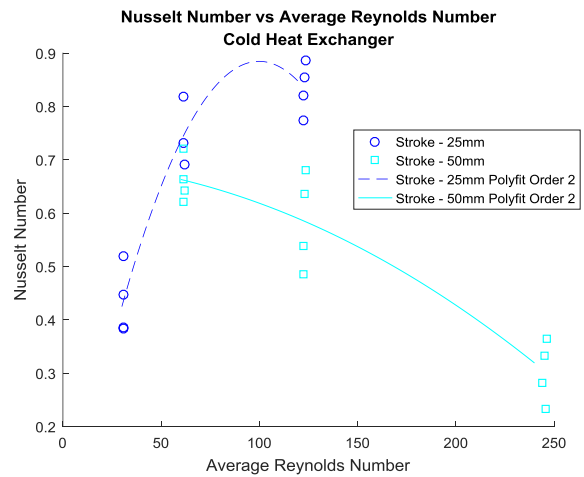


Figure 9: Nusselt Number vs Reynolds numbers for cold heat exchanger with temperatures @ $T = 5^{\circ}\text{C}$, 20°C

For the cold heat exchanger the Nusselt number was found to increase for all Valensi number only for the 25mm stroke while for the 50mm stroke the Nusselt number decreased with increasing Valensi number and average Reynolds number. This could be caused by the temperature of the thermocouples at the inlet and the outlet of the cold heat exchanger coming close to the same value at higher frequencies as seen for the 50mm stroke in Figure 11 compared to the 25 mm stroke under the same conditions in Figure 10.

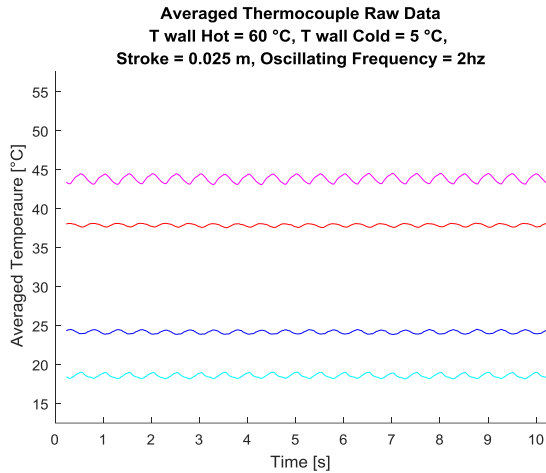


Figure 10: Averaged Thermocouple Raw Data (25mm)

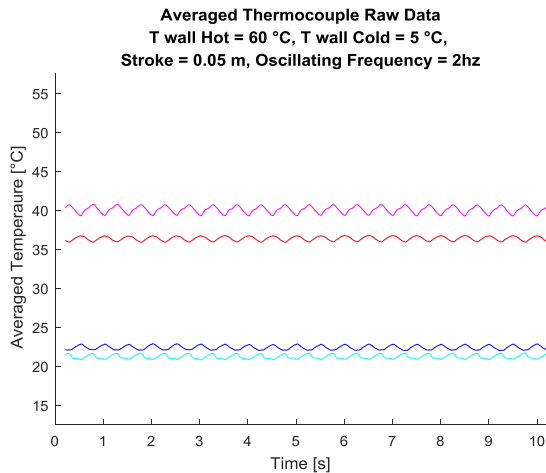


Figure 11: Averaged Thermocouple Raw Data (50mm)

Conclusions and Future Work

Under some conditions the Nusselt number appeared to trend downwards with increasing Valensi/Reynolds number. The exact cause of this trend is unclear however an analysis of the raw data suggests that leakage from the hot to the cold side of the displacer may alter the measured convective heat transfer

coefficient. Due to the large response time on the thermocouples relative to the oscillation frequency, further work is required to validate the Nusselt number relations. This can be accomplished by utilizing thermocouples with a smaller response time.

Future work will consist implementation of thermocouples with a smaller response time along with the addition of a rotary encoder to log displacer position throughout the cycle. With the position of the displacer piston known the time and position in the cycle for a particle to enter and exit the heat exchanger can be determined which will lead to a more accurate determination of the Nusselt number. Additionally, a seal for the displacer piston can be added to eliminate any air that flows around the displacer piston instead of through the heat exchangers.

Acknowledgments

The authors are grateful for funding from Natural Sciences and Engineering Research Council (NSERC) of Canada, the Canadian Foundation for Innovation (CFI), Alberta Innovates Energy and Environment Solutions, and Terrapin Geothermics.

References

- Fan, Angie, Doreen Fulmer, and J Hartenstine. 2008. "Experimental Study of Oscillating Flow Heat Transfer." *Asme 2008*: 1–8.
- Jaworski, Artur J, and Antonio Piccolo. 2012. "Heat Transfer Processes in Parallel-Plate Heat Exchangers of Thermoacoustic Devices—numerical and Experimental Approaches." *Applied Thermal Engineering* 42(0): 145–53.
- Kuosa, M., K. Saari, A. Kankkunen, and T. M. Tveit. 2012. "Oscillating Flow in a Stirling Engine Heat Exchanger." *Applied Thermal Engineering* 45–46: 15–23.
- Kurzweg, U. H. 1985. "Flows Within Parallel-Plate Channels." *Journal of Fluid Mechanics* 156(May): 291–300.
- Nonino, C., and G. Comini. 2002. "Convective Heat Transfer in Ribbed Square Channels." *International Journal of Numerical Methods for Heat & Fluid Flow* 12(5): 610–28.
- Patil, Jitendra D, and B S Gawali. 2016. "Experimental Study of Heat Transfer Characteristics in Oscillating Fluid Flow in Tube." *Experimental Heat Transfer* 30(4): 1–13.
- Simon, Terrence W., and Jorge R. (university of Minnesota) Seume. 1988. "A Survey of Oscillating Flow in Stirling Engine Heat Exchangers." *Contractor* (March): 136.

Appendix

Nomenclature

Symbol	Name	Units
r_{DP}	Displacer piston radius	[m]
A_{DP}	Displacer piston area	[m ²]
l_{HX}	Heat Exchanger Characteristic Length	[m]
w_{HX}	Heat Exchanger Width	[m]
t_{HX}	Heat Exchanger Thickness	[m]
s_{DP}	Stroke length	[m]
SA_{HX}	Heat Exchanger Surface Area	[m ²]
CSA_{HX}	Heat Exchanger Cross-Sectional Area	[m ²]
V_{HX}	Heat Exchanger Volume	[m ³]
$c_{p,h}, c_{p,c}$	Specific Heat Capacity of Air at average temperature	[J/kg K]
P_{air}	Absolute Air Pressure	[Pa]
R	Specific Gas Constant of Air	[J/kg K]
ρ_h, ρ_c	Density of air at average temperature of exchanger	[kg/m ³]
μ_h, μ_c	Dynamic viscosity of air at average temperature in exchanger	[Pa s]
k_h, k_c	Thermal conductivity of air at average temperature of exchanger	[W/m K]
HXT_{avg}	Average temperature of air within exchanger	[°C]
$V_{displaced}$	Volume displaced by displacer piston	[m ³]
$x_{HX,max}$	Distance air is displaced each cycle	[m]
V_{max}	Maximum volumetric flow rate through system	[m ³ /s]
V_{avg}	Average volumetric flow rate through system	[m ³ /s]

v_{max}	Maximum velocity through exchanger	[m/s]
$v_{HX,avg}$	Average velocity through exchanger	[m/s]
ffr	Fluid flush ratio	
Va	Valensi Number	
Re_{max}	Maximum Reynolds number	
Re_{avg}	Average Reynolds number	
$T_{air,i}, T_{air,e}$	Temperature at the inlet and outlet of heat exchanger	[°C]
h	Convective heat transfer coefficient	[W/m K]
Nu	Nusselt number	

DIMENSIONLESS HEAT TRANSFER CORRELATIONS OF FINNED-TUBE RADIATORS IN FULLY REVERSED OSCILLATING FLOW

J. Michaud, D. Miller, C. Speer, M. Nicol-Seto and D.S. Nobes

*Department of Mechanical Engineering,
University of Alberta, Edmonton, AB.*

Abstract

An experimental study was performed on three radiator sizes in oscillating flow. Two of the same radiators, one hot and one cold, were inserted in a duct with an oscillation generator. The piston stroke was varied from 50.8 mm to 152.4 mm in 25.4 mm increments. Frequency varied from 50 rpm to 200 rpm in 50 rpm increments. It was found that at lower speeds, the temperature oscillations were observed, but at higher speeds, the oscillations were attenuated. The temperature of the air near the ceiling of the duct was observed to be up to 10 °C higher than at the base.

Introduction

The application of low-grade heat Stirling engines (LGHSE), with a maximum operating temperature below 150 °C, is under investigation. The narrow operating temperature boundaries of LGHSEs require highly effective heat transfer in order to produce usable power, and so heat exchanger effectiveness is of critical importance to LGHSE design.

Oscillating working fluid flow within Stirling engines presents a challenge for heat exchanger design. It is expected that the oscillating flow velocity profile will have lower fluid velocities near the center of the flow at higher oscillation frequencies, when the flow changes direction (Simon and Seume, 1988). Additionally, oscillating flows tend to be laminar when accelerating and turbulent when decelerating (Organ, 2014). The design of the heat exchanger for a LGHSE may be enhanced with a deeper understanding of the performance of heat exchangers under oscillating flow conditions.

Several authors have conducted experiments for characterizing oscillating flow in heat exchangers. A summary of the knowledge of oscillating flow in Stirling

engine heat exchangers was completed by Simon (1988). Tang and Cheng (1993) and Zhao and Cheng (1996) developed cycle averaged Nusselt number correlations for circular pipes that are a function of Reynolds number, Valensi number, and dimensionless fluid displacement. (Kuosa et al., 2012) compared those correlations to circular pipes with geometric disturbances; however, they did not develop new correlations for their experiments. Nsofor et al. (2007) and Tang et al. (2014) determined Nusselt number correlations to Reynolds number, Prandtl number and Valensi number for finned heat exchangers in thermoacoustic devices. Recently, Patil and Gawali (2016) showed that the convective heat transfer coefficient decreases with increasing frequency between 0.5 Hz and 2.5 Hz for oscillating flow in circular tubes. The literature presents several oscillating flow, heat transfer correlations; however, the correlations' applicability to the current geometry is unknown.

The present experiment aims to study the effects of oscillating flow on small-scale radiators for 120 mm fans. A range of frequencies and amplitudes were tested to approximate the fluid flow conditions within a LGHSE while neglecting pressure swing effects.

Experiment Setup

The experiment setup consist of four key sections: the experiment duct, the oscillation generator, the cooling loop, and the heating loop. Figure 1 is a process and instrumentation diagram of the experiment setup, and Figure 2 is a picture of the experiment duct and oscillation generator.

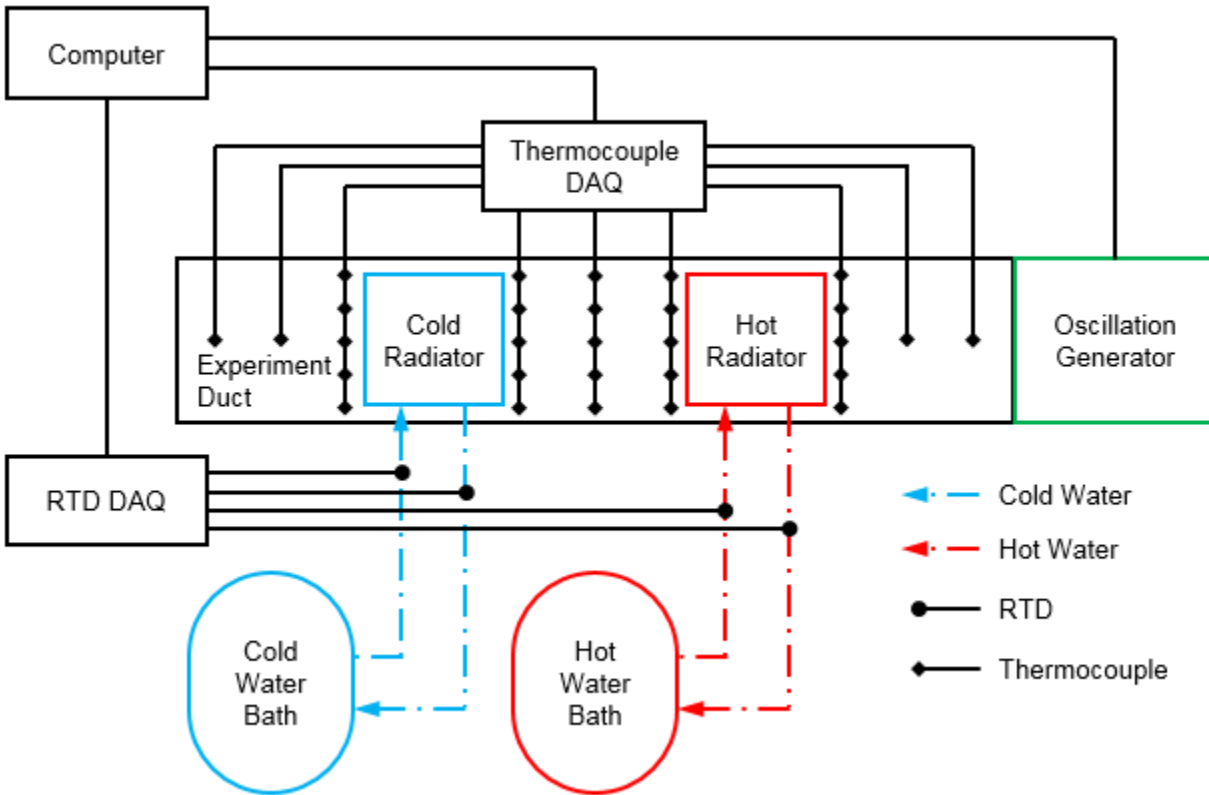


Figure 1: Process and Instrumentation Diagram of Oscillating Flow Heat Transfer Test Rig

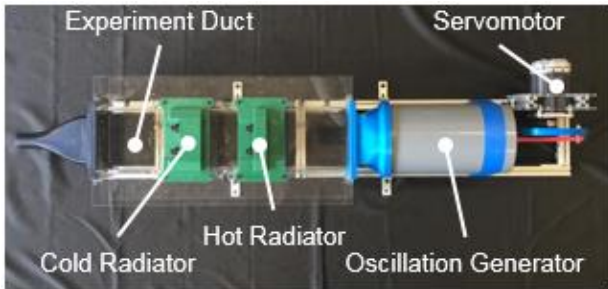


Figure 2: Annotated Picture of the Experiment Duct and Oscillation Generator

Experiment Duct

The 610 mm long, 144 mm wide, and 113.7 mm high acrylic experiment duct was built to test the performance of radiators sized for 120 mm computer fans. Air was utilized as the working fluid, and the experiment duct contained 29 thermocouples to measure air temperature. One end of the experiment duct was attached to an oscillation generator, while the other was attached to an air containment bag to isolate the system from the ambient air.

The radiators examined in the experiment were the EK-CoolStream XE 120, the EK-CoolStream PE 120, and the EK-CoolStream SE 120. The radiators consist of flat tube water channels with brazed louvered fins

that form triangular flow passages for air. Table 1 lists the dimensions of the radiators. Each experiment used two of the same size radiator, and the oscillation generator induced an oscillating fluid motion across the radiators.

Figure 3 (a) contains the longitudinal dimensions of the duct, the radiator positions, and the longitudinal locations of the thermocouple locations. The thermocouple clusters on either side of each radiator and at the mid-plane consisted of five thermocouples as depicted in Figure 3 (b). The four remaining thermocouples further from the radiators were located in the center of the flow channel.

Table 1: List of Radiator Dimensions

Radiator	Width (mm)	Height (mm)	Depth (mm)	Heat Transfer Surface Area (cm ²)
XE 120	120	125	46	9319
PE 120	127	114	22	5961
SE 120	114	120	16	3511

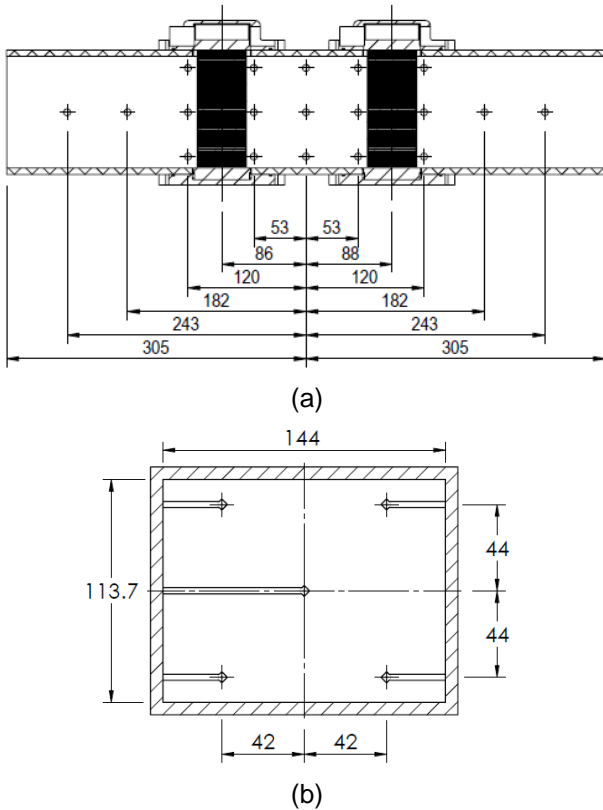


Figure 3: (a) Longitudinal dimensions and (b) cross section dimensions of the experiment duct (dimensions in mm)

Oscillation Generator

The oscillation generator provided fully reversed oscillatory fluid motion to the experiment duct. A slider-crank mechanism converted the rotary motion of a servomotor (ClearPath CPM-MCVC-3441S-RLN, Teknic) to be approximately sinusoidal, linear, motion of a 141.25 mm diameter piston.

Cooling Loop

Cold water removed heated air in the experiment duct through the cold radiator. A refrigerated water bath (12101-41, Cole-Parmer Canada Company) circulated the cold water at a rate of 0.0545 kg/s. The set point of the refrigerated bath was 5 °C. RTDs measured the cold radiator inlet and outlet temperatures.

Heating Loop

A water bath (EX 10, NESLAB) supplied hot water to the hot radiator in the experiment duct at a rate of 0.0545 kg/s. The set point of the hot water bath was 60 °C. Like the cooling loop, the hot radiator inlet and outlet temperatures were measured by RTDs.

Data Acquisition

Thermocouple Data Acquisition

Twenty-nine exposed junction Type-T thermocouples (TJFT72, Omega Engineering Inc.) gathered the air temperature data in the experiment duct. A thermocouple data acquisition device (TC 2095, National Instruments Inc.) and a NI MAX SCXI 1000 low-noise chassis transferred all the air temperature data to the data acquisition computer.

RTD Data Acquisition

RTD probes (RTD-810, Omega Engineering Inc.) measured temperature at the inlets and outlets of the cold and hot radiators. The NI 9217 RTD data-acquisition-device transferred all the water temperature data to the data acquisition computer. The RTDs were calibrated by inserting them into the water baths and determining their offset.

Data Acquisition Software

A custom data acquisition software was written to collect both thermocouple and RTD data. The sample rate for both the thermocouples and RTDs was 50 Hz and the sampling duration was 10 seconds. Data for all 29 thermocouples, 4 RTDs and both timers were stored in a single log file for data processing.

Experiment Methodology

The responding variables of the experiment are the measured air and water temperature differences across both the hot and cold radiators. The manipulated variables were the radiator surface area, piston stroke, and the frequency of oscillation. The piston stroke was varied from 50.8 mm to 152.4 mm in 25.4 mm increments. Frequency varied from 50 rpm to 200 rpm in 50 rpm increments (0.83 – 3.33 Hz in 0.83 Hz increments).

Data Processing

Heat transfer rate, convective heat transfer coefficient, Reynolds number, Valensi Number, and Nusselt number are commonly used to characterize the performance of radiators in oscillating flow.

Table 2: Nomenclature

Symbol	Description	Unit
A_a	Cross-sectional area of radiators	m^2
A_s	Surface area of radiators exposed to air	m^2
$c_{p,w}$	Specific heat of water	$J/(kg \text{ } ^\circ C)$
d_p	Piston diameter	m
f	Oscillation frequency	Hz
h	Convective heat transfer coefficient of air	$W/(m^2 \text{ } ^\circ C)$
k	Thermal conductivity of air	$W/(m \text{ } ^\circ C)$
L	Radiator fin depth	m
L_c	Characteristic length	m
\dot{m}	water mass flow rate	kg/s
Nu	Cycle average Nusselt number	-
\dot{Q}	Heat transfer rate	W
Re	Cycle average Reynolds number	-
S	Piston Stroke	m
T_e	Radiator water exit temperature	$^\circ C$
T_i	Radiator water inlet temperature	$^\circ C$
T_a	Air temperature in Radiator	$^\circ C$
T_s	Radiator surface temperature	$^\circ C$
v_{avg}	Cycle average air speed	m/s
Va	Valensi Number	-
μ	Viscosity of air	$kg/(m \text{ } s)$
ρ	Density of air	$kg/(m^3)$

Heat Transfer Rate

The heat transfer rate was calculated using Equation (1). It was assumed that the energy removed from the water to heat the radiator was equivalent to the amount of energy absorbed by the air. Similarly, the amount of energy removed from the air by the radiator on the cold side was equivalent to the amount of energy absorbed by the water. Hence, the heat transfer rate was assumed to be the same for the air and the water, and the convective heat transfer coefficient, h , of the air may be determined.

$$\dot{Q} = \dot{m} \cdot c_{p,w} (T_i - T_e) = h \cdot A_s (T_s - T_a) \quad (1)$$

Characteristic Length

Kays and London (1964) defined a characteristic length for compact heat exchangers, as shown in Equation (2).

$$L_c = 4 \cdot \frac{A_s}{A_a} \cdot L \quad (2)$$

Cycle Averaged Reynolds Number

In oscillating flow, Reynolds number varies with time, which is inconvenient when developing correlations. Therefore, a cycle averaged Reynolds number was used in Equation (3).

$$Re = \frac{\rho \cdot v_{avg} \cdot L_c}{\mu} \quad (3)$$

The average fluid speed in a cycle is found with conservation of mass between the experiment duct and the oscillation generator over half a cycle. With an incompressible fluid, the volume transfer between the two is the swept volume, which occurs over half a cycle. The average fluid speed was determined in Equation (4).

$$v_{avg} = \frac{(\pi / 4 \cdot d_p^2 \cdot S) \cdot 2 \cdot f}{A_a} \quad (4)$$

Valensi Number

Valensi number is a dimensionless frequency used to describe oscillating fluid motion. It is common in Stirling engine fluid mechanics and is also known as kinetic Reynolds number. It is calculated in Equation (5) (Kuosa et al., 2012):

$$Va = \frac{\rho \cdot (2 \cdot \pi \cdot f) \cdot L_c^2}{\mu} \quad (5)$$

Cycle Averaged Nusselt Number

Nusselt number describes the relative influence of convection to conduction as a mode of heat transfer in fluids, as shown in Equation (6).

$$Nu = \frac{h \cdot L_c}{k} \quad (6)$$

Results

Error! Reference source not found. Figure 5 shows an example spatial temperature distribution throughout the oscillating flow duct. It was observed that the temperatures were up to 10 °C higher near the ceiling of the duct relative to the floor, which may be due to the density differences between the hot and cold air. Additionally this may be caused by the air not being entirely flushed through the experiment duct. As such, the hot air does not reach the cold radiator and vice versa.

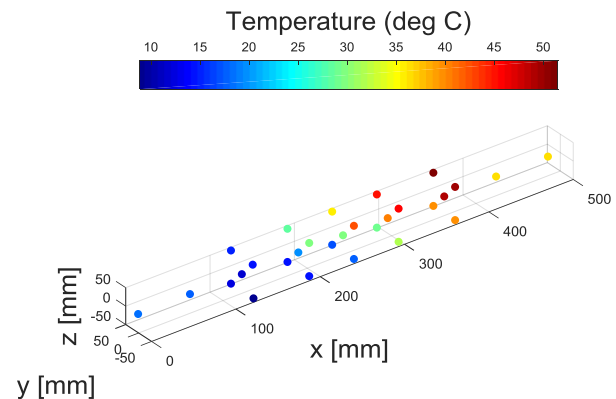


Figure 4: 3D Plot of Spatial Temperature Distribution in the Experiment Duct

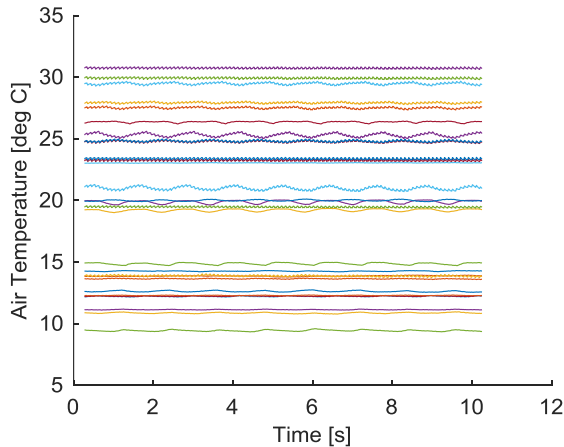


Figure 5: Raw Data Plot for the XE Radiator at 50 RPM and 50.8 mm Stroke

Figure 5Error! Reference source not found. gives an example of raw air temperature data collected for the operating point of 50 RPM, 50.8 mm stroke, and the XE radiator. Consistent time averages confirm that the experiment was at a steady oscillatory state when the measurements were taken. The small oscillations indicate potential noise in the measurement. The larger of the two temperature oscillations matches the frequency of the air flow; however, the time response of the thermocouples is inadequate to capture the full temperature swing amplitude. It was found that as the frequency increases, the thermocouples do not adequately capture the temperature oscillations.

Due to the variability in the water volume flowrate during the experiment, the improper flush ratio of the duct, and experiment conditions variability, the data used to calculate the heat transfer rate, and hence the Nusselt number was corrupted. Therefore, future work will be needed to improve the data collection process to be able to obtain Nusselt number correlations and the heat transfer performance of the three radiators.

Conclusions and Future Work

The heat transfer performance of three finned-tube heat exchangers in oscillatory flow was investigated. It was observed that the air temperature was up to 10 °C higher near the ceiling of the duct relative to the floor, which may be due to improper fluid flushing in addition to the difference in air density.

Acknowledgments

The authors are grateful for funding from Natural Sciences and Engineering Research Council (NSERC) of Canada, the Canadian Foundation for Innovation (CFI), Alberta Innovates Energy and Environment Solutions, and Terrapin Geothermics.

References

- Kays, WM; London A. “*Complact Heat Exchangers.*” 2nded. McGraw-Hill, 1964.
- Kuosa M., Saari K., Kankkunen A. and Tveit T. M. “Oscillating Flow in a Stirling Engine Heat Exchanger,” *Applied Thermal Engineering.* **45–46.** Elsevier Ltd, 15–23, 2012.
- Nsofor E. C., Celik S. and Wang X. “Experimental Study on the Heat Transfer at the Heat Exchanger of the Thermoacoustic Refrigerating System,” *Applied Thermal Engineering.* **27,** 2435–42, 2007.
- Organ A. J. “*Stirling Cycle Engines: Inner Workings and Design.*” Chichester: John Wiley and Sons Ltd., 2014.
- Patil J. D. and Gawali B. S. “Experimental Study of Heat Transfer Characteristics in Oscillating Fluid Flow in Tube,” *Experimental Heat Transfer.* **30,** 1–13, 2016.
- Simon T. W. and Seume J. R. (university of M. “A Survey of Oscillating Flow in Stirling Engine Heat Exchangers,” NASA Contractor Report., 136, 1988.
- Tang K., Yu J., Jin T., Wang Y. P., Tang W. T. and Gan Z. H. “Heat Transfer of Laminar Oscillating Flow in Finned Heat Exchanger of Pulse Tube Refrigerator,” *International Journal of Heat and Mass Transfer.* **70,** 811–18, 2014.
- Tang X. and Cheng P. “Correlations of the Cycle-Averaged Nusselt Number in Periodically Reversing Pipe Flow,” *International Communications in Heat and Mass Transfer.* **20,** 161–72, 1993.
- Zhao T. S. and Cheng P. “Oscillatory Heat Transfer in a Pipe Subjected a Periodically Reversing Flow,” *ASME Journal of Heat Transfer.* **118,** 592–98, 1996.

Empirical Heat Transfer Correlations of Finned-Tube Heat Exchangers in Pulsatile Flow

Jason P. Michaud, Connor P. Speer, David A. Miller, David S. Nobes

Abstract—An experimental study on finned-tube radiators has been conducted. Three radiators found in desktop computers sized for 120 mm fans were tested in steady and pulsatile flows of ambient air over a Reynolds number range of $50 < Re < 900$. Water at $60\text{ }^\circ\text{C}$ was circulated through the radiators to maintain a constant fin temperature during the tests. For steady flow, it was found that the heat transfer rate increased linearly with the mass flow rate of air. The pulsatile flow experiments showed that frequency of pulsation had a negligible effect on the heat transfer rate for the range of frequencies tested (0.5 Hz – 2.5 Hz). For all three radiators, the heat transfer rate was decreased in the case of pulsatile flow. Linear heat transfer correlations for steady and pulsatile flow were calculated in terms of Reynolds number and Nusselt number.

Keywords—Finned-tube heat exchangers, radiators, heat transfer correlations, pulsatile flow, computer radiators.

I. INTRODUCTION

STIRLING engines are currently being investigated for utilization of low-grade heat sources below $150\text{ }^\circ\text{C}$. Heat exchanger design optimization for Stirling engines presents a significant challenge due to unsteady, compressible, flow for which there is limited experimental data. This paper develops linear empirical heat transfer correlations for finned-tube heat exchangers in both steady and pulsatile flows. Although real fluid motion in a Stirling engine is more complex, this research provides a stepping-stone towards its understanding.

Several authors have conducted numerical investigations on the effect of pulsatile flow on heat exchanger performance. Cho and Hyun [1] solved the laminar boundary layer equations numerically for pulsating flow in a circular pipe. They found that the Nusselt number for pulsatile flow can increase or decrease relative to the steady flow value, depending on the pulsation frequency. It was determined by Chattopadhyay et al. [2] that for laminar flow in a circular pipe, pulsation had a negligible effect on the time-averaged heat transfer rate for low frequency and amplitude. For turbulent flow in a circular pipe, numerical results indicated a heat transfer enhancement, at an optimum value of Womersley number, a dimensionless variable which describes the relationship between frequency and viscous forces [3]. Kim et al. [4] considered pulsatile flow in a two-dimensional channel

filled with porous media. Their results showed that pulsatile flow decreased the heat transfer rate in the entrance region of the channel and increased it at moderate downstream locations. Further along the channel, the pulsation was ineffectual. They also noted that the pulsatile flow showed the largest deviation from steady flow at large amplitudes and small values of the pulsation frequency parameter. In the case of a curved pipe, the calculations of Chung and Hyun [5] showed that for small Womersley numbers, the Nusselt number was decreased for pulsatile flow. As Womersley number increased, the pulsatile flow Nusselt number approached the steady flow case.

Other authors have also explored pulsatile flow heat exchange experimentally. Habib et al. [6] demonstrated that the Nusselt number enhancement depends strongly on pulsation frequency for a laminar flow of air in a circular pipe. For turbulent flow in a similar geometry, a paper by the same first author reported that the Nusselt number could be increased, decreased, or unchanged relative to the steady flow case, depending on the frequency and Reynolds number [7].

Wantha [8] studied finned tube heat exchangers in steady and pulsatile flows of air. The experiment covered a frequency range of 10 to 50 Hz, and a relative amplitude range of 13.33 to 15.35%. Wantha's results showed that the Nusselt number could be increased relative to steady flow. The increase was greater for higher Reynolds numbers, and each Reynolds number had a unique optimum frequency for Nusselt number enhancement.

This study considers both steady, and pulsatile flow applied to the air side of a computer radiator. The results are applicable to computer cooling system design, and provide insight on unsteady flow heat exchangers in general.

II. EXPERIMENT SET-UP

A process and instrumentation diagram of the experiment setup is shown in Fig. 1 and compared with an image of the actual experiment in Fig. 2. Air flowed from an accumulation tank, through a mass flow controller (MC500, Cole-Parmer Canada Company) into the experiment duct via a diffuser. The custom 3D printed diffuser expanded the flow geometry from a $\frac{3}{4}$ in NPT fitting to the rectangular duct and provided a more uniform velocity profile in the duct. The rectangular duct was a 0.61 m long acrylic airflow channel built to test the performance of radiators sized for 120 mm fans. Fig. 3 contains the cross-sectional dimensions of the experiment duct. The radiators examined are the EK-CoolStream XE 120, the EK-CoolStream PE 120, and the EK-CoolStream SE 120 whose dimensions and surface areas are in Table I and

J. P. Michaud, C. P. Speer, and D. A. Miller are M.Sc. candidates in the Department of Mechanical Engineering, University of Alberta, Edmonton, AB T6G 2G8 Canada (e-mail: jpmichau@ualberta.ca, cspeer@ualberta.ca, damiller@ualberta.ca).

D. S. Nobes is a Professor with the Department of Mechanical Engineering, University of Alberta, Edmonton, AB T6G 2G8 Canada (e-mail: dnobes@ualberta.ca).

depicted in Fig. 4. After passing through the radiator, air exited the experiment duct to ambient, through a nozzle. To maintain the radiators near 60 °C, a hot water bath (EX 10,

NESLAB) circulated distilled water through the radiator in an open loop.

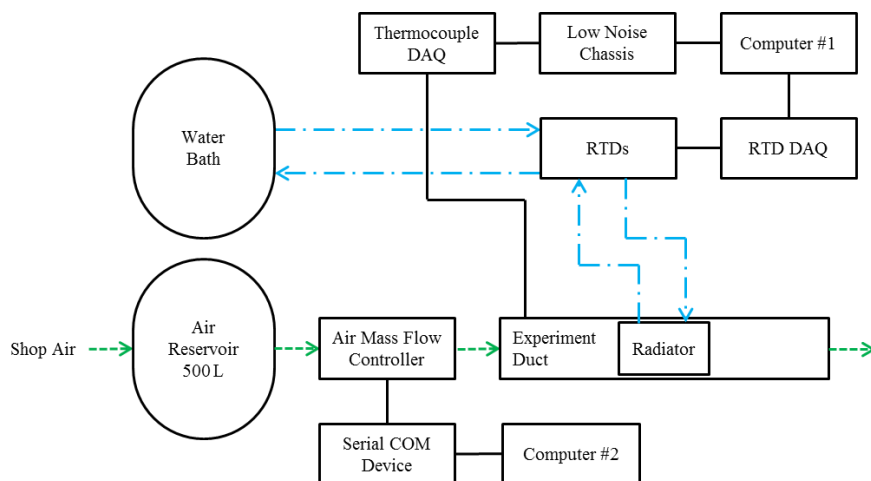


Fig. 1 Process and Instrumentation Diagram of The Radiator Testing Experiment

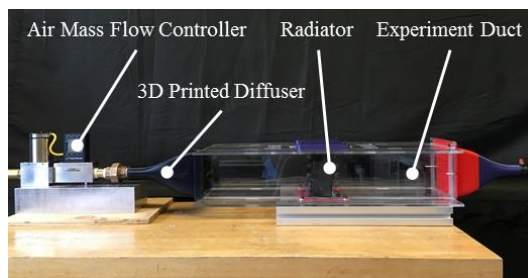


Fig. 2 Image of the Experiment Setup

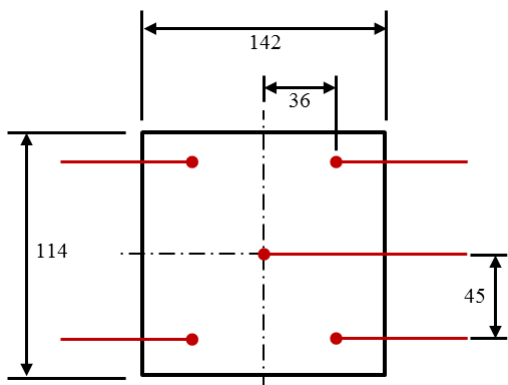


Fig. 3 Cross-Sectional Diagram of Experiment Duct with Thermocouple Locations in Red (dimensions in millimeters)

TABLE I
RADIATOR DIMENSIONS

Radiator	Width (mm)	Height (mm)	Depth (mm)	Heat Transfer Surface Area (cm ²)
XE 120	120	125	46	9319
PE 120	127	114	22	5961
SE 120	114	120	16	3511

A. Temperature Measurement Instruments

Both air and water temperature data were logged for analysis. Exposed junction Type-T thermocouples (TJFT72,

Omega Engineering Inc.) measured air temperature in the experiment duct in eleven positions—five immediately before and after the radiator in the locations shown in Fig. 3 and one in the exhaust nozzle. Two RTD probes (RTD-810, Omega Engineering Inc.) measured the water inlet and outlet temperature of the radiator.

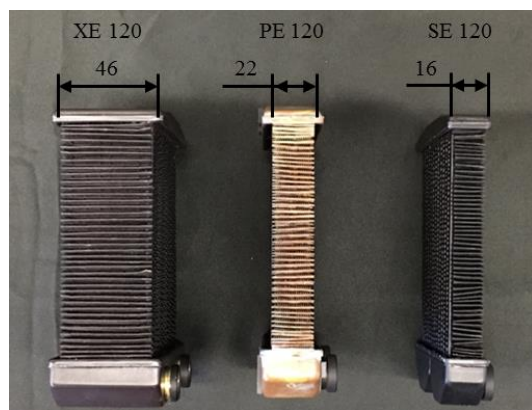


Fig. 4 Images of All Three Radiators with Depth Dimensions (dimensions in millimeters)

B. Data Acquisition

One computer (Comp #1) gathered all the temperature data. The thermocouple data-acquisition-device (TC 2095, National Instruments Inc.) transmitted air temperature data to computer 1 via the NI MAX SCXI 1000 low-noise chassis. The NI 9217 RTD data-acquisition-device transmitted the water temperature data to Comp #1. Comp #1 alternately collected data from each data-acquisition-device at a frequency of 1 Hz.

A second computer (Comp #2) was responsible for the air mass flow controller. Comp #2 commanded the air mass flow controller to change or maintain its set point at a frequency of 10 Hz through a NI USB-232/2 serial COM device. Similarly, the mass flow controller returned volume flow rate, mass flow

rate, temperature, and pressure measurements at a 10 Hz through the serial COM device. Comp #2 logged the command set point and all the flow controller data.

III. EXPERIMENT METHODOLOGY

TABLE II
NOMENCLATURE

Symbol	Description	Unit
A_{air}	Cross-sectional area of radiators exposed to air	m ²
A_s	Surface area of radiators exposed to air	m ²
c_p	Constant pressure specific heat	J/(kg °C)
f	Pulsation frequency	Hz
h	Convective heat transfer coefficient of Air	W/(m ² °C)
k	Thermal conductivity of air at 40 °C	W/(m °C)
L	Radiator fin depth	m
\dot{m}	Air mass flow rate	kg/s
Nu	Nusselt Number	-
\dot{Q}	Heat transfer rate	W
Re	Reynolds Number	-
T_{in}	Radiator air inlet temperature	°C
T_s	Radiator surface temperature	°C
v	Average air velocity in radiator	m/s
ΔT	Arbitrary temperature difference	°C
μ	Viscosity of air at 40 °C	kg/(m s)
ρ	Density of air at 40 °C	kg/(m ³)

The responding variables of the experiment are the measured air and water temperature difference. As seen in (1), the heat transfer rate, \dot{Q} , may be calculated for each radiator by varying the mass flow rate, \dot{m} , and measuring the temperature difference, ΔT , assuming a constant specific heat, c_p such as:

$$\dot{Q} = \dot{m} \cdot c_p \cdot \Delta T \quad (1)$$

For the steady state experiments, the manipulated variables were the radiator surface area and air flow rate. For the pulsatile flow experiments, radiator surface area, pulse frequency and amplitude were the manipulated variables. The internal control system of the water bath maintained the water temperature at 60 °C. Water mass flow rate was determined by weighing six 40 s samples of water circulated through the system for each radiator.

A. Steady Flow Experiments

In the steady flow experiments, constant airflow rates were passed through each radiator in random order. Table III lists the two groups of flow rates that flowed through the radiators. The lower group is from 50 to 100 LPM for comparison with the pulsatile mean airflow rates. The higher group is from 100 to 300 to expand the steady flow data. All 30 experiments were 400 s to ensure sufficient steady state data was gathered.

B. Pulsatile Flow Experiments

The pulsatile flow experiments had pulsating airflow rates passing through each radiator at several frequencies as listed in Table IV. Similarly, to the steady flow experiments, the pulsatile flow experiment was performed in random order with

respect to the maximum airflow set point and pulsation frequency. The anticipated mean pulsatile airflow rates correspond to the lower group of steady state flow rates. Equipment limitations restricted the range of airflow set points and pulsation frequencies available for analysis. Again, all 90 experiments were 400 s long to ensure enough data was collected at thermal steady state.

TABLE III
STEADY FLOW MANIPULATED VARIABLES

Number	Air Flow Rate Set point (LPM)
1	50
2	60
3	70
4	80
5	90
6	100
7	150
8	200
9	250
10	300

TABLE IV
PULSATILE FLOW MANIPULATED VARIABLES

Number	Air Flow Rate Setpoint Maximum (LPM)	Pulsation Frequency (Hz)
1	100	0.5
2	120	1.0
3	140	1.5
4	160	2.0
5	180	2.5
6	200	-

IV. DATA PROCESSING

Heat transfer rate, convective heat transfer coefficient, Reynolds number and Nusselt number characterize the performance of radiators. The calculations used constant properties of air at 40 °C and atmospheric pressure. Furthermore, calculations applied mean air mass flow rate data averaged over the entire dataset. Calculations requiring temperatures used the mean temperature averaged beyond data point 300 (approximately 300 s) to ensure the thermally transient portion of the data was ignored.

Fig. 5 presents a sample of the raw data collected for the inlet and outlet temperatures for both steady and pulsatile flows. Both the steady flow and pulsatile flow samples stabilize after approximately 300 s.

The average air velocity, v , through the radiator was calculated using:

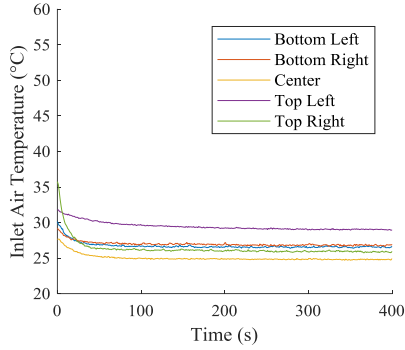
$$v = \frac{\dot{m}}{(\rho \cdot A_{air})} \quad (2)$$

where the air mass flow rate is \dot{m} , the density of the air is ρ , and the surface area of the radiator exposed to air is A_{air} .

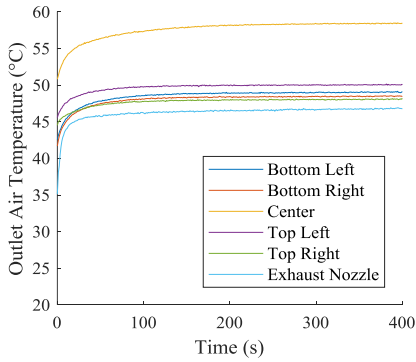
The Reynolds number, Re , for the air was then calculated using:

$$Re = \frac{\rho \cdot v \cdot L}{\mu} \quad (3)$$

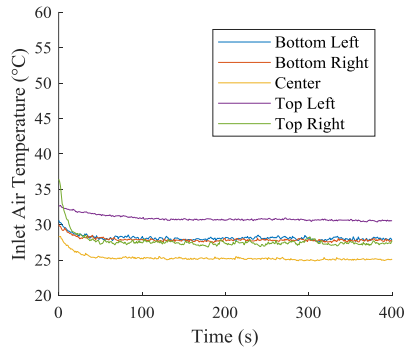
where μ is the dynamic viscosity of air, and L is the characteristic length scale, which was assumed to be the length of the fins in the flow direction [9].



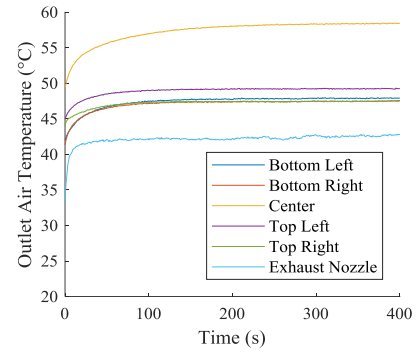
(a)



(b)



(c)



(d)

Fig. 5 Raw data plots of (a) the steady flow inlet air temperature and (b) outlet air temperature through radiator XE 120 with a set point of 70 LPM; and (c) raw data plots of pulsatile flow inlet air temperature (d) and outlet air temperature through radiator XE 120 with a maximum set point of 140 LPM at a pulsation frequency of 1.0 Hz

The convective heat transfer coefficient, h , was calculated using:

$$h = \frac{\dot{Q}}{(A_s \cdot (T_s - T_{in}))} \quad (4)$$

with the heat transfer rate from (1), surface area of each radiator, A_s , shown in Table I, the radiator surface temperature, T_s , which was measured to be approximately 59 °C, and the averaged air inlet temperature, T_{in} .

The Nusselt number, Nu , was calculated for a thermal conductivity k is the of the air using:

$$Nu = \frac{h \cdot L}{k} \quad (5)$$

V. RESULTS AND DISCUSSION

Fig. 6 is a plot of heat transfer rate with respect to mean mass flow rate for all three radiators. As expected, the heat transfer rate increases with an increase in mass flow rate. Additionally, the XE 120 radiator, with the largest surface area, has a greater heat transfer rate followed by the PE 120, and SE 120.

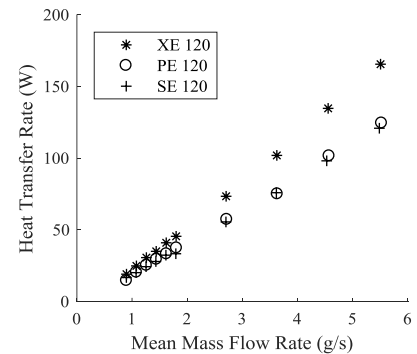


Fig. 6 Plot Comparing Steady Flow Heat Transfer Rate and Mean Mass Flow for Each Radiator

Fig. 7 shows the steady and pulsatile heat transfer rates for the XE 120 radiator. The graph indicates that the performance of the radiator is superior for steady flow compared to pulsatile flow. However, the advantage is not distinct since both data sets nearly collapse to a straight line. In addition, the frequency of pulsation did not have a significant effect on the heat transfer rate for the frequency range of 0.5 Hz to 2.5 Hz.

Fig. 8 demonstrates the heat transfer rate as a function of average mass flow rate for the PE 120 radiator. The results indicate that the performance of the radiator is also decreased by the pulsatile flow. However, similar to the XE 120, the pulsatile and steady data are not significantly different in terms of performance enhancement.

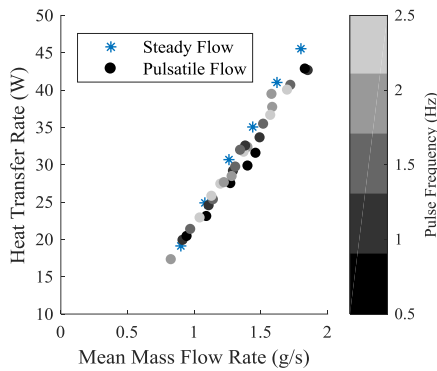


Fig. 7 Plot Comparing Heat Transfer Rate and Mean Mass Flow for Steady and Pulsatile Flows for the EK XE 120

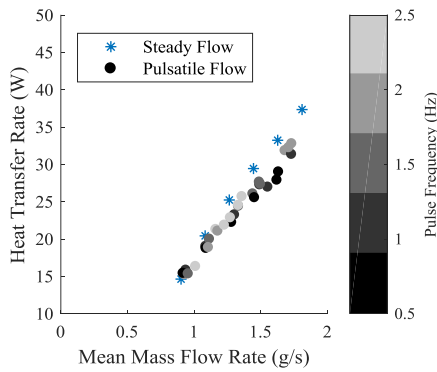


Fig. 8 Plot Comparing of Heat Transfer Rate and Mean Mass Flow for Steady and Pulsatile Flows for the EK PE 120

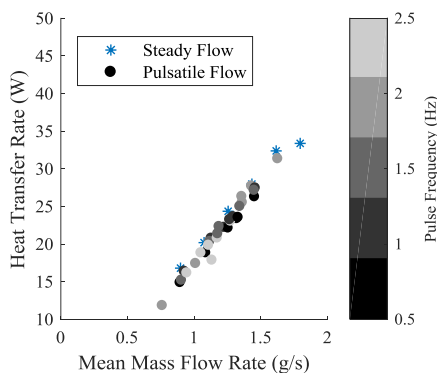


Fig. 9 Plot Comparing of Heat Transfer Rate and Average Mass Flow for Steady and Pulsatile Flows for the EK SE 120

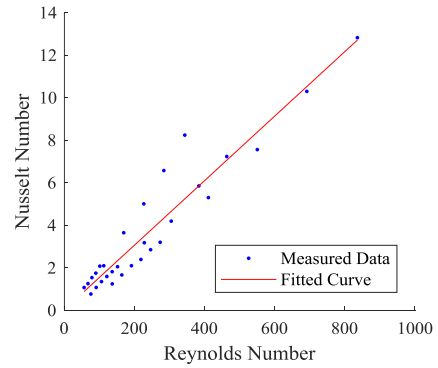


Fig. 10 Plot Correlating Steady Flow Nusselt Number and Reynolds Number

Similar to the XE and PE radiator the SE 120 radiator also has a decreased heat transfer rate under pulsatile flow conditions. Data supporting this is presented in Fig. 9.

Figs. 7-9 indicate that, for the conditions tested here, pulsatile flow has a negative effect on the rate of heat transfer from finned-tube radiators tested.

Fig. 10 shows the Nusselt number correlation for steady flow conditions. Three distinct lines of data are visible, corresponding to the three radiators tested. The separation of the three lines can be attributed to the geometric differences between the three radiators. The Reynolds number, as calculated here, does not overcome the differences in fin structure and tube layout that exist between the three radiators. A linear polynomial fit was calculated to produce the Nusselt number correlation for steady flow, shown in (6). The R^2 value for the linear fit was 0.904.

$$Nu = 0.01517 \cdot Re + 0.3523 \quad (6)$$

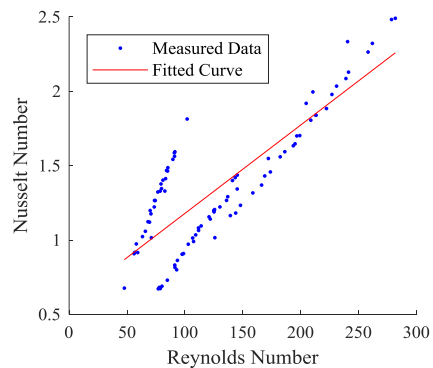


Fig. 11 Plot Correlating Pulsatile Flow Nusselt Number and Reynolds Number

Fig. 11 corresponds to pulsatile flow. The Reynolds number was based on the average flow velocity through the radiator. The R^2 value was 0.6968, indicating a poor fit relative to the steady flow case. Similarly, three distinct lines can be seen in Fig. 11, which indicate that the Reynolds number definition did not adequately capture the geometric differences between the radiators. A more detailed dimensionless number would be required to improve the fit. The correlation equation for pulsatile flow is shown in (7):

$$Nu = 0.00594 \cdot Re + 0.5850 \quad (7)$$

VI. CONCLUSIONS AND FUTURE WORK

The heat transfer performances of three finned-tube heat exchangers in both steady and pulsatile flows were investigated. The results of this study indicate that pulsatile flows decrease heat transfer rates for the range of geometries and flow conditions tested.

Future work would include testing a wider range of flow conditions, including oscillating flow and compressible flow, to better represent flows present in low temperature Stirling engines. The pressure drop across the radiators should also be correlated to facilitate design optimization. Additionally, different dimensionless numbers and characteristic length scales should be explored to produce more universal design plots.

ACKNOWLEDGMENT

This work was conducted with the support of the Natural Sciences and Engineering Research Council (NSERC) of Canada, the Canadian Foundation of Innovation (CFI), Alberta Innovates Energy and Environment Solutions, and Terrapin Geothermics. Micheal Bayans, Carlos Mendez, and Jakub Piwowarczyk provided advice and equipment support.

REFERENCES

- [1] H. W. Cho and J. M. Hyun, "Numerical solutions of pulsating flow and heat transfer characteristics in a pipe," *Int. J. Heat Fluid Flow*, vol. 11, no. 4, pp. 321–330, 1990.
- [2] H. Chattopadhyay, F. Durst, and S. Ray, "Analysis of heat transfer in simultaneously developing pulsating laminar flow in a pipe with constant wall temperature," *Int. Commun. Heat Mass Transf.*, vol. 33, no. 4, pp. 475–481, 2006.
- [3] X. Wang and N. Zhang, "Numerical analysis of heat transfer in pulsating turbulent flow in a pipe," *Int. J. Heat Mass Transf.*, vol. 48, no. 19–20, pp. 3957–3970, 2005.
- [4] S. Kim, B. Kang, and J. Hyun, "Heat transfer in the thermally developing region of a pulsating channel flow," *Int. J. Heat Mass Transf.*, vol. 36, no. 17, pp. 4257–4266, 1993.
- [5] J. Chung and J. Hyun, "Heat transfer from a fully-developed pulsating flow in a curved pipe," *Int. J. Heat Mass Transf.*, vol. 37, no. 1, pp. 43–52, 1994.
- [6] M. A. Habib, A. M. Attya, A. I. Eid, and A. Z. Aly, "Convective heat transfer characteristics of laminar pulsating pipe air flow," *Heat Mass Transf.*, vol. 38, no. 3, pp. 221–232, 2002.
- [7] M. A. Habib, S. A. M. Said, A. A. Al-Farayedhi, S. A. Al-Dini, A. Asghar, and S. A. Gbadebo, "Heat transfer characteristics of pulsated turbulent pipe flow," *Heat Mass Transf.*, vol. 34, no. 5, pp. 413–421, 1999.
- [8] C. Wantha, "Effect and heat transfer correlations of finned tube heat exchanger under unsteady pulsating flows," *Int. J. Heat Mass Transf.*, vol. 99, pp. 141–148, 2016.
- [9] M. Carl, D. Guy, B. Leyendecker, A. Miller, and X. Fan, "The Theoretical and Experimental Investigation of the Heat Transfer Process of an Automobile Radiator," in *ASEE Gulf Southwest Annual Conference*, 2012, vol. 1, no. 128, pp. 1–12.

Jason P. Michaud is from Sherwood Park, Alberta, Canada, and is a MSc. Candidate in the Department of Mechanical Engineering at the University of Alberta, Edmonton, Alberta, Canada. He completed his BSc. of mechanical engineering in 2016 at the same institution.

Connor P. Speer is an MSc Candidate in the Department of Mechanical

Engineering at the University of Alberta in Edmonton, Alberta, Canada. He completed a BSc. In Mechanical engineering in 2015 at the same institution.

David A. Miller was raised in St. Paul, Alberta, Canada. He completed a BSc. of mechanical engineering at the University of Alberta, Edmonton, Alberta, Canada in 2016. His is currently a MSc. Candidate in the Department of Mechanical Engineering at the University of Alberta.

David S. Nobes has a BE and PhD in mechanical engineering from the University of Adelaide, Australia. He is now a Professor in the Department of Mechanical Engineering at the University of Alberta, Canada.

Modification of an ST05G-CNC Stirling Engine to Use a Low Temperature Heat Source

Connor P. Speer¹, David A. Miller¹, Calynn J.A. Stumpf¹, Jason P. Michaud¹
University of Alberta, Edmonton, Alberta, Canada, T6G 2G8

and

David S. Nobes²
University of Alberta, Edmonton, Alberta, Canada, T6G 2G8

Preliminary modeling and experiments have been performed on a modified ST05G-CNC Stirling engine aiming to lower the minimum thermal source temperature at which it will run for a given thermal sink temperature. Modeling results indicated that decreasing the piston/displacer swept volume ratio would improve performance for source temperatures between 85 °C and 150 °C, relative to the original engine design. Experiments were performed using two piston diameters: 44 mm and 85 mm. It was found that decreasing the piston swept volume improved low temperature difference operation due to a decrease in forced work and crankcase gas spring hysteresis loss.

Nomenclature

A	= area
E	= mechanism effectiveness
f	= Reynolds friction factor
k	= thermal conductivity
m	= mass of gas
Q	= heat
\dot{Q}	= heat transfer rate
Re	= Reynolds number
T	= temperature
V	= volume
W	= work
τ	= torque
<i>actual</i>	= subscript for actual
c	= subscript for compression space
e	= subscript for expansion space
f	= subscript for forced
h	= subscript for heater
i	= subscript for indicated
<i>ideal</i>	= subscript for ideal
k	= subscript for cooler
r	= subscript for regenerator
s	= subscript for shaft

¹ MSc. Candidate, Department of Mechanical Engineering, 116 St & 85 Ave, Edmonton, AB T6G 2R3.

² Professor, Department of Mechanical Engineering, 116 St & 85 Ave, Edmonton, AB T6G 2R3.

I. Introduction

The Stirling engine is a reciprocating, closed-cycle heat engine. Compared to other externally heated engines such as Rankine or Ericsson engines, Stirling engines have the advantage of being relatively simple. The Stirling engine is currently being considered for small scale distributed electricity production, which utilize low grade heat sources such as flat plate solar collectors, geothermal wells, or industrial processes. Specifically, this research targets heat sources in the 85 °C to 150 °C temperature range with a rejection temperature of 0 °C to 25 °C. The low conversion efficiencies associated with these low temperature heat sources require a large, inexpensive Stirling engine system to be economically viable for electricity generation.

To date, the majority of the literature features engines with hot side temperatures of greater than 500 °C [1]–[6]. Far fewer investigations delve into the 85 °C to 150 °C heat source temperature regime [7], [8]. The aim of this study is to bridge the gap between high and low temperature source Stirling engine design. This will be accomplished by testing a Stirling engine over a wide source temperature range (95 °C to 500 °C). To achieve this, a high temperature difference engine will be modified with the intent of lowering its minimum source temperature while keeping a constant sink temperature. The goal is to provide insight on the application of high temperature source engine design methods to low source temperature engines.

Stirling engine design focuses on comparisons to thermodynamic models which range in complexity from simple hand calculations, to complicated numerical solutions [2]. In the ideal isothermal model, the defining assumption is infinite heat transfer through the piston cylinder walls [9]. The Schmidt analysis is a special case of the ideal isothermal model which additionally assumes sinusoidal volume variations to obtain a closed form analytical solution [9]. Short heat transfer times and low surface area to volume ratios invalidate the isothermal cylinder assumption in practical high temperature engines [2]. The ideal adiabatic model considers the opposite extreme, with negligible heat transfer in the cylinder walls [9]. A numerical solution is required for this more complicated model. Both of these models ignore several losses that reduce the performance of real engines. These losses include flow friction, imperfect heat transfer, working fluid leakage, mechanical friction, and appendix gap losses [10]. The interdependence of these losses makes optimization of Stirling engine geometry difficult. A common design approach is to ignore the coupling of these losses and estimate them individually [2]. Analyses which make this assumption are termed second order methods [2]. For a more accurate but computationally demanding simulation, a third order method, also known as nodal analysis, can be used [2]. This method involves dividing the engine into small volumes and solving conservation equations for each [2]. Choice of the appropriate model depends on the resources available and the desired accuracy.

In this study, a second order model is used. It is a modified version of the well-known “simple” model described by Urieli and Berchowitz [9], and available for download on Urieli’s website [11]. The modifications include the addition of parasitic losses, the use of slider-crank mechanism volume variations, and a loop scheme that facilitates study of engine parameters. Here, the model is used to identify dominant losses and predict their behavior as the temperature difference is decreased.

The experimental engine is a modified version of the ST05G-CNC designed by Ve-Ingenieure of Germany [12]. Experimental studies have been performed by other researchers using similar engines. Gheith et al. [13]–[15] performed several experiments using a stock ST05G-CNC Stirling engine. These experiments consisted of changing the working fluid from air to helium, as well as varying the material and porosities of the regenerator. Bert et al. used an ST05G Stirling engine to quantify the effects of rotational speed, charge pressure, and hot side temperature on the engine performance [16]. Hooshang et al. [17] considered the dynamic response characteristics of the ST05G Stirling engine for use in control system design. The experiments of these authors did not extend to source temperatures below 300 °C. The goal of this work is to explore the differences between high and low temperature difference Stirling engines, by decreasing the minimum operating temperature difference of the ST05G-CNC.

II. Mathematical Model

The model used in this work is a second order model based on the well-known “Simple” model of Urieli and Berchowitz [9]. The forced work principles described by Senft [7] are also employed to account for mechanical friction. Other losses are calculated using the equations presented by Urieli and Berchowitz [9]. Details of the model are described below.

A. Main Assumptions

The model begins by assuming that the power and efficiency of the engine may be calculated by subtracting losses from the baseline values corresponding to an ideal scenario. Here, the ideal power and efficiency values are determined using the ideal adiabatic model described by Urieli and Berchowitz [9]. The ideal adiabatic model makes the following assumptions [9]:

1. Adiabatic compression and expansion spaces.
2. Isothermal heater, cooler, and regenerator spaces.
3. No pressure drop across components.
4. Mass of working fluid is constant (no leakage).
5. The ideal gas law is applicable.
6. Kinetic and potential energies of the working fluid are neglected.

These assumptions give rise to the ideal gas temperature distribution shown in Fig. 1 below.

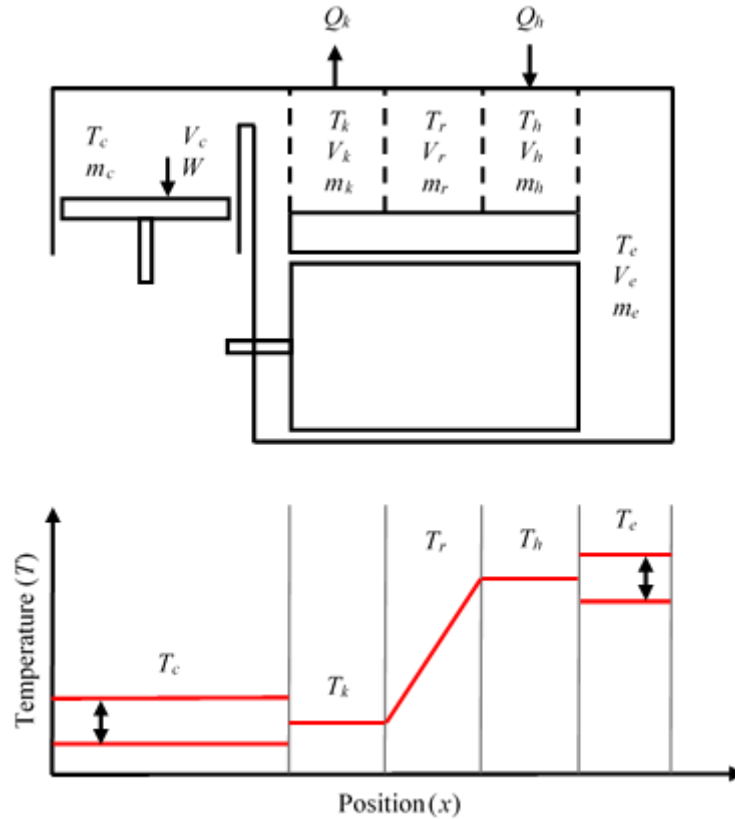


Fig. 1. Assumed Working Fluid Temperature Distribution for the Ideal Adiabatic Model of Urieli and Berchowitz

The additional assumptions necessary to calculate the decoupled losses will be described in the coming subsections.

B. Application of “Simple” Model

1. Separation of Isothermal and Adiabatic Spaces

In the simple model, each region is defined as adiabatic or isothermal. Fig. 1 displays the temperature profile in a generic gamma Stirling engine. Here the compression and expansion spaces are adiabatic and the heat exchangers are isothermal (heater, cooler, and regenerator). This corresponds to the specific analysis of the modified ST05G-CNC Stirling engine presented here.

2. Calculation of Mass of Working Fluid

The simple model requires the mass of working fluid as an input. The mass is calculated using the Schmidt analysis pressure equation [9], averaged over a complete rotation of the crankshaft.

3. Volume Variations

The volume variations of the compression and expansion spaces were based on the slider-crank mechanism loop closure equations derived by Cleghorn and Dechev [18]. Note that the compression space volume is influenced by both the displacer and piston positions. The volume of the displacer rod was neglected.

4. 'Simple Model Approach

The ideal adiabatic model forms a part of a greater model termed the “simple” model by Urieli and Berchowitz [9]. Additional losses have been added to extend the model.

A software flow diagram of the calculation procedure is shown in Fig. 2 below. Geometric data, working fluid properties, and operating conditions are input to begin the simulation. Volumes and surface areas are then determined from the geometric data. Mass of working fluid is calculated using the Schmidt analysis. Next, an ideal adiabatic simulation is performed assuming that the heater and cooler gas temperatures are equal to their corresponding wall temperatures. Results of this calculation are then used to determine the regenerator net enthalpy loss, and the new heater and cooler gas temperatures, making use of steady flow friction and heat transfer correlations. Iterative ideal adiabatic simulations are performed using updated heater and cooler gas temperatures, until the difference in heater and cooler temperatures between successive iterations is below a specified error tolerance. Once the heater and cooler temperatures have converged, heat and power losses are calculated and combined with the ideal adiabatic model results to give the final power and efficiency. Finally, the results are displayed via plots.

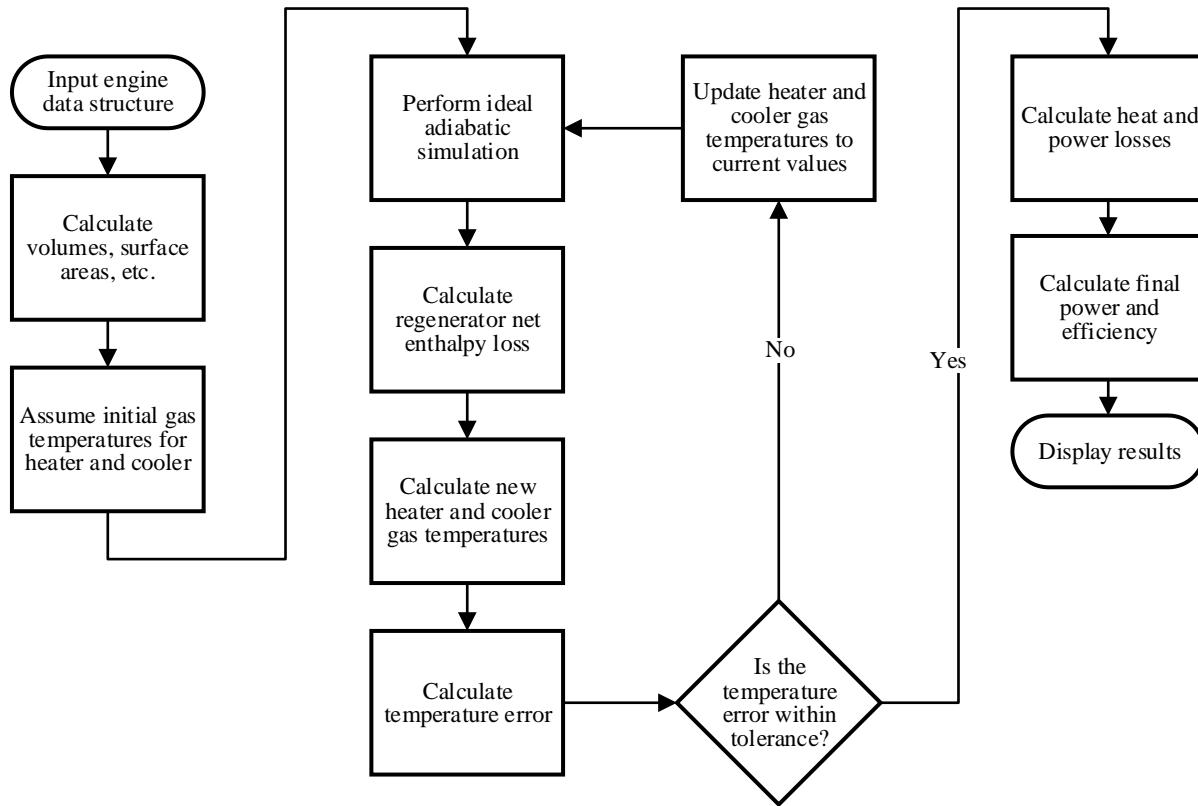


Figure 2. Software Flow Diagram for Mathematical Model

C. Heat Losses

Heat losses are assumed to affect the efficiency only. They are calculated individually and added to the ideal adiabatic model heat input to obtain the final heat input prediction.

1. Conduction loss

Conduction loss occurs when heat passes directly from the hot source to the cold sink without taking part in the engine cycle. For this study, the conduction path was divided into three components: The engine walls, the working fluid, and the displacer. For each component, a one-dimensional Fourier’s law approach was taken using the corresponding thermal conductivity, area, and length. The bulk thermal conductivity for each component was calculated as the area-weighted average of the component’s materials. The temperature profile for each conduction path was assumed to be linear. The one-dimensional Fourier’s law, with these assumptions, is given by:

$$\dot{Q} = kA\Delta T \quad (1)$$

Equation (1) highlights that the absolute value of the conduction loss will decrease linearly as the temperature difference decreases; however, if the ideal heat input decreases at a different rate, the relative contribution of conduction loss to the total heat input may change.

2. Appendix gap loss

Appendix gap loss refers to losses that occur inside the annular gap between the displacer and the cylinder. Appendix gap loss is estimated using equations from Urieli and Berchowitz [9].

3. Regenerator Enthalpy Loss

Due to imperfections in the regenerator, gas will leave the hot end below the heater temperature, and leave the cold end above the cooler temperature. This increases the load on both the heater and the cooler and leads to a decrease in efficiency. Here, the regenerator enthalpy loss is calculated as described by Urieli and Berchowitz [9]. Mass flow rate results from the ideal adiabatic model are substituted into a steady flow Stanton number correlation. The regenerator effectiveness is calculated, and used to find the regenerator enthalpy loss.

4. Heat Losses Not Considered

Heat losses not considered here include displacer seal leakage, and heating system loss. Displacer seal leakage would allow working fluid to pass directly from the hot space to the cold space, and vice-versa, without passing through the heat exchangers. This effect would tend to decrease the temperature difference between the compression and expansion space, reducing the power and efficiency. In this work, displacer leakage is assumed to be negligibly small for all hot source temperatures. Heating system loss refers to heat lost to the room before entering the engine. Since the heating system is well insulated for these experiments, the loss has been neglected.

D. Power Losses

1. Mechanical Friction and Forced Work

The ideas of Senft [7] are used to calculate the losses associated with mechanical friction. Following Senft, shaft work is determined from the amount of forced work that occurs during the cycle and the mechanism effectiveness. Forced work occurs when the direction of the pressure differential vector across the piston is in the opposite direction of the velocity vector of the piston. Mechanism effectiveness refers to the ratio of the actual torque that the piston would provide to the crankshaft over the ideal torque that the piston would provide in the absence of friction. Mechanism effectiveness is defined in Eq. (2) below. In general, the mechanism effectiveness can change throughout the cycle depending on the position of the mechanism and the varying loads; however, the variation is typically small and therefore the mechanism effectiveness can be assumed constant [7]. If the forced work, indicated work, and mechanism effectiveness are known, the shaft work can be calculated using Eq. (3) below [7]. For the calculations shown here, a mechanism effectiveness of 0.66 was used. This value was calculated using measured data with Eq. (3).

$$E = \frac{\tau_{actual}}{\tau_{ideal}} \quad (2)$$

$$W_s = E * W_i - \left(\frac{1}{E} - E\right) * W_f \quad (3)$$

2. Flow Friction

Flow friction was estimated for the heater, cooler, and regenerator only. To estimate flow friction losses, the flow rate through the heat exchangers is assumed to be constant for each crank angle increment used in the simulation. The Blasius equation for turbulent flow in smooth pipes was used for the heater and the cooler, and is given in Eq. (4).

$$f = 0.0791 Re^{0.75} \quad (4)$$

Note that f is the Reynolds friction factor. The Reynolds number was calculated separately for each crank angle increment, and was based on the hydraulic diameter of the heater and cooler slots. For the regenerator, the following correlation was used [11].

$$f = 54 + 1.43 Re^{0.78} \quad (5)$$

The Reynolds number for the regenerator used a hydraulic diameter based on the wire diameter and the porosity.

3. Gas spring hysteresis

The ST05G-CNC Stirling engine features a sealed crankcase, which is subject to gas spring hysteresis loss. Urieli and Berchowitz [9] suggest an equation for calculating the gas spring hysteresis loss, which is used here. Hysteresis occurs due to heat transfer between the gas and the walls of the crankcase, and due to viscous dissipation [9]. The effects of viscous dissipation are not considered here.

4. Power Losses Not Considered

Several power losses have not been calculated in the current mathematical model. In an ideal Stirling engine, there is no gas leakage between the power piston, or displacer piston, and the cylinder wall; however, in a real Stirling engine, seal leakage is an important loss that contributes to a reduction in the total power output of the engine. Seal leakage has not been added to the model at this stage. West [10] describes a loss called heat transfer hysteresis loss. Similar to gas spring hysteresis loss, this effect occurs due to adiabatic temperature swings in the working fluid as the cycle pressure rises and falls. It does not occur in adiabatic or isothermal spaces, so it is not represented in the current model. Other researchers have considered losses arising from the relative motion between the piston and the working fluid molecules [19]–[21]. These losses are accounted for using finite speed thermodynamics. They have not been considered here. Losses due to viscous friction in the crankcase, and due to the coolant pump have also been neglected.

E. Modeling Results

1. Effect of Temperature Difference on Losses

Figure 3 gives results of the power loss calculations as a function of hot side temperature. All calculations were done using a cold sink temperature of 5 °C, a running frequency of 5 Hz, and a mean pressure of 10 bar. Power losses are given as a percentage of the ideal adiabatic power output. For both piston sizes, the relative influences of mechanical friction, crankcase gas spring hysteresis, and flow friction all increase as the hot source temperature decreases. Decreasing the piston size reduces the absolute value of both mechanical friction and crankcase gas spring hysteresis. Mechanical friction is decreased due to a decreased amount of forced work. Gas spring hysteresis is decreased because the crankcase volume change is reduced.

In Fig. 3 (a), it is clear that mechanical friction is the dominant loss that will prevent the engine from running as the temperature difference is decreased. Fig. 3 (b) shows that decreasing the piston diameter from 85 mm to 44 mm reduces the influence of mechanical friction significantly.

To decrease the relative influence of flow friction, the engine could be operated at a lower speed. This may require an increase in the flywheel inertia to overcome parts of the cycle in which forced work occurs.

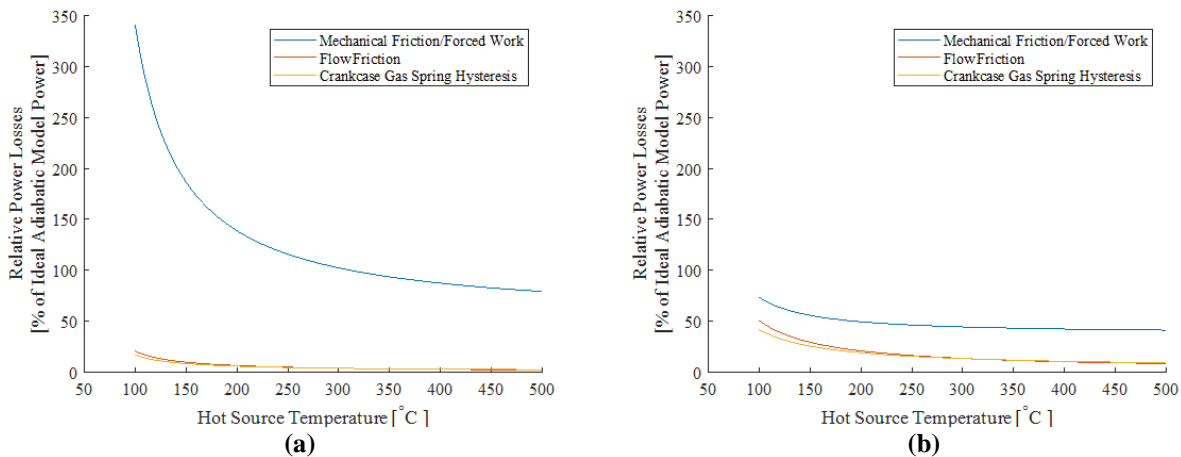


Figure 3. Relative Power Losses for (a) 85 mm Piston and (b) 44 mm Piston

Figure 4 presents the relative heat losses for the two piston sizes at the same operating point as Fig. 3. The heat losses are expressed as percentages of the ideal heat input from the adiabatic model. Of the three losses calculated, conduction loss was the most influential. For a given cold sink temperature, the absolute value of the conduction loss increases as the hot source temperature increases. Since the absolute value of conduction loss increases faster than the ideal heat input for a given change in source temperature, the relative influence of conduction loss increases with hot side temperature. This effect is indicated by the positive slope of the conduction loss line for both plots in Fig. 4. For a given hot source temperature, decreasing the piston size from 85 mm to 44 mm increases the relative influence of

conduction loss. This is because, for a given source temperature, the absolute value of conduction loss will be the same for both piston sizes and the ideal heat input will be smaller for the 44 mm piston.

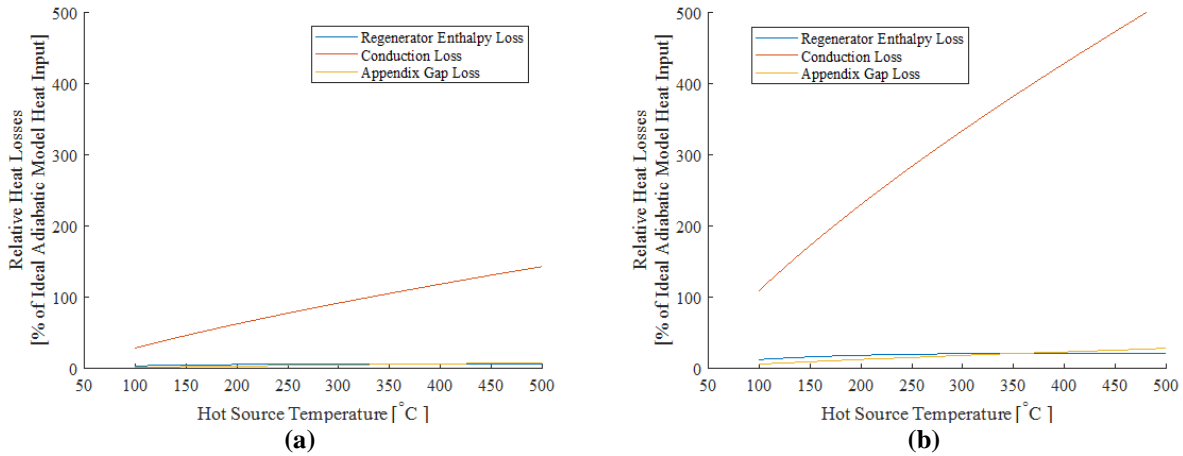


Figure 4. Relative Heat Losses for (a) 85 mm Piston and (b) 44 mm Piston

Figure 5 shows indicator diagrams for the two piston sizes at the same operating point. As expected, reducing the piston size from 85 mm to 45 mm decreases the indicated work of the cycle, which is represented by the area of the blue loop. The red shaded areas represent the forced work inherent in each cycle. It is clear from these plots that decreasing the piston size decreases the relative amount of forced work at the operating point shown. The negative effect of forced work depends on the mechanism effectiveness [7]. Taking the mechanism effectiveness to be 0.66, the shaft work for the two cycles below are -18.0 J for the 85 mm piston and 7.23 J for the 44 mm piston. This means that, for the 85 mm piston, the engine will not run at all under these conditions. The 44 mm piston configuration will run at this operating point. This example illustrates the importance of considering forced work effects when choosing a swept volume ratio.

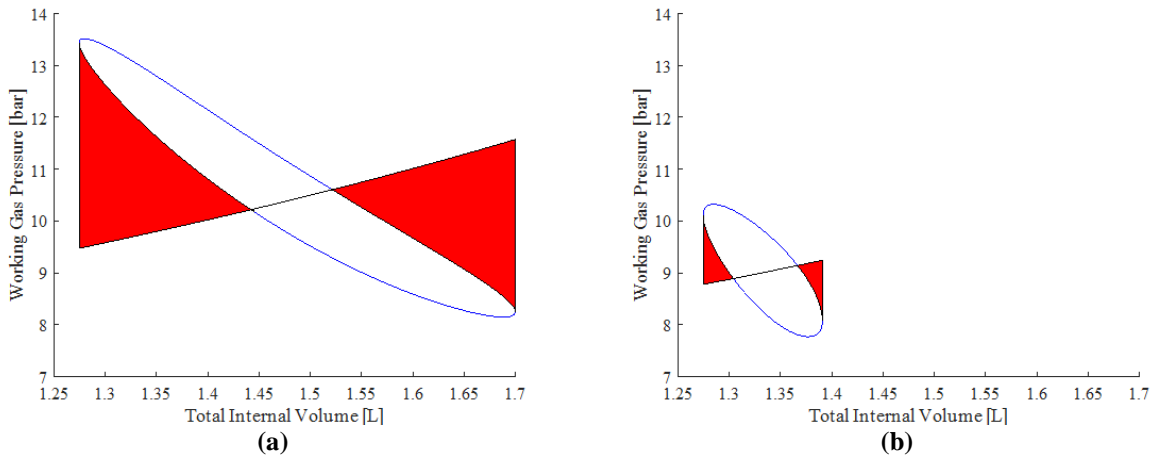


Figure 5. Forced Work Plots for (a) 85 mm Piston and (b) 44 mm Piston at 200 °C Source Temperature, 5 Hz Operating Frequency, and 10 bar Mean Pressure

2. Predicted Power and Efficiency

Figure 6 shows the predicted net power and efficiency for the two piston sizes as predicted by the mathematical model. The x-intercept of the power curve represents the theoretical minimum hot source temperature at which the engine will run. The plots show that by decreasing the piston diameter, the minimum source temperature has been decreased from 360°C to 175°C. Efficiency at low temperature differences is also improved with the smaller piston.

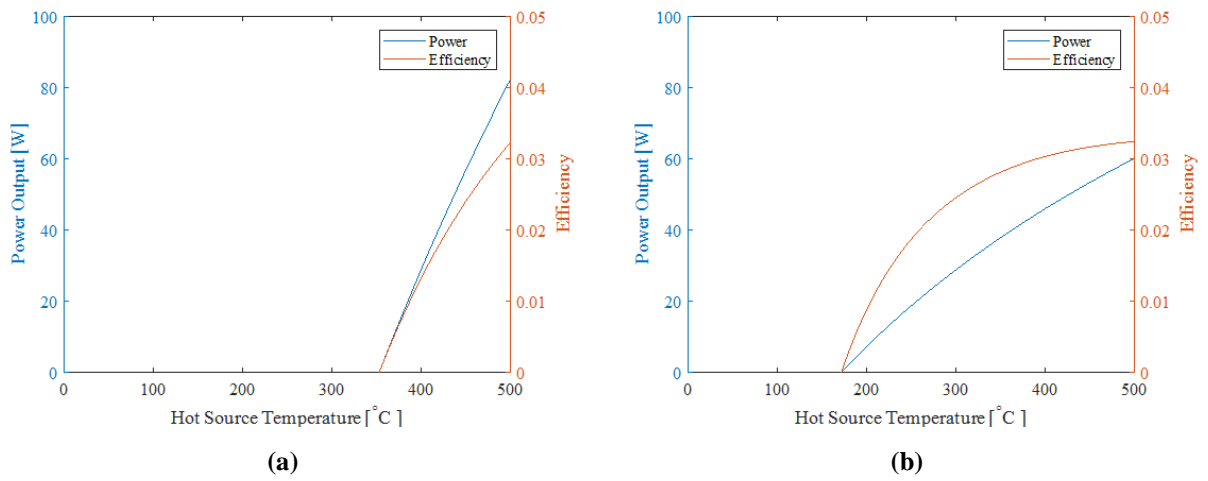


Figure 6. Predicted Power Output and Efficiency for (a) 85 mm Piston and (b) 44 mm Piston

III. Experimental Setup

An image of the experimental setup is shown in Fig. 7. The setup includes the engine, the heating system, the cooling system, temperature measurement system, the pressure measurement system, and the power output measurement system. All data is collected by the data acquisition computer using a custom written program (LabWindows/CVI™). The following subsections provide details on the test rig systems.

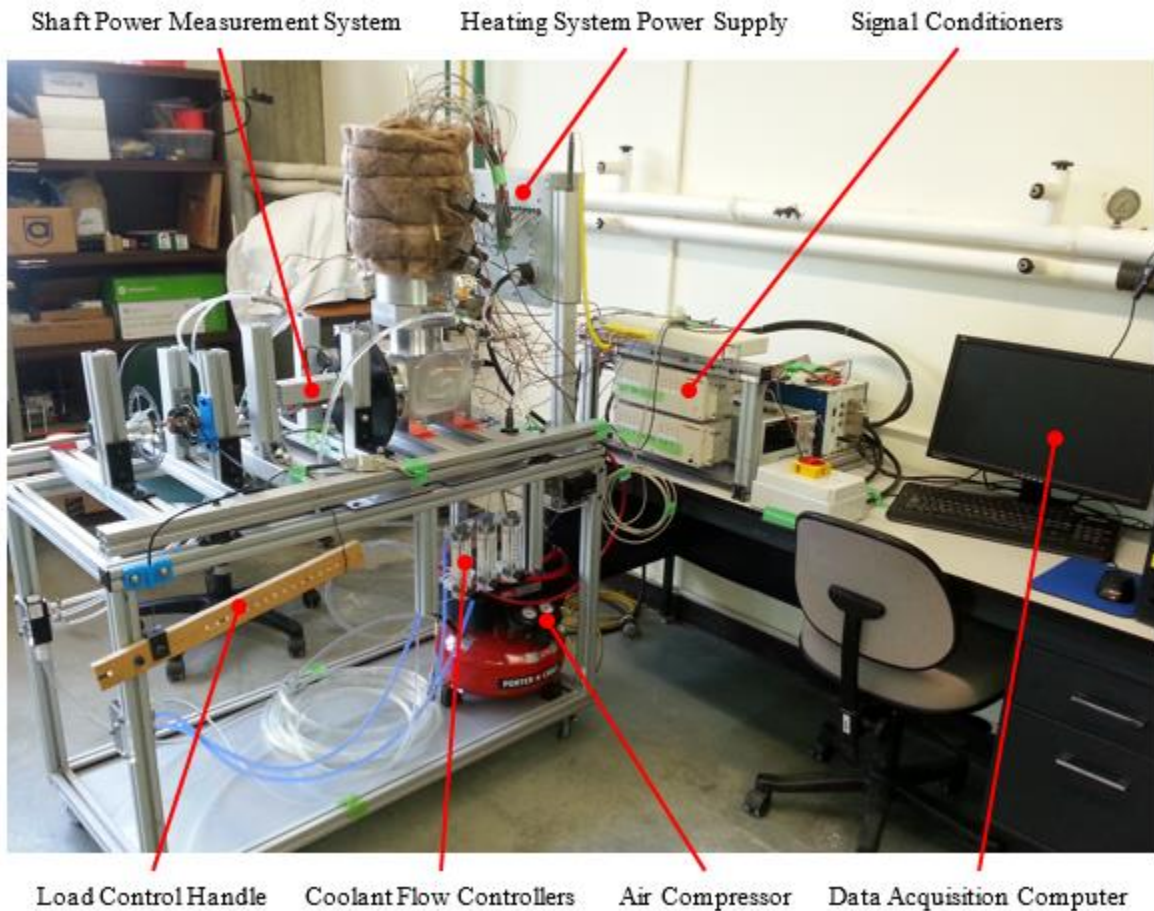


Figure 7. Image of Experimental Setup

A. Engine

The experimental engine is a modified version of the ST05G-CNC designed by Ve-Ingenieure. The stock ST05G-CNC is rated at 500 W of shaft power at a source temperature of 500 °C delivered at 500 RPM, using dry air or nitrogen working fluid [12]. A pressurized crankcase allows charge pressures of up to 10 bar. The engine is a gamma layout with slotted annular heat exchangers surrounding the displacer cylinder. A rendered solid model of the modified engine is presented in Fig. 8.

The main modification from the original design was the hot side heat exchanger, which was redesigned to mate with a solid heat reservoir. The heater is an annular gap configuration with slots added to increase the surface area. Compared to the heater of the original ST05G, the current heater has a larger internal surface area and a smaller internal volume.

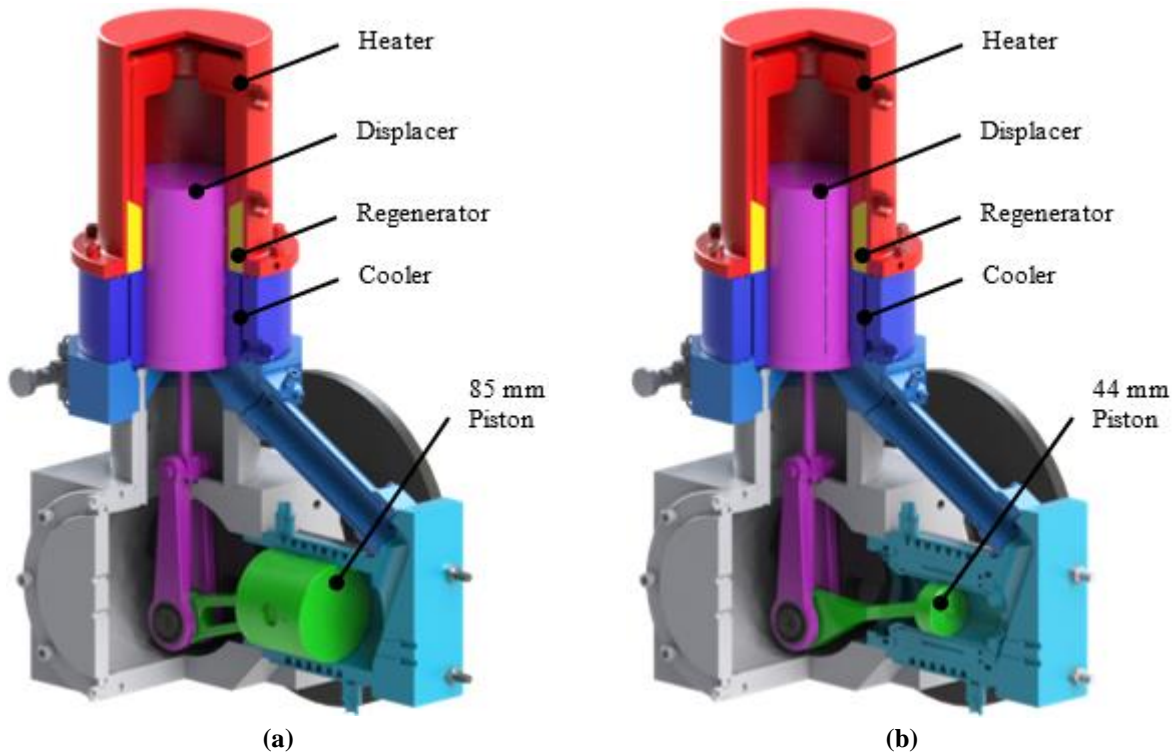


Figure 8. Solid Model of Experimental Engine (a) with 85mm Piston and (b) with 44mm Piston

B. Heating System

The heating system consists of 15 electric cartridge heaters housed in a steel cap. The cap fits over the heater of the engine, and is well insulated from the ambient air. The heaters have a combined heating capacity of 5,000 W, and can bring the cap to a maximum temperature of 650 °C. A temperature controller (CN8DPT-440-C24, Omega Engineering Inc.) maintains the temperature of the heater according to feedback from a single K-type grounded junction thermocouple (KMTSS-062G-6, Omega Engineering Inc.) placed in the center of the cap.

C. Cooling System

The water cooling system is separated into three cooling zones: the cooler, the connecting pipe, and the power cylinder. Each zone has an acrylic flow meter (75302113C08, King Instrument Company), and an inlet and outlet thermocouple (KMTSS-062G-6, Omega Engineering Inc.) installed. A refrigerated water bath (12101-41, Cole-Parmer Canada Company) maintains the coolant temperature, and circulates it through the engine.

D. Temperature Measurement

The experimental engine is equipped with seven K-type exposed junction thermocouples (HKMTSS-062E-6, Omega Engineering Inc.) to measure the gas temperature. Water temperatures are measured using six K-type thermocouples (KMTSS-062G-6, Omega Engineering Inc.) corresponding to the inlets and outlets of the three cooling zones. Thermocouple signals are collected using a thermocouple terminal block (TC 2095, National Instruments Inc.)

and processed using a low noise chassis (SCXI-1000, National Instruments Inc.) equipped with a thermocouple module (SCXI-1102B, National Instruments Inc.). Resolution of the cyclic temperature variation is limited due to the response time of the thermocouples.

E. Pressure Measurement

Pressure measurements are taken via five pressure transducers (DP15-50, Validyne Engineering). Signals from the transducers are conditioned using a demodulator (CD280-8, Validyne Engineering), and sampled at up to 250 000 Hz by a DAQ module (NI USB-6211, National Instruments Inc.). Resolution of the cyclic pressure variation throughout the engine cycle is possible up to the maximum rated engine speed of 12.5 Hz (750 RPM). Pressures are measured in both the power piston cylinder and the crankcase to allow experimental determination of the forced work and gas spring hysteresis effects.

F. Output Power Measurement

The power output measurement system is composed of a 500 pulse per revolution incremental rotary encoder (15S-19M1-0500NV1ROC-F03S1, Encoder Products Company), a non-contact rotary torque transducer (TRS600, FUTEK Advanced Sensor Technology, Inc.), and a loading system based on a bicycle disk brake. The power output measurement system is shown in Fig. 9. To calculate power, the engine speed measured by the rotary encoder is multiplied by the measured torque. To protect the torque transducer in the event of a sudden application of the disk brake, a torque-limiting coupling will sever the connection between the engine and the brake.

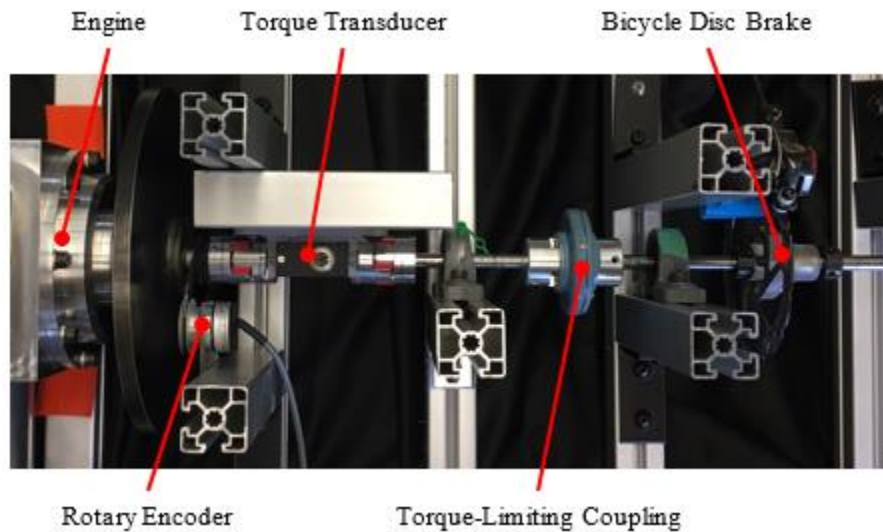


Figure 9. Image of Power Output Measurement System

IV. Results and Discussion

Experiments were conducted first with the 85 mm piston, followed by the 44 mm piston. A displacer piston failure limited the 44 mm piston tests to a hot source temperature of 100 °C. At 100 °C, the engine could only run for approximately 10 seconds before stalling. Data was collected during one of these short runs, and is presented below.

Data was collected for one second at a sampling rate 10 000 Hz. For the trials with the 85 mm piston, the engine was allowed to reach steady state before the measurement was taken. For the 44 mm piston trials, this was not possible. Several engine rotations occurred during the one second data set. Pressure values were averaged for each crank angle degree to produce the plots shown below.

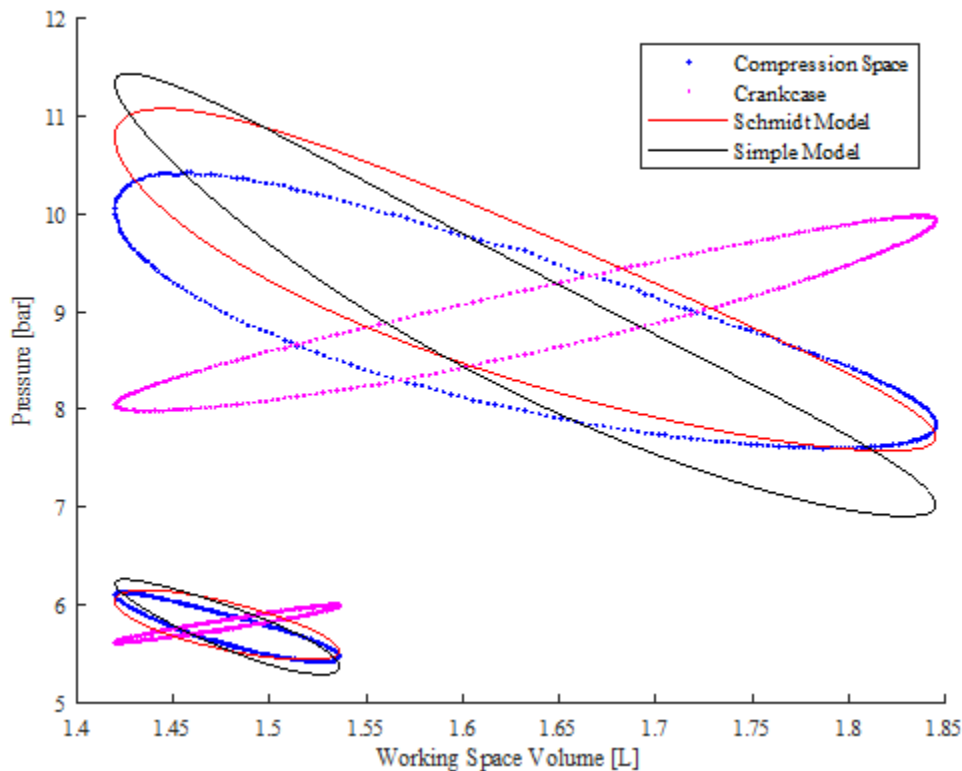


Figure 10. Experimental Indicator Diagram with Overlaid Models for Both Piston Sizes

Figure 10 is a plot of the Schmidt model, Simple model, and experimental indicator diagrams for both piston sizes. Data for the 85 mm piston is shown in the top right of the figure, while data for the 44 mm piston appears in the bottom left. Since the two data sets were not collected at the same operating point, only qualitative comparisons can be made between the two piston sizes at this stage. The 85 mm piston data was collected at a source temperature of 400°C, a fill pressure of 8.91 bar, and a frequency of 6.01 Hz (361 RPM). The 44 mm piston data was collected at a source temperature of 100°C, a fill pressure of 5.79 bar, and a frequency of 1.94 Hz (116 RPM).

From Fig. 10, it is clear that the 44 mm piston reduces the volume range of the cycle significantly, relative to the 85 mm piston. The pressure swing is also greatly reduced. This is due to the lower temperature difference, and fill pressure, at which the 44 mm piston data was collected.

The hysteresis effect of the crankcase pressure is also clearly visible in Fig. 10. The area of the crankcase pressure loop represents the work lost to gas spring hysteresis. The crankcase hysteresis loop also slightly increases the amount of forced work compared to a thin line. Both gas spring hysteresis and forced work could be reduced by increasing the crankcase volume.

Figure 11 is an enlarged plot of the 44 mm indicator diagram previously shown in Fig. 10. Both Fig. 10 and Fig. 11 display a significant discrepancy between the models and the experimental data. This is an expected result since neither of the models used to generate the indicator diagrams include all losses that affect the indicator diagram. All relevant losses would need to be included and coupled in the simulation to obtain precise agreement between the data and the model. Another potential source of discrepancy is the calculation of the mass of working fluid in the engine. As previously mentioned, the models use the Schmidt analysis equation averaged over a complete rotation to determine the mass. For the experiment, the true mass would depend on what position the crankshaft was in during the filling process.

The Schmidt model, which assumes isothermal swept volumes, shows a distinctly different shape than the simple model, which assumes adiabatic swept volumes. The adiabatic spaces result in a higher pressure swing relative to the isothermal case. In reality, all engine spaces have a finite heat transfer rate associated with them, so it is expected that the indicator diagram shape would fall somewhere in between the Schmidt and simple models.

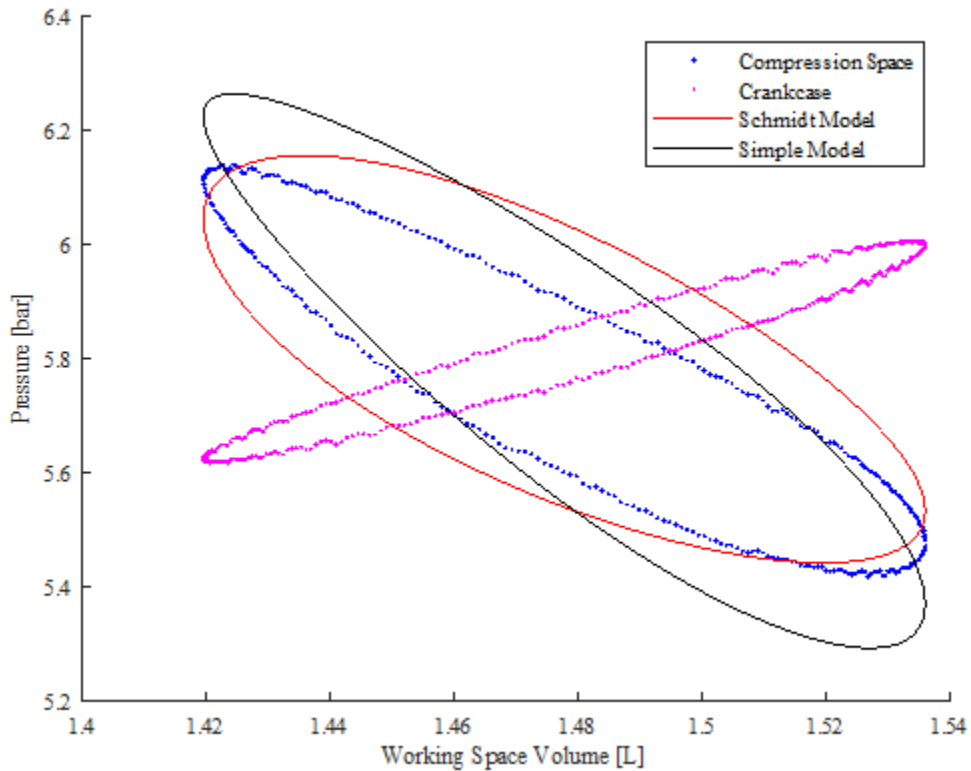


Figure 11. Experimental Indicator Diagram with Overlaid Models for 44 mm Piston

Table 1 lists the work from the 85 mm piston engine calculated by the Schmidt model, simple model and the experimental data with a source temperature of 400 °C, a fill pressure of 8 bar, and a running frequency of 1.94 Hz. The Schmidt model predicts that the indicated work is 0.9 % less than experimental indicated work and the Simple model predicts that the indicated work is 17.6 % less than experimental indicated work. Idealized thermodynamic models should predict indicated work that exceeds the measured indicated work of the engine; therefore, a discrepancy must be present. One potential discrepancies between the models and real engine could be the mass of working fluid, as mentioned above.

Table 1. Indicated and Experimental Work for 85 mm Piston Size with 400 °C Source Temperature, 8.91 bar Fill Pressure, and 6.01 Hz (361 RPM) Running Frequency

Schmidt Model Indicated Work (J)	54.5
Simple Model Indicated Work (J)	45.3
Current Mathematical Model Shaft Work (J)	-15.3
Experimental Indicated Work (J)	55.0
Experimental Shaft Work (J)	0.125

Table 1 also contains the current mathematical model shaft work prediction and experimental shaft work. The current mathematical model predicts that at these conditions the engine will not run (-15.3 J/cycle). However, experiments show that the engine can output 0.125 J/cycle and 0.2 % of the experimental indicated work. The engine output is low in this example, because the engine was free running with no applied load. The difference between the current mathematical model shaft work and the experimental shaft work suggest that the decoupled losses may have

an exaggerated affect on engine performance. Model validation measurements that isolate the individual losses are needed to improve agreement.

Table 2 shows the quantitative results corresponding to Fig. 11. In this case, both models overpredict the experimental indicated work. The difference in model error for the two piston sizes could be due to the difference in operating point between the data sets. Since the engine could only run briefly at the operating point tested with the 44 mm piston, the power output was not measured.

Table 2. Indicated and Experimental Work for 44 mm Piston Size with 100 °C Source Temperature, 5.79 bar Fill Pressure, and 1.94 Hz (116 RPM) Running Frequency

Schmidt Model Indicated Work (J)	4.54
Simple Model Indicated Work (J)	4.15
Current Mathematical Model Shaft Work (J)	-0.800
Experimental Indicated Work (J)	2.83
Experimental Shaft Work (J)	Not Measured

V. Conclusions

The preliminary investigation has demonstrated that optimum swept ratio between displacer and piston is strongly dependent on the temperature difference due to the effects of forced work and crankcase gas spring hysteresis. The relative influence of flow friction and conduction loss also increase as the temperature difference decreases.

Acknowledgments

This work was conducted with the support of the Natural Sciences and Engineering Research Council (NSERC) of Canada, the Canadian Foundation of Innovation (CFI), Alberta Innovates Energy and Environment Solutions, and Terrapin Geothermics.

References

- ¹Hargreaves, C. M., *The Philips Stirling Engine*, Elsevier Science Publishers B.V., Amsterdam, 1991.
- ²Martini, W. R., *Stirling Engine Design Manual*, NASA Lewis Research Center, Washington D.C., 1983.
- ³Cinar, C., and Karabulut, H., “Manufacturing and testing of a gamma type Stirling engine,” *Renew. Energy*, Vol. 30, No. 1, 2005, pp. 57–66.
- ⁴Valenti, G., Silva, P., Fergnani, N., Di Marcoberardino, G., Campanari, S., and Macchi, E., “Experimental and numerical study of a micro-cogeneration Stirling engine for residential applications,” *Energy Procedia*, Vol. 45, 2014, pp. 1235–1244.
- ⁵Schreiber, J., “Test Results and Description of a 1-kW Free-Piston Stirling Engine with a Dashpot Load,” NASA TM - 83407, 1983.
- ⁶Rogdakis, E. D., Antonakos, G. D., and Koronaki, I. P., “Thermodynamic analysis and experimental investigation of a Solo V161 Stirling cogeneration unit,” *Energy*, Vol. 45, No. 1, 2012, pp. 503–511.
- ⁷Senft, J. R., *Mechanical Efficiency of Heat Engines*, Cambridge University Press, New York, 2007.
- ⁸Kato, Y., “Indicated diagrams of a low temperature differential Stirling engine using flat plates as heat exchangers,” *Renew. Energy*, Vol. 85, 2016, pp. 973–980.
- ⁹Urieli, I., and Berchowitz, D. M., *Stirling Cycle Engine Analysis*, Adam Hilger Ltd, Bristol, 1984.
- ¹⁰West, C. D., *Principles and Applications of Stirling Engines*, Van Nostrand Reinhold Company Inc., New York, 1986.
- ¹¹Urieli, I., “Stirling Cycle Machine Analysis.” [Online]. URL: <https://www.ohio.edu/mechanical/stirling/index.html>. [Accessed: 14-Jun-2017].
- ¹²Viebach, D., “The ST05G Stirling Engine Project.” [Online]. URL: http://ve-ingenieure.de/projekt_st05g_cnc_engl.html. [Accessed: 11-Dec-2016].
- ¹³Hachem, H., Gheith, R., Aloui, F., and Ben Nasrallah, S., “Numerical characterization of a γ -Stirling engine considering losses and interaction between functioning parameters,” *Energy Convers. Manag.*, Vol. 96, 2015, pp. 532–543.
- ¹⁴Gheith, R., Aloui, F., and Ben Nasrallah, S., “Study of the regenerator constituting material influence on a gamma type Stirling engine,” *J. Mech. Sci. Technol.*, Vol. 26, No. 4, 2012, pp. 1251–1255.
- ¹⁵Gheith, R., Aloui, F., and Ben Nasrallah, S., “Determination of adequate regenerator for a Gamma-type Stirling engine,” *Appl. Energy*, Vol. 139, 2015, pp. 272–280.

- ¹⁶Bert, J., Chrenko, D., Sophy, T., Le Moyne, L., and Sirot, F., “Simulation, experimental validation and kinematic optimization of a Stirling engine using air and helium,” *Energy*, Vol. 78, 2014, pp. 701–712.
- ¹⁷Hooshang, M., Askari Moghadam, R., and AlizadehNia, S., “Dynamic response simulation and experiment for gamma-type Stirling engine,” *Renew. Energy*, Vol. 86, 2016, pp. 192–205.
- ¹⁸Cleghorn, W. L., and Dechev, N., *Mechanics of Machines*, 2nd ed., Oxford University Press, New York, 2015.
- ¹⁹Costea, M., Petrescu, S., and Harman, C., “Effect of irreversibilities on solar Stirling engine cycle performance,” *Energy Convers. Manag.*, Vol. 40, No. 15, 1999, pp. 1723–1731.
- ²⁰Petrescu, S., Costea, M., Harman, C., and Florea, T., “Application of the Direct Method to irreversible Stirling cycles with finite speed,” *Int. J. Energy Res.*, Vol. 26, No. 7, 2002, pp. 589–609.
- ²¹Hosseinzade, H., and Sayyaadi, H., “CAFS: The Combined Adiabatic-Finite Speed thermal model for simulation and optimization of Stirling engines,” *Energy Convers. Manag.*, Vol. 91, 2015, pp. 32–53.

PRELIMINARY MODEL VALIDATION FOR A GAMMA TYPE STIRLING ENGINE

Connor Speer, David Miller, David Nobes

*Department of Mechanical Engineering,
University of Alberta, Edmonton, AB.*

Introduction

The ST05G-CNC Stirling engine is a research engine designed by Ve-Ingenieure (Viebach, 2016). The engine, shown in Figure 1 (a) was originally intended to accept heat from a gaseous thermal source and features a bare tube hot side heat exchanger. In this study, experiments will be performed using a modified ST05G Stirling engine, shown in Figure 1 (b), with a heater head designed to connect to a solid thermal source.

Stirling engine thermodynamic models have been classified into first, second, and third order models based on their complexity (Martini, 1983). Second order models assume that loss mechanisms are independent of the ideal cycle and may be separately quantified and added to the ideal cycle result (Martini, 1983). This study will compare experimental results to the second order models described by Urieli and Berchowitz (Urieli and M., 1984). The forced work principles pioneered by Senft (2007) will also be examined.

Several experimental studies have been performed on the ST05G-CNC Stirling engine. Gheith et al. tested the influence of charge pressure, speed, coolant flow rate, and temperature difference on the engine performance (Ramla Gheith et al., 2011). The effect of changing regenerator properties has also been examined (Ramla Gheith, Aloui, and Nasrallah, 2012; Ramla Gheith, Aloui, and Ben Nasrallah, 2015). Other experiments have focused on the heater (R. Gheith et al., 2015). Experiments have been compared to a second order model. (Hachem et al., 2015). Bert et al. also used an ST05G Stirling engine for their research (Bert et al., 2014). They experimentally validated a second order model and numerically optimized the drivetrain kinematics. The effects of forced work were not considered in any of these studies.

Experimental Setup

The experimental setup is shown in Figure 2 below. The engine is heated using 15 electric cartridge heaters with a total power consumption of 5000 W. The cooling system consists of three independently controlled and instrumented water jackets. Exposed tip thermocouples measure the internal gas temperature at six locations. The gas pressure is measured at five locations. All measurements are collected using a custom written program (LabWindows™/CVI, National Instruments Inc.).

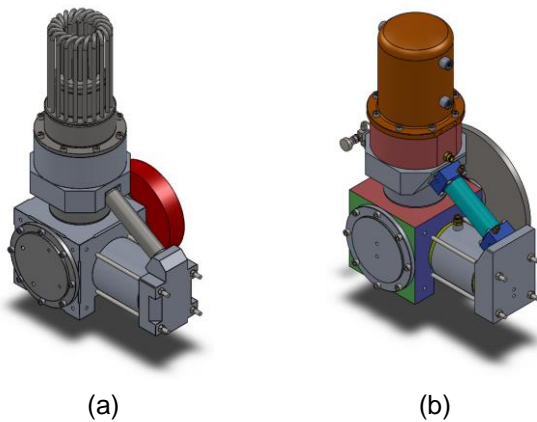


Figure 1: Solid Models of (a) The Original ST05G-CNC Stirling Engine (b) The Modified Engine

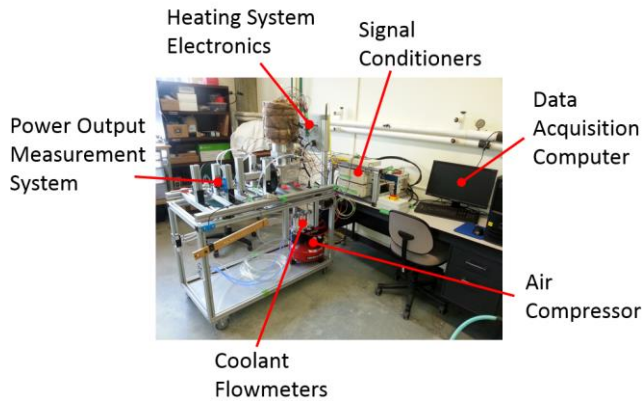


Figure 2: Image of Experimental Setup

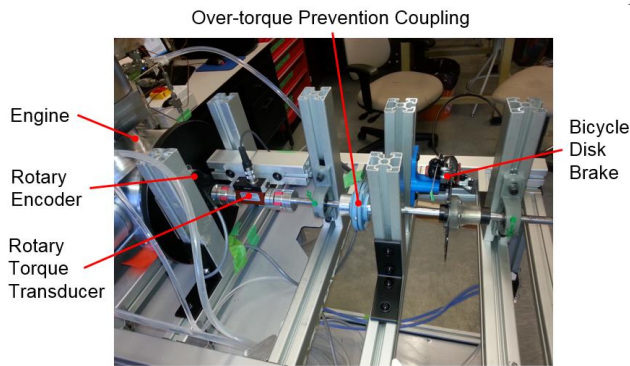


Figure 3: Image of Power Output Measurement System

Figure 3 shows the power output measurement system. Load torques are applied to the engine using a braking system based on bicycle disk brake. The torque and crank position are measured using an inline torque transducer and an incremental rotary encoder, respectively.

Results

Figure 4 is an experimentally measured indicator diagram for a charge pressure of 10 bar and a hot source temperature of 400°C. Regular ripples are visible in this diagram. These may indicate the presence of compressibility effects.

Figure 5 displays preliminary data overlaid with the Schmidt model that has been developed for this specific configuration of gamma Stirling engine. The model is based off the mean experimentally measured pressure and shows good agreement with the measure results.

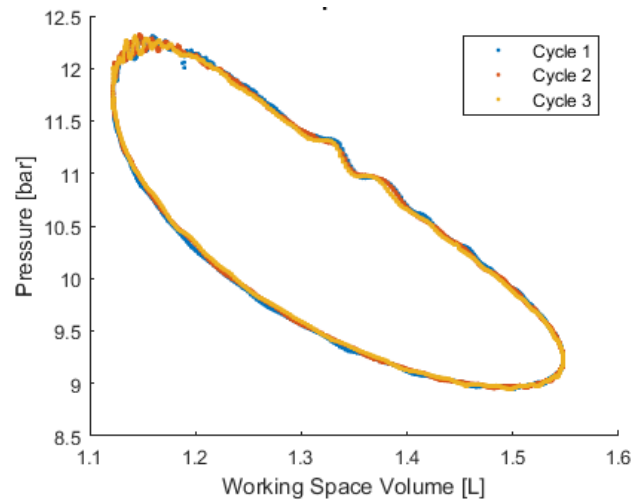


Figure 4: Experimental Indicator Diagram for Three Engine Cycles

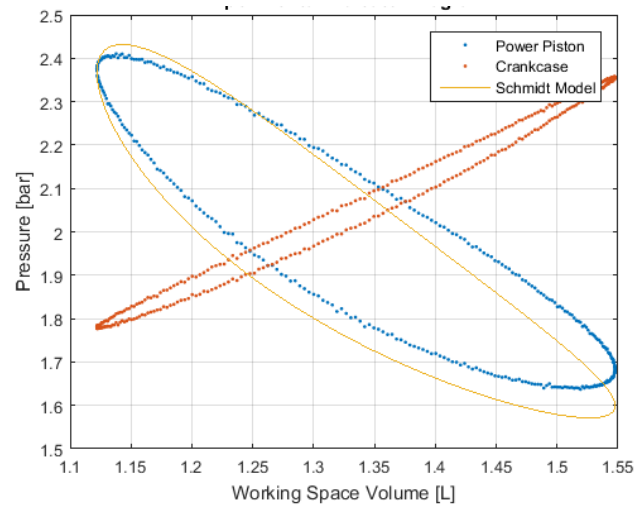


Figure 5: Comparison Between Experimental Data and Schmidt Model

Proposed Work

The full paper will include comparisons between the measured indicator diagram and that predicted by a second order thermodynamic model. Power output will be compared to that achieved by other research groups, and to the model predictions. From these comparisons, the effects of the design changes and the accuracy of the model will be deduced.

Acknowledgments

The authors gratefully acknowledge financial support from Natural Sciences and Engineering Research Council (NSERC) of Canada, Alberta Innovates Energy and Environment Solutions, and Terrapin Geothermics.

References

- Bert J., Chrenko D., Sophy T., Le Moyne L. and Sirot F. "Simulation, Experimental Validation and Kinematic Optimization of a Stirling Engine Using Air and Helium," *Energy*. **78**, 701–12, 2014.
- Gheith R., Aloui F. and Ben Nasrallah S. "Determination of Adequate Regenerator for a Gamma-Type Stirling Engine," *Applied Energy*. **139**. Elsevier Ltd, 272–80, 2015.
- Gheith R., Aloui F. and Nasrallah S. Ben "Study of the Regenerator Constituting Material Influence on a Gamma Type Stirling Engine," *Journal of Mechanical Science and Technology*. **26**, 1251–55, 2012.
- Gheith R., Aloui F., Tazerout M. and Nasrallah S. Ben "Experimental Investigations of a Gamma Stirling Engine," *International Journal of Energy Research*. **31**, 1175–82, 2011.
- Gheith R., Hachem H., Aloui F. and Ben Nasrallah S. "Experimental and Theoretical Investigation of Stirling Engine Heater: Parametrical Optimization," *Energy Conversion and Management*. **105**, 285–93, 2015.
- Hachem H., Gheith R., Aloui F. and Ben Nasrallah S. "Numerical Characterization of a γ -Stirling Engine Considering Losses and Interaction between Functioning Parameters," *Energy Conversion and Management*. **96**. Elsevier Ltd, 532–43, 2015.
- Martini W. R. "*Stirling Engine Design Manual*." Washington D.C.: NASA Lewis Research Center, 1983.
- Senft J. R. "*Mechanical Efficiency of Heat Engines*." New York: Cambridge University Press, 2007.
- Urieli I. and M. B. D. "*Stirling Cycle Engine Analysis*." Bristol: Adam Hilger Ltd, 1984.
- Viebach D. "The ST05G Stirling Engine Project"2016. Accessed December 11. http://ve-ingenieure.de/projekt_st05g_cnc_engl.html.